

# Beyond Universality: Probing Lepton Flavor in the SMEFT

---

Cornelius Grunwald<sup>a</sup> Gudrun Hiller<sup>b,a</sup> Kevin Kröninger<sup>a</sup> Lara Nollen<sup>a</sup>

<sup>a</sup>*TU Dortmund University, Department of Physics, Otto-Hahn-Str.4, D-44221 Dortmund, Germany*

<sup>b</sup>*Theoretical Physics Department, CERN, 1211 Geneva 23, Switzerland*

*E-mail:* [cornelius.grunwald@tu-dortmund.de](mailto:cornelius.grunwald@tu-dortmund.de), [gudrun.hiller@cern.ch](mailto:gudrun.hiller@cern.ch),  
[kevin.kroeninger@tu-dortmund.de](mailto:kevin.kroeninger@tu-dortmund.de), [lara.nollen@tu-dortmund.de](mailto:lara.nollen@tu-dortmund.de)

**ABSTRACT:** We present a global analysis of lepton-flavor-specific operators in the Standard Model Effective Field Theory (SMEFT), combining data from collider and flavor physics experiments. We systematically explore various lepton-flavor scenarios, including flavor-specific, universal, and democratic patterns, while employing a minimal flavor violation (MFV) ansatz in the quark sector. We constrain a set of 17 dimension-six SMEFT operators using a Bayesian fitting approach. Our analysis yields stringent bounds on the Wilson coefficients, probing new physics scales up to  $\mathcal{O}(1000)$  TeV. The strongest constraints are obtained in lepton-flavor universal and lepton-flavor democratic scenarios, in particular for the electroweak dipole operators. We further provide posterior-based predictions for  $B \rightarrow K^{(*)}\nu\bar{\nu}$  and  $B \rightarrow (\pi, \rho)\nu\bar{\nu}$  decays, highlighting their role as probes of the MFV hypothesis in upcoming Belle II measurements. Our results demonstrate the complementarity of collider and flavor observables, the impact of flavor assumptions on global SMEFT fits, and establish robust limits on extensions of the Standard Model in the lepton sector.

---

## Contents

<b>1</b>	<b>Introduction</b>	<b>2</b>
<b>2</b>	<b>Effective Field Theory Model</b>	<b>3</b>
2.1	SMEFT Setup	3
2.2	Flavor Patterns	4
2.3	Matching onto the LEFT	6
<b>3</b>	<b>Collider Observables</b>	<b>7</b>
3.1	Z-Boson Observables	8
3.2	W-Boson Decays	10
3.3	Dilepton Production at LEP	12
3.4	Drell–Yan Production	12
3.5	Top-Quark Pair-Production in Association with Leptons	13
<b>4</b>	<b>Flavor Observables</b>	<b>14</b>
4.1	Anomalous Magnetic Moments of Leptons	14
4.2	Lepton Decays	15
4.3	Meson Decays	17
<b>5</b>	<b>Global Analysis</b>	<b>22</b>
5.1	Fit Methodology	22
5.2	Higgs-Current Operators	22
5.3	Semileptonic Four-Fermion Operators	25
5.4	Four-Lepton Operators	27
5.5	Dipole Operators	29
5.6	Scalar and Tensor Operators	30
5.7	Testing MFV	32
5.8	CKM Parameters	33
<b>6</b>	<b>Predicting Dineutrino Modes</b>	<b>35</b>
<b>7</b>	<b>Conclusions</b>	<b>37</b>
<b>A</b>	<b>Numerical Input Parameters</b>	<b>39</b>
<b>B</b>	<b>Treatment of the CKM matrix</b>	<b>41</b>
<b>C</b>	<b>Matching Conditions</b>	<b>41</b>
<b>D</b>	<b>Credible intervals of the global fit</b>	<b>43</b>
<b>E</b>	<b>Further predictions for <math>B \rightarrow (K, K^*, \pi, \rho)\nu\bar{\nu}</math></b>	<b>46</b>

---

# 1 Introduction

The Standard Model Effective Field Theory (SMEFT) [1, 2] is a means to explore the physics beyond the electroweak scale in a systematic way. Combining experimental information from low and high energies, such as rare hadron decays and collider observables, this multi-observable approach fully exploits large data sets with complementary sensitivities to physics beyond the standard model (BSM); it can resolve otherwise flat directions in the parameter space of new physics (NP) couplings, eliminate large cancellations between them, and thus leads in general to significantly improved results relative to single sector fits. This advantage stems not just from more data hence better statistics, but also from the fact that different sectors are subject to different theory and experimental systematics, leading to more control in the global analysis. The increase in diagnostic power allows also to perform flavorful fits in which the fermions' generational structure is taken into account, or even probed, e.g., recently [3–8].

In this work we test the standard model (SM) in processes involving charged leptons and neutrinos. We employ the SMEFT and work beyond lepton flavor universality (LU), performing fits in a lepton-flavor specific manner. We go beyond existing works by considering  $\mathcal{O}(170)$  decays of mesons, leptons, electroweak bosons, as well as Drell-Yan (DY) and electroweak observables. In addition, we take into account the recent constraints from the muons anomalous magnetic moment [9, 10], and data from ATLAS on  $t\ell\ell$ , with results available for electrons and muons separately [11]. As processes which are used to extract the Cabibbo-Kobayashi-Maskawa (CKM)-matrix elements can be subjected to BSM physics we perform a joint fit to the CKM elements and SMEFT Wilson coefficients. To benefit from correlations between different quark generations we assume minimal flavor violation (MFV) in the quark sector, whose expansion we test simultaneously in the global fit.

The paper is organized as follows. The effective theory set up in SMEFT and the low energy effective theory (LEFT) is given in Sec. 2, together with the MFV ansatz and lepton flavor patterns considered: flavor-specific, LU, and lepton flavor democracy (LD). We present collider and flavor observables in Sec. 3 and Sec. 4 respectively. The fit methodology and a comparative discussion of SMEFT constraints for different operator types and lepton flavor patterns are given in Sec. 5. The posterior distributions allow further to predict branching ratios of rare  $B$ -decays into dineutrinos. Results are presented in Sec. 6. We conclude in Sec. 7. Numerical input is provided in App. A. In App. B we give details on the CKM prior fit to obtain priors for the full, global analysis. Matching conditions from SMEFT onto LEFT are given in App. C. In App. D we give the 90 % credible intervals of the global fit. Further predictions for  $B \rightarrow (K, K^*, \pi, \rho)\nu\bar{\nu}$  decays are provided in App. E.

## 2 Effective Field Theory Model

Effective field theories are a powerful tool to connect observables from various energy scales in a joint, largely model-independent framework. We employ the SMEFT [1] to probe NP in lepton-flavor specific fits. The set up used in this work is given in Sec. 2.1. We discuss flavor patterns in Sec. 2.2 and the matching onto the LEFT in Sec. 2.3.

### 2.1 SMEFT Setup

The SMEFT Lagrangian can be written as

$$\mathcal{L}_{\text{SMEFT}} = \mathcal{L}_{\text{SM}} + \sum_{d=5}^{\infty} \sum_i \frac{C_i^{(d)}}{\Lambda^{d-4}} O_i^{(d)}, \quad (2.1)$$

where  $\mathcal{L}_{\text{SM}}$  denotes the Lagrangian of the SM,  $O_i^{(d)}$  are dimension- $d$  operators, and  $C_i^{(d)}$  the corresponding Wilson coefficients. The scale  $\Lambda$  denotes the scale of NP, assumed to be sufficiently above the electroweak scale. The operators are composed out of SM degrees of freedom, and respect SM gauge and Poincare symmetries. To cover leading effects we restrict our analysis to  $d = 6$  operators for which we employ the Warsaw basis [2]. As we focus on leptonic NP, we exclude purely bosonic operators as well as operators involving only quark fields, such as quark-current and four-quark operators. In total, we consider 17 operators which are given in Tab. 1.

Dipole			
$O_{ij}^{eB}$	$(\bar{L}_i \sigma^{\mu\nu} E_j) \varphi B_{\mu\nu}$	$O_{ij}^{eW}$	$(\bar{L}_i \sigma^{\mu\nu} E_j) \tau^I \varphi W_{\mu\nu}^I$
Higgs-Current			
$O_{ij}^{\varphi l(1)}$	$(\varphi^\dagger i \overleftrightarrow{D}_\mu \varphi) (\bar{L}_i \gamma^\mu L_j)$	$O_{ij}^{\varphi l(3)}$	$(\varphi^\dagger i \overleftrightarrow{D}_\mu^I \varphi) (\bar{L}_i \tau^I \gamma^\mu L_j)$
$O_{ij}^{\varphi e}$	$(\varphi^\dagger i \overleftrightarrow{D}_\mu \varphi) (\bar{E}_i \gamma^\mu E_j)$		
Four-Lepton			
$O_{ijkl}^{ll}$	$(\bar{L}_i \gamma_\mu L_j) (\bar{L}_k \gamma^\mu L_m)$	$O_{ijkl}^{ee}$	$(\bar{E}_i \gamma_\mu E_j) (\bar{E}_k \gamma^\mu E_m)$
$O_{ijkl}^{le}$	$(\bar{L}_i \gamma_\mu L_j) (\bar{E}_k \gamma^\mu E_m)$		
Semileptonic Four-Fermion			
$O_{ijkl}^{lq(1)}$	$(\bar{L}_i \gamma_\mu L_j) (\bar{Q}_k \gamma^\mu Q_m)$	$O_{ijkl}^{lq(3)}$	$(\bar{l}_i \gamma_\mu \tau^I l_j) (\bar{Q}_k \gamma^\mu \tau^I Q_m)$
$O_{ijkl}^{qe}$	$(\bar{Q}_i \gamma_\mu Q_j) (\bar{E}_k \gamma^\mu E_m)$		
$O_{ijkl}^{eu}$	$(\bar{E}_i \gamma_\mu E_j) (\bar{U}_k \gamma^\mu U_m)$	$O_{ijkl}^{ed}$	$(\bar{E}_i \gamma_\mu E_j) (\bar{D}_k \gamma^\mu D_m)$
$O_{ijkl}^{lequ(1)}$	$(\bar{l}_i^p E_j) \epsilon_{pr} (\bar{q}_k^r U_m)$		
$O_{ijkl}^{lu}$	$(\bar{L}_i \gamma_\mu L_j) (\bar{U}_k \gamma^\mu U_m)$	$O_{ijkl}^{ld}$	$(\bar{L}_i \gamma_\mu L_j) (\bar{D}_k \gamma^\mu D_m)$
$O_{ijkl}^{lequ(3)}$	$(\bar{l}_i^p \sigma_{\mu\nu} E_j) \epsilon_{pr} (\bar{q}_k^r \sigma^{\mu\nu} U_m)$		

**Table 1.** Dimension-six SMEFT Wilson coefficients considered in this work.

We denote the left-handed lepton doublets by  $L$  and the right-handed charged lepton singlets by  $E$ . The Higgs doublet is written as  $\varphi$ . Quark doublets are denoted by  $Q$ , while the right-handed up-type and down-type quarks are represented by  $U$  and  $D$ , respectively. Generation indices are labeled by  $i, j, k, m = 1, 2, 3$ , and isospin indices by  $p, r = 1, 2$ . The Pauli matrices are denoted by  $\tau^I$ , and the antisymmetric tensor by  $\epsilon_{pr}$ , with  $\epsilon_{12} = +1$ . The gauge field strength tensors of the  $U(1)$  and  $SU(2)$  gauge groups are denoted by  $B_{\mu\nu}$  and  $W_{\mu\nu}^I$ , respectively. The covariant derivative is written as  $D_\mu$ .

Given that our analysis involves collider processes at high energies, we set  $\Lambda = 10 \text{ TeV}$  to ensure the validity of the EFT expansion. We further assume all Wilson coefficients to be real, thereby excluding additional sources of CP violation within the SMEFT framework. To evolve the Wilson coefficients from the scale  $\Lambda = 10, \text{ TeV}$  to the energy scale relevant for our observables, we use the one-loop SMEFT renormalization group equations (RGEs) [12–14], which we solve numerically with the Python package `Wilson` [15]. In the following we use rescaled Wilson coefficients

$$\tilde{C} = \frac{v^2}{\Lambda^2} C, \quad (2.2)$$

where  $v \simeq 246 \text{ GeV}$  denotes the Higgs vacuum expectation value. This absorbs the explicit  $\Lambda$ -dependence (2.1) into the definition of the Wilson coefficients  $\tilde{C}$ , making them comparable across different choices of  $\Lambda$ , up to residual effects from renormalization group running. We expand observables in inverse powers of the NP scale and keep terms including those of the order  $\Lambda^{-4}$ .

For the electroweak input parameters, we adopt the  $\alpha_{\text{em}}, m_W, m_Z$  input scheme. With this choice and given the set of operators listed in Tab.1, the input parameters remain unaffected by SMEFT-induced shifts. For details see Appendix A. Since the extraction of CKM matrix elements can be influenced by BSM physics, we treat the CKM parameters as nuisance parameters in the fit following Refs. [16]. Further details are provided in Appendix B.

## 2.2 Flavor Patterns

In its most general form, the SMEFT contains 2499 free parameters at dimension-six after accounting for all generation indices [2]. This number is far too large to be fully constrained by current experimental data, making additional assumptions about the flavor structure necessary. In this analysis, we adopt the MFV framework in the quark-flavor sector to reduce the number of free parameters. In MFV, the Yukawa couplings  $Y_{u,d}$  of the up-type and down-type quarks are the sole sources of flavor violation, treated as spurions that break the  $U(3)^3$  quark flavor symmetry of the SM gauge sector [17]. We include terms up to  $\mathcal{O}(Y_i^2)$  in the MFV expansion and approximate  $Y_d \sim 0$  and  $Y_u \sim \text{diag}(0, 0, y_t)$ , that is, from all the quark Yukawas we only keep the one of the top.<sup>1</sup>

---

<sup>1</sup>BSM effects can break the relation between fermion masses and their Yukawa couplings. While only upper limits exist on the latter for the first generation and the strange quark at the level of  $\mathcal{O}(10^2)$  above their SM values, the others are more or less well constrained, and model-independently  $y_{f \neq t} \ll 1$ , except for the top, for which holds  $y_t \simeq 1$ .

The quark bilinears can then be written as

$$\begin{aligned}
\bar{Q}Q : \quad C_{ij} &= a_1 \delta_{ij} + a_2 y_t^2 \delta_{i3} \delta_{j3}, & \bar{U}U : \quad C_{ij} &= b_1 \delta_{ij} + b_2 y_t^2 \delta_{i3} \delta_{j3}, \\
\bar{Q}U : \quad C_{ij} &= (c_1 + c_2 y_t^2) y_t \delta_{i3} \delta_{j3}, & \bar{D}D : \quad C_{ij} &= e_1 \delta_{ij}, \\
\bar{Q}D : \quad C_{ij} &= 0, & \bar{U}D : \quad C_{ij} &= 0.
\end{aligned} \tag{2.3}$$

Since we neglect the small down-type Yukawas chirality-flipping operators with a right-handed down-type quark i.e.  $\bar{Q}D$  and right-handed charged currents  $\bar{U}D$  vanish. The up-type scalar and tensor operators  $O_{lequ}^{(1)}$  and  $O_{lequ}^{(3)}$  involving  $\bar{Q}U$ , on the other hand, couple only to third-generation quarks in this framework, leading to the absence of chirality-flipping interactions involving first- or second-generation quarks.

To confront the SMEFT with experimental data, the operators defined in the gauge basis must be rotated to the mass basis. In the MFV framework, this rotation yields identical results regardless of whether it is performed in the up- or down-type quark sector [6]. In the mass basis, the parameterization of the quark bilinears reads

$$\begin{aligned}
\bar{q}_L q_L : \quad C_{ij}^{\prime, \bar{u}u} &= a_1 \delta_{ij} + a_2 y_t^2 \delta_{i3} \delta_{j3}, & C_{ij}^{\prime, \bar{d}d} &= a_1 \delta_{ij} + a_2 y_t^2 V_{ti}^* V_{tj}, \\
& C_{ij}^{\prime, \bar{u}d} &= a_1 V_{ij} + a_2 y_t^2 \delta_{i3} V_{tj}, & C_{ij}^{\prime, \bar{d}u} &= a_1 V_{ji}^* + a_2 y_t^2 V_{ti}^* \delta_{j3}, \\
\bar{q}_L u_R : \quad C_{ij}^{\prime, \bar{u}u} &= (c_1 + c_2 y_t^2) y_t \delta_{i3} \delta_{j3}, & C_{ij}^{\prime, \bar{d}u} &= (c_1 + c_2 y_t^2) y_t V_{ti}^* \delta_{j3}, \\
\bar{u}_R u_R : \quad C_{ij}^{\prime, \bar{u}u} &= b_1 \delta_{ij} + b_2 y_t^2 \delta_{i3} \delta_{j3}, \\
\bar{d}_R d_R : \quad C_{ij}^{\prime, \bar{d}d} &= b_1 \delta_{ij},
\end{aligned} \tag{2.4}$$

where  $V_{ij}$  are the CKM matrix elements. In this approach, down-type flavor-changing neutral currents (FCNCs) arise at second order in the MFV expansion for operators involving two left-handed quark doublets, and are proportional to the CKM factor  $V_{ti}^* V_{tj}$ . In contrast, up-type FCNCs are absent due to  $Y_d \sim 0$ . For further details on the MFV expansion in the SMEFT context, see e.g. Refs. [6, 18].

To test MFV in the fit we follow Ref. [6] and define the following degrees of freedom

$$\begin{aligned}
\tilde{C}_{\bar{q}q} &= \frac{v^2}{\Lambda^2} a_1, & \tilde{C}_{\bar{u}u} &= \frac{v^2}{\Lambda^2} b_1, & \tilde{C}_{\bar{q}u} &= \frac{v^2}{\Lambda^2} (c_1 + y_t^2 c_2), \\
\tilde{C}_{\bar{d}d} &= \frac{v^2}{\Lambda^2} d_1, & r_L &= y_t^2 \frac{a_2}{a_1}, & r_R &= y_t^2 \frac{b_2}{b_1}.
\end{aligned} \tag{2.5}$$

The ratios  $r_L$  and  $r_R$ <sup>2</sup> quantify the relative size of higher-order terms in the MFV expansion compared to the leading-order contributions. In our fit, each operator with a  $\bar{Q}Q$  or  $\bar{U}U$  structure is assigned its own MFV parameter  $r_{L/R}^i$ , allowing for differences in flavor structure that may arise in more intricate UV completions.

We perform lepton-flavor-specific and lepton-flavor-universal analyses to explore the impact of lepton flavor on the bounds. In the lepton-flavor-specific fits, we assume that NP couples exclusively to a single lepton flavor. We further consider a lepton-flavor-universal (LU)

<sup>2</sup>These ratios are denoted by  $\gamma_a$  and  $\gamma_b$  in Ref. [6].

scenario and a lepton-flavor-democratic (LD) scenario. In the LU case, we assume that NP couples equally to each lepton flavor in a flavor-diagonal manner, such that  $\tilde{C}_{ij} = \tilde{C}_{\text{LU}} \delta_{ij}$  for all lepton bilinears. In contrast, the LD scenario assumes that NP couples equally to all lepton flavors, including off-diagonal terms. This implies  $\tilde{C}_{ij} = \tilde{C}_{\text{LD}}$  for all  $i, j$ , thereby allowing lepton-flavor-conserving (LFC) and lepton-flavor-violating (LFV) interactions.

### 2.3 Matching onto the LEFT

While collider observables are naturally described within the SMEFT, flavor observables are typically evaluated at lower energy scales. To account for this, we compute these observables in the LEFT, which is valid at scales below the electroweak one. The LEFT is obtained by integrating out the top quark, the  $W$  and  $Z$  bosons, and the Higgs boson. As a result, the gauge symmetry is reduced to  $SU(3)_c \times U(1)_{\text{em}}$ , in contrast to the full SM symmetry  $SU(3)_c \times SU(2)_L \times U(1)_Y$  that characterizes the SMEFT.

We perform the matching of SMEFT Wilson coefficients onto the LEFT at the scale  $\mu = m_W$  at tree level, following Ref. [19]. Details of the matching conditions are provided in Appendix C. The resulting LEFT Wilson coefficients are then evolved to the low-energy scales using the one-loop RGEs of the LEFT [20], implemented in the `Wilson` package [15].

Tab. 2 lists the LEFT Wilson coefficients induced by the SMEFT operators considered in this work. Within our MFV framework, no scalar or tensor operators are generated in the LEFT, as the top quark, which is the only flavor contributing to these operators, is integrated out. To distinguish between the two EFTs, we use  $\mathcal{C}$  and  $\mathcal{Q}$  to denote LEFT Wilson coefficients and operators, respectively, and  $\tilde{C}$  and  $O$  for their SMEFT counterparts. For processes below the electroweak scale, we denote charged leptons by  $\ell$ , neutrinos by  $\nu$ , and up- and down-type quarks by  $u$  and  $d$ , respectively. Fermion chirality is indicated by  $L$  and  $R$ , and the electromagnetic field strength tensor is denoted by  $F_{\mu\nu}$ .

While there is an intrinsic  $SU(2)_L$  link between the left-handed fermions in the SMEFT, this symmetry is no longer present in the LEFT due to the breaking of the  $SU(2)_L$  gauge symmetry. Following from the matching, however, the SMEFT dictates correlations among the LEFT Wilson coefficients comprising left-handed fermions, which can be tested experimentally. For instance, the operator  $O_{lq}^1$ , which couples left-handed leptons to left-handed quarks, matches onto four different LEFT operators,  $\mathcal{Q}_{\nu u}^{V,LL}$ ,  $\mathcal{Q}_{\nu d}^{V,LL}$ ,  $\mathcal{Q}_{e u}^{V,LL}$  and  $\mathcal{Q}_{e d}^{V,LL}$ . Without the  $SU(2)_L$  structure, these operators can be treated independently, while they are correlated within the SMEFT. This allows to test flavor patterns and also the SMEFT ansatz with the hypothesis of heavy NP itself.

In addition to the direct contributions from SMEFT four-fermion operators, four-fermion operators in the LEFT also receive contributions from Higgs-current operators. Double insertions of these SMEFT Higgs-current operators can lead to contributions of order  $\Lambda^{-4}$ , as illustrated in Fig. 1. To maintain a consistent expansion in the SMEFT scale  $\Lambda$ , we

Dipole			
$\mathcal{Q}_{e\gamma}_{ij}$	$(\bar{\ell}_L \sigma^{\mu\nu} \ell_R) F_{\mu\nu}$		
LL			
$\mathcal{Q}_{ee}^{V,LL}_{ijkm}$	$(\bar{\ell}_L \gamma_\mu \ell_L) (\bar{\ell}_L \gamma^\mu \ell_L)$	$\mathcal{Q}_{\nu e}^{V,LL}_{ijkm}$	$(\bar{\nu}_L \gamma_\mu \nu_L) (\bar{\ell}_L \gamma^\mu \ell_L)$
$\mathcal{Q}_{\nu d}^{V,LL}_{ijkm}$	$(\bar{\nu}_L \gamma_\mu \nu_L) (\bar{d}_L \gamma^\mu d_L)$	$\mathcal{Q}_{eu}^{V,LL}_{ijkm}$	$(\bar{\ell}_L \gamma_\mu \ell_L) (\bar{u}_L \gamma^\mu u_L)$
$\mathcal{Q}_{vedu}^{V,LL}_{ijkm}$	$(\bar{\nu}_L \gamma_\mu \ell_L) (\bar{d}_L \gamma^\mu u_L) + \text{h.c.}$		
		$\mathcal{Q}_{\nu u}^{V,LL}_{ijkm}$	$(\bar{\nu}_L \gamma_\mu \nu_L) (\bar{u}_L \gamma^\mu u_L)$
		$\mathcal{Q}_{ed}^{V,LL}_{ijkm}$	$(\bar{\ell}_L \gamma_\mu \ell_L) (\bar{d}_L \gamma^\mu d_L)$
RR			
$\mathcal{Q}_{ee}^{V,RR}_{ijkm}$	$(\bar{\ell}_R \gamma_\mu \ell_R) (\bar{\ell}_R \gamma^\mu \ell_R)$	$\mathcal{Q}_{eu}^{V,RR}_{ijkm}$	$(\bar{\ell}_R \gamma_\mu \ell_R) (\bar{u}_R \gamma^\mu u_R)$
		$\mathcal{Q}_{ed}^{V,RR}_{ijkm}$	$(\bar{\ell}_R \gamma_\mu \ell_R) (\bar{d}_R \gamma^\mu d_R)$
LR			
$\mathcal{Q}_{ee}^{V,LR}_{ijkm}$	$(\bar{\ell}_L \gamma_\mu \ell_L) (\bar{\ell}_R \gamma^\mu \ell_R)$	$\mathcal{Q}_{\nu e}^{V,LR}_{ijkm}$	$(\bar{\nu}_L \gamma_\mu \nu_L) (\bar{\ell}_R \gamma^\mu \ell_R)$
$\mathcal{Q}_{\nu d}^{V,LR}_{ijkm}$	$(\bar{\nu}_L \gamma_\mu \nu_L) (\bar{d}_R \gamma^\mu d_R)$	$\mathcal{Q}_{eu}^{V,LR}_{ijkm}$	$(\bar{\ell}_L \gamma_\mu \ell_L) (\bar{u}_R \gamma^\mu u_R)$
$\mathcal{Q}_{ue}^{V,LR}_{ijkm}$	$(\bar{u}_L \gamma_\mu u_L) (\bar{\ell}_R \gamma^\mu \ell_R)$	$\mathcal{Q}_{de}^{V,LR}_{ijkm}$	$(\bar{d}_L \gamma_\mu d_L) (\bar{\ell}_R \gamma^\mu \ell_R)$
		$\mathcal{Q}_{\nu u}^{V,LR}_{ijkm}$	$(\bar{\nu}_L \gamma_\mu \nu_L) (\bar{u}_R \gamma^\mu u_R)$
		$\mathcal{Q}_{ed}^{V,LR}_{ijkm}$	$(\bar{\ell}_L \gamma_\mu \ell_L) (\bar{d}_R \gamma^\mu d_R)$

**Table 2.** LEFT operators considered in this work.

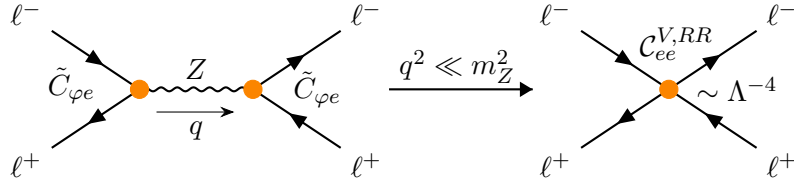


**Figure 1.** Feynman diagrams illustrating double insertions of the SMEFT Higgs-current operators (left diagram) in the matching to the LEFT four-lepton operator (right diagram).

include these double-insertion contributions only in the interference terms between the SM and the NP amplitudes.

### 3 Collider Observables

In this section, we discuss collider observables within the SMEFT,  $Z$ -decays (Sec. 3.1) and  $W$ -decays (Sec. 3.2), dilepton production at lepton colliders (Sec. 3.3), neutral- and charged-current Drell–Yan processes (Sec. 3.4), and top-quark pair production in association with leptons (Sec. 3.5).

### 3.1 Z-Boson Observables

The tree-level partial width for the decay  $Z \rightarrow l_i l_j$  can be expressed as [21]

$$\Gamma(Z \rightarrow l_i l_j) = \frac{G_F m_Z^3}{6\pi\sqrt{2}} \left( |g_{ij}^L|^2 + |g_{ij}^R|^2 \right), \quad (3.1)$$

where  $g_{ij}^L$  and  $g_{ij}^R$  denote the left- and right-handed couplings of the charged leptons and neutrinos to the  $Z$  boson, respectively. In the SMEFT, the  $Z$  boson couplings to fermions are modified by the Higgs-current operators, which can also induce flavor-violating decays. For the Wilson coefficients considered in this work, the couplings read

$$g_{ij}^{\nu} = \frac{1}{2}\delta_{ij} - \frac{1}{2}\tilde{C}_{\varphi l}^-, \quad g_{ij}^{\nu} = 0, \quad (3.2)$$

$$g_{ij}^{\ell} = \frac{1}{2}\delta_{ij}(2\sin^2\theta_W - 1) - \frac{1}{2}\tilde{C}_{\varphi l}^+, \quad g_{ij}^{\ell} = \delta_{ij}\sin^2\theta_W - \frac{1}{2}\tilde{C}_{\varphi e}, \quad (3.3)$$

with

$$\tilde{C}_{\varphi l}^{\pm} = \tilde{C}_{\varphi l}^{(1)} \pm \tilde{C}_{\varphi l}^{(3)}, \quad (3.4)$$

where the Wilson coefficients are evaluated at the scale of the  $Z$ -mass,  $\mu \sim m_Z$ .  $\theta_W$  and  $G_F$  denote the weak mixing angle and Fermi's constant, respectively.

In addition, dipole operators contribute to the  $Z$  boson decay width into charged leptons. Their contribution to the partial width is given by

$$\Gamma_{\text{Dipole}}(Z \rightarrow l_i l_j) = \frac{G_F m_Z^3}{24\pi\sqrt{2}} \left( \tilde{C}_{eZ}^2 + \tilde{C}_{ji}^2 \right), \quad (3.5)$$

where

$$\tilde{C}_{eZ} = \sin\theta_W \tilde{C}_{eB} + \cos\theta_W \tilde{C}_{eW}. \quad (3.6)$$

The measurements of the  $Z$  boson decay widths and the limits on the LFV branching fractions are listed in Tab. 3 alongside the corresponding SM predictions. For the partial widths to charged leptons, we include the correlation of the data provided by LEP [22].

While the decay widths to charged leptons constrain  $\tilde{C}_{\varphi l}^+$ , the decay width to neutrinos is sensitive to  $\tilde{C}_{\varphi l}^-$ . A combined analysis of both decay modes therefore enables to disentangle  $\tilde{C}_{\varphi l}^{(1)}$  and  $\tilde{C}_{\varphi l}^{(3)}$ , which would otherwise remain degenerate in the fit. Fig. 2 illustrates this synergy for the example of a lepton flavor specific pattern where only the  $e\mu$  coefficient is switched on. The plot shows the 90% credible regions from a two-dimensional fit in the  $\tilde{C}_{\varphi l}^{(1)} - \tilde{C}_{\varphi l}^{(3)}$  plane. The region in blue is obtained from a fit of  $Z \rightarrow \nu\bar{\nu}$  decays, while the orange region is derived from  $Z \rightarrow e\mu$  decays. The combination of both channels (red region) breaks the degeneracy and significantly reduces the allowed parameter space.

We further consider forward-backward asymmetries  $A_{\text{FB}}^{\ell}$  at the  $Z$ -pole, defined as the difference of cross sections in the  $Z$  boson center-of-mass frame regarding the scattering

Observable	Measurement	SM prediction
$\Gamma(Z \rightarrow e^+e^-)$	83.92(12) MeV [22]	83.987(68) MeV [22]
$\Gamma(Z \rightarrow \mu^+\mu^-)$	83.99(18) MeV [22]	83.986(68) MeV [22]
$\Gamma(Z \rightarrow \tau^+\tau^-)$	84.08(22) MeV [22]	83.796(67) MeV [22]
$\Gamma(Z \rightarrow \nu\bar{\nu})$	497.4(25) MeV [22]	501.435(45) MeV [23]
Observable	95% CL limit	SM prediction
$\mathcal{B}(Z \rightarrow e\mu)$	$2.62 \cdot 10^{-7}$ [24]	0
$\mathcal{B}(Z \rightarrow e\tau)$	$5.04 \cdot 10^{-6}$ [25]	0
$\mathcal{B}(Z \rightarrow \mu\tau)$	$6.5 \cdot 10^{-6}$ [25]	0

**Table 3.** Measurements of the  $Z$  boson decay widths and limits on the LFV branching fractions as well as the corresponding SM predictions used in this analysis.

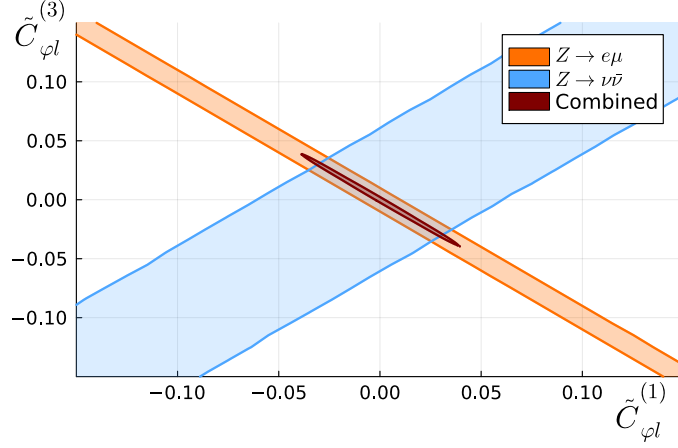


**Figure 2.** 90% credible regions for the two-dimensional fit in the  $\tilde{C}_{\phi l}^{(1)}-\tilde{C}_{\phi l}^{(3)}$  plane. The blue (orange) region is obtained from  $Z$  decays to neutrinos (charged leptons  $Z \rightarrow e\mu$ ). The red region presents a combined fit of both decays.

angle  $\theta$  normalized to the total one

$$A_{\text{FB}}^{\ell} = \frac{\sigma_{\text{F}}^{\ell} - \sigma_{\text{B}}^{\ell}}{\sigma_{\text{F}}^{\ell} + \sigma_{\text{B}}^{\ell}}, \quad (3.7)$$

where

$$\sigma_{\text{F}}^{\ell} = \int_0^1 d \cos \theta \frac{d\sigma(e^+e^- \rightarrow \ell^+\ell^-)}{d \cos \theta}, \quad \sigma_{\text{B}}^{\ell} = \int_{-1}^0 d \cos \theta \frac{d\sigma(e^+e^- \rightarrow \ell^+\ell^-)}{d \cos \theta}. \quad (3.8)$$

Defined as ratios of cross sections,  $A_{\text{FB}}^{\ell}$  benefit from partial cancellation of systematic uncertainties. Moreover, they are sensitive to the chiral structure of the  $Z$ -couplings and thus probe different combinations of Wilson coefficients than the decay rates. While  $A_{\text{FB}}^{\ell}$

is affected by  $\gamma$ -exchange and interference between the  $Z$  and  $\gamma$  contribution, LEP has defined a "pole" quantity which is corrected for these effects, denoted by  $A_{\text{FB}}^{0,\ell}$ . The latter is related to the  $Z$ -couplings as

$$\mathcal{A}_\ell = \frac{(g_L^\ell)^2 - (g_R^\ell)^2}{(g_L^\ell)^2 + (g_R^\ell)^2}, \quad (3.9)$$

via

$$A_{\text{FB}}^{0,\ell} = \frac{3}{4} \mathcal{A}_e \mathcal{A}_\ell. \quad (3.10)$$

Since there is no interference with the SM and in view of their strong constraints from  $Z$ -decays, we neglect contributions from electroweak dipole operators in  $A_{\text{FB}}^{0,\ell}$ . This probes and hence concerns only LFC-fits. To maintain consistency in the SMEFT expansion, we expand the forward-backward asymmetries in powers of the NP scale including terms up to order  $\Lambda^{-4}$ . Tab. 4 summarizes the measurements used in this analysis, alongside their corresponding SM predictions.

Four-lepton operators also contribute to the asymmetry parameters by modifying the  $e^+e^- \rightarrow \ell^+\ell^-$  cross section, schematically,

$$A_{\text{FB}}^{0,\ell} \sim \frac{3(\tilde{C}_{e\ell}^2 + \tilde{C}_{\ell\ell}^2 - \tilde{C}_{\ell e}^2 - \tilde{C}_{\ell e}^2)}{4(\tilde{C}_{e\ell}^2 + \tilde{C}_{\ell\ell}^2 + \tilde{C}_{\ell e}^2 + \tilde{C}_{\ell e}^2)}. \quad (3.11)$$

In the fit we include the full formula, which we again expand up to order  $\Lambda^{-4}$ , including SM contributions and terms with other SMEFT coefficients.

Observable	Measurement	SM prediction
$A_{\text{FB}}^{0,e}$	0.0145(25)	0.01627(27)
$A_{\text{FB}}^{0,\mu}$	0.0169(13)	0.01627(27)
$A_{\text{FB}}^{0,\tau}$	0.0188(17)	0.01627(27)

**Table 4.** Measurements and SM predictions of the  $Z$  boson forward-backward asymmetries [22].

### 3.2 $W$ -Boson Decays

In the SMEFT the partial decay width  $\Gamma(W \rightarrow \ell_i \nu_j)$  is given by [21]

$$\Gamma(W \rightarrow \ell_i \nu_j) = \frac{G_F m_W^3}{6\pi\sqrt{2}} \left( \left( \delta_{ij} + \tilde{C}_{ij}^{(3)} \right)^2 + \tilde{C}_{eW}^2 \right), \quad (3.12)$$

where the coefficients are evaluated at  $\mu \sim m_W$ . Since the neutrino flavor cannot be resolved experimentally, the observed decay width corresponds to the sum over all neutrino flavors

$$\Gamma(W \rightarrow \ell_i \nu) = \sum_j \Gamma(W \rightarrow \ell_i \nu_j), \quad (3.13)$$

where only  $i = j$  receives a SM contribution. As the Wilson coefficients contribute incoherently, we can nonetheless constrain all SMEFT coefficients at  $\mu = m_W$  simultaneously.

$\Gamma(W \rightarrow e\nu)$	$\Gamma(W \rightarrow \mu\nu)$	$\Gamma(W \rightarrow \tau\nu)$
0.226(5) GeV	0.228(5) GeV	0.225(6) GeV

**Table 5.** Experimental values of the partial widths  $\Gamma(W \rightarrow \ell\nu)$ . They are obtained by multiplying the branching fractions stated in Ref. [26] with the total  $W$  boson decay width of  $\Gamma_W = 2.085(42)$  GeV [23].

As experimental input, we employ partial decay widths rather than branching fractions. This choice avoids the need to expand the branching ratios in powers of  $\Lambda$ , since both, the partial and total decay widths can receive SMEFT contributions. The partial widths are obtained by multiplying the  $W$  boson branching fractions to charged leptons with the total  $W$  decay width,  $\Gamma_W = 2.085(42)$  GeV [23]. For the branching fractions, we use the most recent measurements of the CMS collaboration [26]. Results are listed in Tab. 5.

The decays  $W \rightarrow \ell\nu$  provide complementary constraints to the ones from the  $Z$ . Together, they resolve flat directions in the  $\tilde{C}_{eB}$ - $\tilde{C}_{eW}$  parameter space that arises in  $Z$  boson observables. This is illustrated for the example of an  $e\mu$ -specific fit in Fig. 3, where we show the 90% credible regions resulting from a two-dimensional fit of the Wilson coefficients. The blue (orange) region corresponds to constraints from the  $W \rightarrow e\nu$  decay ( $Z \rightarrow e\mu$  decay). The red region shows the result of a combined fit to both decay channels. The combinations significantly reduces the allowed parameter space and enables constraints on  $\tilde{C}_{eB}$ .

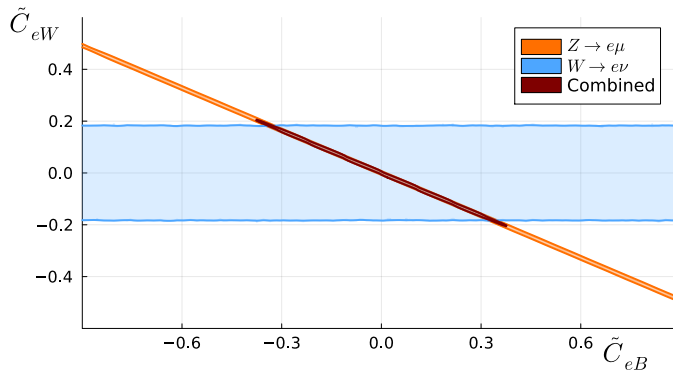


**Figure 3.** 90% credible regions for the two-dimensional fit in the  $\tilde{C}_{eB}$ - $\tilde{C}_{eW}$  plane for a lepton flavor specific analysis with only the  $e\mu$  coefficient switched on. The blue region is obtained from a fit to  $W \rightarrow e\nu$  decays, while the orange region is obtained from  $Z \rightarrow e\mu$ . The red region shows the combined fit.

### 3.3 Dilepton Production at LEP

The production of charged lepton pairs in electron-positron collisions allows to cleanly probe NP in the lepton sector. In addition to the contact four-lepton interactions, the process also receives contributions from vertex corrections induced by Higgs-current operators, as well as from dipole operators.

As experimental input we employ the differential measurements of the  $e^+e^- \rightarrow \ell^+\ell^-$  cross section for all flavors  $\ell = e, \mu, \tau$  by the DELPHI collaboration at  $\sqrt{s} = 207 \text{ GeV}$  [27]. The data is binned in terms of  $\cos\theta$ , where  $\theta$  is the angle between the outgoing lepton and the beam axis in the center-of-mass frame. We compute the SMEFT contributions to this process at tree-level using MATHEMATICA [28] in combination with the FEYN CALC [29–32] and `SmeftFR` v3.0 [33] packages. The coefficients inducing vector couplings, such as the four-lepton coefficients and the Higgs-current operators, induce contributions proportional to  $(1 \pm \cos\theta)^2$ , while the dipole operators induce contributions proportional to  $1 - \cos^2\theta$ . The angular distribution thus allows one to disentangle different chirality structures.

### 3.4 Drell–Yan Production

The Drell–Yan (DY) process refers to lepton production in hadron collisions,  $pp \rightarrow \ell^+\ell^-$  and  $pp \rightarrow \ell\nu$ . In the SM, it arises at tree-level from exchange of electroweak bosons. In contrast to the  $Z, W$  boson decays and dilepton production at LEP, the experimental measurements of DY are typically reported as differential distributions of event counts rather than differential cross sections. Thus, in order to confront the SMEFT to experimental data, hadronization, parton showering and detector effects need to be taken into account.

We compute the partonic cross section at LO using `MadGraph5_aMC@NLO` [34]. The hadronic cross section is obtained by convoluting the partonic cross section with the parton-luminosity-functions, defined as

$$\mathcal{L}_{q_i\bar{q}_j}(\tau) = \tau \int_{\tau}^1 \frac{dx}{x} [f_{q_i}(x, \mu_F) f_{\bar{q}_j}(\tau/x, \mu_F) + f_{\bar{q}_j}(x, \mu_F) f_{q_i}(\tau/x, \mu_F)] , \quad (3.14)$$

where  $f_{q_i}$  and  $f_{\bar{q}_j}$  denote the parton-distribution-functions (PDFs) of the incoming quarks  $q_i$  and  $\bar{q}_j$ , respectively, and  $\tau = \frac{\hat{s}}{s}$ , with  $\hat{s}$  the partonic and  $s$  the hadronic center-of-mass energy. The resulting hadronic cross section is given by

$$\sigma = \sum_{ij} \int \frac{d\tau}{\tau} \mathcal{L}_{q_i\bar{q}_j}(\tau) \hat{\sigma}(\tau s) . \quad (3.15)$$

As a result, the DY process probes a wide range of initial-state quark combinations. Since the different quark flavor contribute incoherently, we can simultaneously constrain various flavor combinations of the four-fermion operators. Due to the structure of the PDFs, the process is most sensitive to the light quarks of the first generation,  $u$  and  $d$ , which constitute

the valence quarks of the proton. Second-generation quarks,  $s$  and  $c$ , enter as sea quarks and are thus less relevant, while third-generation quarks,  $b$  and  $t$ , are strongly suppressed by their PDFs. In particular, the top quark is too heavy to significantly affect the DY process at LHC energies, and we therefore neglect its contribution in this analysis.

We employ the leading-order Monte Carlo variant of the NNPDF4.0 PDF sets [35, 36] as implemented in LHAPDF 6 [37]. The hadronic cross sections are computed numerically using the MadGraph5\_aMC@NLO [34] framework. Parton showering and hadronization are handled by Pythia8 [38], while detector effects are simulated using the parametric detector simulation framework Delphes [39]. The DY observables considered in this work, including the integrated luminosity, the number of bins and the corresponding experimental reference are summarized in Tab. 6.

The DY process is sensitive to a variety of different SMEFT operators, including the semileptonic four-fermion operators, which particularly benefit from the energy enhancement in the tails of the kinematic distributions, scaling with the partonic center-of-mass energy  $\hat{s}$  as  $\hat{s}/\Lambda^2$  [40]. Contributions from electroweak dipole operators and Higgs-current operators scale as  $\sqrt{\hat{s}}v/\Lambda^2$  and  $v^2/\Lambda^2$ , respectively<sup>3</sup>. In our MFV setup, tensor and scalar operators do not contribute to the DY process, since they couple exclusively to quark bilinears involving the top quark, which does not enter the partonic cross section at LHC energies.

Process	Observable	Integrated Luminosity	# Bins	Experiment	Reference
$pp \rightarrow ee$	$\frac{d\sigma}{dm_{ee}}$	137 fb <sup>-1</sup>	117	CMS	[41]
$pp \rightarrow \mu\mu$	$\frac{d\sigma}{dm_{\mu\mu}}$	140 fb <sup>-1</sup>	48	CMS	[41]
$pp \rightarrow \tau\tau$	$\frac{d\sigma}{dm_T^{\text{tot}}}$	139 fb <sup>-1</sup>	4	ATLAS	[42]
$pp \rightarrow e\mu$	$\frac{d\sigma}{dm_{e\mu}}$	139 fb <sup>-1</sup>	4	ATLAS	[42]
$pp \rightarrow e\tau$	$\frac{d\sigma}{dm_{e\tau}}$	139 fb <sup>-1</sup>	4	ATLAS	[42]
$pp \rightarrow \mu\tau$	$\frac{d\sigma}{dm_{\mu\tau}}$	139 fb <sup>-1</sup>	4	ATLAS	[42]
$pp \rightarrow e\nu$	$\frac{d\sigma}{dm_T}$	139 fb <sup>-1</sup>	65	ATLAS	[43]
$pp \rightarrow \mu\nu$	$\frac{d\sigma}{dm_T}$	139 fb <sup>-1</sup>	54	ATLAS	[43]
$pp \rightarrow \tau\nu$	$\frac{d\sigma}{dm_T}$	138 fb <sup>-1</sup>	18	CMS	[44]

**Table 6.** Drell–Yan observables considered in this work.

### 3.5 Top-Quark Pair-Production in Association with Leptons

We incorporate constraints from top-quark pair-production in association with a charged lepton pair,  $pp \rightarrow t\bar{t}\ell^+\ell^-$ . This process provides unique sensitivity to semileptonic four-

<sup>3</sup>Gluon dipole operators, which contribute to more generalized DY processes into missing energy with full energy-enhancement  $\hat{s}/\Lambda^2$  [8] are not considered in this work, see Tab. 1.

fermion operators involving right-handed couplings to the top quark. While left-handed couplings can be probed through other observables via the  $SU(2)_L$  relation between the top and bottom quarks, the  $t\bar{t}\ell\ell$  process constitutes the only direct collider probe of third-generation right-handed up-type quark Wilson coefficients. It therefore tests the MFV-expansion beyond leading order in the right-handed sector, parameterized by the ratio  $r_R$  in Eq. (2.5). Moreover, within the MFV framework, the  $t\bar{t}\ell\ell$  process is the only observable that constrains directly, at tree level, the scalar and tensor coefficients  $\tilde{C}_{lequ}^{(1)}$  and  $\tilde{C}_{lequ}^{(3)}$ . As we neglect light fermion Yukawas, the couplings of these coefficients to the light quarks vanish. The scalar and tensor operators, however, are indirectly constrained by their RG mixing onto the dipole operators  $O_{eW}$  and  $O_{eB}$ , e.g. see [45].

As experimental input, we use two-dimensional likelihood scans of Wilson coefficients provided by the ATLAS collaboration [11], based on global fits to  $t\bar{t}ee$  and  $t\bar{t}\mu\mu$  data. We interpolate these likelihood scans using radial basis function (RBF) interpolation to obtain continuous likelihood functions.

## 4 Flavor Observables

We discuss constraints from the anomalous magnetic moments of leptons (Sec. 4.1), various lepton decays (Sec. 4.2), and leptonic and semileptonic meson decays (Sec. 4.3).

### 4.1 Anomalous Magnetic Moments of Leptons

The anomalous magnetic moments (AMMs), denoting the deviation of the magnetic moment from the Dirac value  $a_\ell = \frac{g_\ell - 2}{2}$ , are among the most precisely measured quantities in particle physics for the light leptons. The AMM of the  $\tau$  lepton, on the other hand, is less precisely known due to the short lifetime of the  $\tau$  and resulting experimental challenges, so that at present only limits on the  $\tau$  AMM exist. Recent determinations and SM predictions of the AMMs are given in Tab. 7.

Observable	Measurement	SM Prediction
$a_e$	$1159.65218062(12) \cdot 10^{-6}$ [23]	$1159.65218161(23) \cdot 10^{-6}$ [46] <sup>†</sup>
$a_\mu$	$1165.92071(13) \cdot 10^{-6}$ [10]	$1165.92033(62) \cdot 10^{-6}$ [9]
$a_\tau$	$-0.057 < a_\tau < 0.024$ (95%CL) [47]	$1177.21(5) \cdot 10^{-6}$ [48]

**Table 7.** Measurements of the lepton AMMs and SM predictions. <sup>†</sup> From measurement of  $\alpha_e$  in Caesium. The Rubidium-based one differs in 10th digit.

In the LEFT, the contribution to the AMM of a charged lepton is given by

$$a_\ell^{\text{LEFT}} = \frac{2m_\ell}{\sqrt{\pi}\alpha_{\text{em}}} \mathcal{C}_{e\gamma}^{\ell\ell}, \quad (4.1)$$

where the Wilson coefficient is evaluated at the scale  $\mu = 2 \text{ GeV}$ . This choice serves as a lower limit for the RGE in order to avoid potential QCD-related divergences.

The tree level matching of the LEFT dipole coefficient  $\mathcal{C}_{e\gamma}$  onto the SMEFT reads

$$\mathcal{C}_{e\gamma} = \frac{1}{\sqrt{2}v} \left( -\sin\theta_W \tilde{C}_{eW} + \cos\theta_W \tilde{C}_{eB} \right). \quad (4.2)$$

This implies a flat direction in the parameter space, as contributions from the dipole operators  $O_{eW}$  and  $O_{eB}$  can cancel each other. This degeneracy can be lifted by combining constraints from additional observables, such as  $Z$  and  $W$  boson decays, which probe different linear combinations of Wilson coefficients. The scalar and tensor operators also contribute to the AMMs via their RG-mixing and at 1-loop. In total, the impact of the tensor  $O_{lequ}^{(3)}$  is bigger than the one of the scalar operator  $O_{lequ}^{(1)}$  [45].

## 4.2 Lepton Decays

We discuss constraints from LFV radiative lepton decays, LFV decays involving four leptons, and charged-current lepton decays.

### 4.2.1 Radiative LFV Lepton Decays

While the AMMs constrain the lepton-flavor-conserving (LFC) electroweak dipole coefficients, the corresponding LFV couplings are bounded by radiative lepton decays. In the LEFT framework, the branching fraction for the decay  $\ell_i \rightarrow \ell_j \gamma$  is given by

$$\mathcal{B}(\ell_i \rightarrow \ell_j \gamma) = \frac{m_{\ell_i}^3}{4\pi\Gamma_{\ell_i}} \left( |\mathcal{C}_{e\gamma}|^2 + |\mathcal{C}_{e\gamma}|^2 \right), \quad (4.3)$$

where  $\Gamma_{\ell_i}$  denotes the total decay width of the initial-state lepton. The SM contribution to this decay is negligible, as it is highly suppressed by the smallness of neutrino masses. Tab. 8 summarizes the current experimental limits on the branching fractions.

	$\mathcal{B}(\mu \rightarrow e\gamma)$	$\mathcal{B}(\tau \rightarrow e\gamma)$	$\mathcal{B}(\tau \rightarrow \mu\gamma)$
90% CL limit	$4.2 \cdot 10^{-13}$ [49]	$3.3 \cdot 10^{-8}$ [50]	$4.2 \cdot 10^{-8}$ [51]

**Table 8.** Current limits on the branching fractions of radiative, LFV lepton decays, all at 90% CL.

### 4.2.2 LFV Decays involving four charged leptons

LFV decays of the form  $\ell_i \rightarrow \ell_j \ell_k \ell_l$  are null tests of the SM. In the LEFT, the decay  $\ell_i \rightarrow \ell_j \bar{\ell}_k \ell_l$  is induced by the four-lepton operators  $\mathcal{Q}_{ee}^{V,LL}$ ,  $\mathcal{Q}_{ee}^{V,RR}$ , and  $\mathcal{Q}_{ee}^{V,LR}$ , as well as by

photon exchange via the LFV components of the dipole operator  $\mathcal{Q}_{e\gamma}$  for  $j = k$ . The four-lepton operators receive matching contributions from the SMEFT four-lepton operators  $O_{ee}$ ,  $O_{ll}$  and  $O_{le}$  as well as from the Higgs-current operators  $O_{\varphi l}^{(1)}$ ,  $O_{\varphi l}^{(3)}$ , and  $O_{\varphi e}$  at tree-level. We compute the LEFT contributions following Refs. [52–54]. Tab. 9 summarizes the current experimental limits on the branching fractions of LFV lepton decays at 90% CL. Note, the decays  $\tau^- \rightarrow e^+ \mu^- \mu^-$  and  $\tau^- \rightarrow \mu^+ e^- e^-$  violate two units of lepton flavor.

Observable	Limit	Ref.	Observable	Limit	Ref.
$\mathcal{B}(\tau^- \rightarrow e^- e^+ e^-)$	$2.7 \cdot 10^{-8}$	[55]	$\mathcal{B}(\tau^- \rightarrow \mu^- \mu^+ \mu^-)$	$2.1 \cdot 10^{-8}$	[55]
$\mathcal{B}(\tau^- \rightarrow e^- \mu^+ \mu^-)$	$2.7 \cdot 10^{-8}$	[55]	$\mathcal{B}(\tau^- \rightarrow e^+ \mu^- \mu^-)$	$1.7 \cdot 10^{-8}$	[55]
$\mathcal{B}(\tau^- \rightarrow \mu^- e^+ e^-)$	$1.8 \cdot 10^{-8}$	[55]	$\mathcal{B}(\tau^- \rightarrow \mu^+ e^- e^-)$	$1.5 \cdot 10^{-8}$	[55]
$\mathcal{B}(\mu^- \rightarrow e^- e^+ e^-)$	$1.0 \cdot 10^{-12}$	[56]			

**Table 9.** Experimental upper 90% CL limits on the branching fractions of LFV lepton decays.

### 4.2.3 Semileptonic $\tau$ Decays

The decay rate of the  $\tau$  lepton for a (charged-current) process involving a pseudoscalar meson  $P$  and a neutrino is given by

$$\Gamma(\tau \rightarrow \nu_i P) = \frac{m_\tau^3}{128\pi} f_P^2 \left(1 - \frac{m_P^2}{m_\tau^2}\right)^2 |\mathcal{C}_{i3kl}^{V,LL}|^2, \quad (4.4)$$

where  $f_P$  is the meson decay constant and  $m_P$  the meson mass. In the SM,  $\mathcal{C}_{vedu}^{V,LL}$  receives contributions from  $W$  boson exchange. The SM contribution can be read off from the matching conditions given in App. C. In the computation of the SM predictions we follow Refs. [57–59]. Meson masses are taken from Ref. [23], while the corresponding decay constants are listed in Appendix A, Tab. 25. The resulting SM predictions are presented in Tab. 10, together with the current experimental values.

Observable	Measurement	SM Prediction
$\Gamma(\tau^- \rightarrow \pi^- \bar{\nu})$	$2.453(12) \cdot 10^{-13}$ GeV [59]	$2.451(33) \cdot 10^{-13}$ GeV
$\Gamma(\tau^- \rightarrow K^- \bar{\nu})$	$1.578(23) \cdot 10^{-14}$ GeV [59]	$1.618(13) \cdot 10^{-14}$ GeV

**Table 10.** Experimental values and SM predictions of the partial widths of semileptonic  $\tau$  decays.

We compute the LFV (neutral-current) semileptonic  $\tau$  decay rates,  $\Gamma(\tau \rightarrow \ell_i M)$ , following Refs. [54, 60]. The decay to a pseudoscalar  $P$  probes  $|\mathcal{C}_{eq}^{V,RR} - \mathcal{C}_{qe}^{V,LR}|^2$  and  $|\mathcal{C}_{qe}^{V,LL} - \mathcal{C}_{eq}^{V,RL}|^2$ , while the decay rate to a vector meson  $V$  probes the orthogonal combinations  $|\mathcal{C}_{eq}^{V,RR} + \mathcal{C}_{qe}^{V,LR}|^2$  and  $|\mathcal{C}_{qe}^{V,LL} + \mathcal{C}_{eq}^{V,RL}|^2$ . Combining both types of final state mesons thus allows to disentangle left- and right-handed operator contributions. Tab. 11 gives the limits on the semileptonic LFV  $\tau$  branching fractions at 90% CL used in this analysis.

$\ell M$	Limit	$\ell M$	Limit	$\ell M$	Limit
$e\pi^0$	$8.0 \cdot 10^{-8}$ [61]	$\mu\pi^0$	$1.1 \cdot 10^{-7}$ [62]	$e\eta$	$9.2 \cdot 10^{-8}$ [61]
$\mu\eta$	$6.5 \cdot 10^{-8}$ [61]	$e\eta'$	$1.6 \cdot 10^{-7}$ [61]	$\mu\eta'$	$1.3 \cdot 10^{-7}$ [61]
$e\rho$	$2.2 \cdot 10^{-8}$ [63]	$\mu\rho$	$1.7 \cdot 10^{-8}$ [63]	$e\omega$	$2.4 \cdot 10^{-8}$ [63]
$\mu\omega$	$3.9 \cdot 10^{-8}$ [63]	$eK^*$	$1.9 \cdot 10^{-8}$ [63]	$\mu K^*$	$2.9 \cdot 10^{-8}$ [63]
$e\bar{K}^*$	$1.7 \cdot 10^{-8}$ [63]	$\mu\bar{K}^*$	$4.3 \cdot 10^{-8}$ [63]	$e\phi$	$2.0 \cdot 10^{-8}$ [63]
$\mu\phi$	$2.3 \cdot 10^{-8}$ [63]				

**Table 11.** Experimental 90% CL. limits on the branching fractions of the decay  $\tau \rightarrow \ell M$ .

#### 4.2.4 Lepton Decays to dineutrinos

Charged lepton decays of the form  $\ell_i \rightarrow \ell_j \nu_k \bar{\nu}_m$  are mediated by  $W$ -boson exchange in the SM. In the LEFT framework, the partial decay widths are given by

$$\Gamma(\ell_i \rightarrow \ell_j \nu_k \bar{\nu}_m) = \frac{m_{\ell_i}^5}{1536\pi^3} \sum_{k,m} \left( \left| \mathcal{C}_{kmij}^{V,LL} \right|^2 + \left| \mathcal{C}_{kmij}^{V,LR} \right|^2 \right), \quad (4.5)$$

where the sum is over all neutrino flavors since they are not flavor-tagged. Their contributions add incoherently, allowing several flavor components to be constrained simultaneously. In the SM, only the LFC terms with  $i = k$  and  $j = m$  contribute. Tab. 12 summarizes the current experimental values and SM predictions for the decay rates of the charged lepton decays to dineutrinos.

Observable	Measurement	SM Prediction
$\Gamma(\mu^- \rightarrow e^- \nu \bar{\nu})$	$2.995984(3) \cdot 10^{-19}$ GeV [59]	$2.994(5) \cdot 10^{-19}$ GeV
$\Gamma(\tau^- \rightarrow e^- \nu \bar{\nu})$	$4.045(11) \cdot 10^{-13}$ GeV [59]	$4.028(7) \cdot 10^{-13}$ GeV
$\Gamma(\tau^- \rightarrow \mu^- \nu \bar{\nu})$	$3.936(11) \cdot 10^{-13}$ GeV [59]	$3.918(7) \cdot 10^{-13}$ GeV

**Table 12.** Experimental values and SM predictions of the  $\ell_i \rightarrow \ell_j \nu_k \bar{\nu}_m$  decay rates.

### 4.3 Meson Decays

We discuss leptonic and semileptonic meson decays and their sensitivity to different combinations of Wilson coefficients.

#### 4.3.1 Leptonic Meson Decays

The purely leptonic decays of a pseudoscalar meson  $P \rightarrow \ell_i \ell_j$  probe the combinations  $|\mathcal{C}_{q\ell}^{V,RR} - \mathcal{C}_{q\ell}^{V,LR}|^2$  and  $|\mathcal{C}_{q\ell}^{V,LL} - \mathcal{C}_{q\ell}^{V,RL}|^2$ , analogous to semileptonic  $\tau$  decays. In contrast,

the charged-current process  $P \rightarrow \ell\nu$  is sensitive to the coefficient  $\mathcal{C}_{\nu edu}^{V,LL}$ . Since neutral meson decays involve FCNC transitions, they are strongly suppressed in the SM by the GIM mechanism. With the additional lepton mass suppression from the chiral flip, most leptonic decays of neutral mesons are currently constrained only by experimental upper limits, with the exception of  $B_s \rightarrow \mu^+\mu^-$ , which is in good agreement with the SM prediction. Tab. 13 lists the leptonic decay modes of pseudoscalar mesons considered in this analysis. We do not include LFC decays of light mesons, as they are typically dominated by long distance contributions. Recall that in our MFV setup no up-type FCNCs are induced so no BSM contribution to FCNC  $D$ -meson decays is present.

Meson	final states	Meson	final states
$\pi^0$	$e\mu$	$\eta$	$e\mu$
$\eta'$	$e\mu$	$K_L$	$e\mu$
$B^0$	$ee, \mu\mu, \tau\tau, e\mu, e\tau, \mu\tau$	$B_s$	$ee, \mu\mu, \tau\tau, e\mu, e\tau, \mu\tau$
$\pi^+$	$e\nu, \mu\nu$	$K^+$	$e\nu, \mu\nu$
$D^+$	$e\nu, \mu\nu, \tau\nu$	$D_s^+$	$e\nu, \mu\nu, \tau\nu$
$B^+$	$e\nu, \mu\nu, \tau\nu$		

**Table 13.** Leptonic decay modes of pseudoscalar mesons considered in this analysis. The upper part lists the neutral mesons, while the lower part lists the charged mesons.

Leptonic decays of quarkonium states,  $V \rightarrow \ell\ell$ , probe the orthogonal combinations of Wilson coefficients,  $|\mathcal{C}_{eq}^{V,RR} + \mathcal{C}_{qe}^{V,LR}|^2$  and  $|\mathcal{C}_{qe}^{V,LL} + \mathcal{C}_{eq}^{V,RL}|^2$ , complementary to pseudoscalar meson decays. These decays also provide access to the quark-flavor-diagonal components of the Wilson coefficients, which dominate in the MFV setup.

Unlike pseudoscalar meson decays, vector meson decays are not affected by helicity suppression, such that the decay  $V \rightarrow \nu\bar{\nu}$  is allowed in the SM. The partial width reads [64]

$$\Gamma(V \rightarrow \bar{\nu}_i\nu_j) = \frac{f_V^2 m_V^3}{96\pi} \left| \mathcal{C}_{\nu q}^{V,LL} + \mathcal{C}_{\nu q}^{V,LR} \right|_{ij}^2, \quad (4.6)$$

which probes the semileptonic dineutrino operators of the LEFT and thereby complements SMEFT studies into charged leptons, as the processes are related in SMEFT by  $SU(2)_L$ . SM contributions can be read off from the matching conditions given in App. C.

The quarkonium decay modes considered in this analysis are given in Tab. 14. While the LFC modes with charged leptons are measured with high precision, the dineutrino and LFV modes are currently constrained only by upper limits, see Tab. 15.

Meson	Final States
$\Phi$	$e^+e^-, \mu^+\mu^-, e\mu, \nu\bar{\nu}$
$J/\Psi$	$e^+e^-, \mu^+\mu^-, e\mu, e\tau, \mu\tau, \nu\bar{\nu}$
$\Upsilon(1S)$	$e^+e^-, \mu^+\mu^-, \tau^+\tau^-, e\mu, e\tau, \mu\tau, \nu\bar{\nu}$

**Table 14.** Leptonic decay modes of vector mesons considered in this analysis.

Observable	Measurement	SM Prediction
$\mathcal{B}(\Phi \rightarrow \nu\bar{\nu})$	$1.7 \cdot 10^{-4}$ [23]	$3.22 \cdot 10^{-10}$
$\mathcal{B}(J/\Psi \rightarrow \nu\bar{\nu})$	$7.0 \cdot 10^{-4}$ [23]	$2.22 \cdot 10^{-8}$
$\mathcal{B}(\Upsilon(1S) \rightarrow \nu\bar{\nu})$	$3.0 \cdot 10^{-4}$ [23]	$9.28 \cdot 10^{-6}$

**Table 15.** 90% CL limits and SM predictions of  $(q\bar{q}) \rightarrow \nu\bar{\nu}$  branching ratios.

### 4.3.2 Semileptonic Meson Decays

Semileptonic  $P \rightarrow M\ell\nu$  and  $P \rightarrow M\ell\ell$  decays are sensitive to different combinations of Wilson coefficients compared to purely leptonic decays, allowing to disentangle chirality structures. As three-body decays, they offer also to measure angular distributions as functions of the hadronic momentum transfer  $q^2$ .

Tab. 16 lists the charged-current decays  $P \rightarrow M\ell\nu$  considered in this work. For these processes, we compute the SMEFT and SM predictions following Refs. [59, 65, 66]. The form factors used in the computation are listed in Appendix A, Tab. 26.

Meson	$e\nu$	$\mu\nu$	$\tau\nu$
$D^0$	$K^-, K^{*-}, \pi^-, \rho^-$	$K^-, K^{*-}, \pi^-, \rho^-$	
$D^+$	$\bar{K}^0, \bar{K}^{*0}, \pi^0, \eta, \rho, \omega$	$\bar{K}^0, \bar{K}^{*0}, \pi^0, \eta, \rho, \omega$	
$D_s$	$\phi, K^{*0}$	$\phi$	
$B^0$	$D^-, D^{*-}, \pi^-, \rho^-$	$D^-, D^{*-}, \pi^-, \rho^-$	$D^-, D^{*-}, \pi^-$
$B^+$	$\bar{D}^0, D^*, \pi^0, \rho^0$	$\bar{D}^0, D^*, \pi^0, \rho^0$	$\bar{D}^0, D^*$
$B_s$		$D_s^-, D_s^{*-}, K^-$	

**Table 16.** Semileptonic charged-current decays included in this analysis. The decay channels are grouped according to the lepton flavor of the final state.

The decay rate for  $P \rightarrow P'\ell\ell$  processes is typically significantly larger than that of purely leptonic decays  $P \rightarrow \ell\ell$ , as the former is not chirally-suppressed. The resulting higher statistics allow for differential measurements, which provide enhanced sensitivity to the Wilson coefficients. Due to the increased complexity in computing LEFT contributions

here, we utilize the Python package `flavio` [67] to evaluate the SMEFT contributions, and we adopt the corresponding SM predictions from the literature. The observables used in this analysis are given in Tab. 17.

Observables	Data	Ref	SM Ref
$\Gamma(B^0 \rightarrow \pi^0 e^+ e^-)$	90% CL limit	[68]	[69]
$\Gamma(B^0 \rightarrow \pi^0 \mu^+ \mu^-)$	90% CL limit	[68]	[69]
$\Gamma(B^+ \rightarrow \pi^+ e^+ e^-)$	90% CL limit	[70]	[69]
$\langle \frac{d\sigma}{dq^2} \rangle (B^+ \rightarrow \pi^+ \mu^+ \mu^-)$	9 bins	[71]	[72, 73]
$\Gamma(B^0 \rightarrow K^0 e^+ e^-)$	full kinematic range	[23]	[74]
$\langle \frac{d\sigma}{dq^2} \rangle (B^0 \rightarrow K^0 \mu^+ \mu^-)$	6 bins	[75]	[74]
$\Gamma(B^+ \rightarrow K^+ e^+ e^-)$	full kinematic range	[23]	[74]
$\langle \frac{d\sigma}{dq^2} \rangle (B^+ \rightarrow K^+ \mu^+ \mu^-)$	11 bins	[75]	[74, 76]
$\Gamma(B^+ \rightarrow K^+ \tau^+ \tau^-)$	90% CL limit	[77]	[74]

**Table 17.** Observables of  $P \rightarrow P' \ell_i^+ \ell_i^-$  decays considered in this analysis.

The semileptonic decay  $P \rightarrow V \ell \ell$ , involving a vector meson in the final state, features additional polarization degrees of freedom and thus offers a richer angular distribution. The various helicity amplitudes are commonly expressed in terms of observables such as the longitudinal polarization fraction  $F_L(q^2)$ , the forward–backward asymmetry  $A_{\text{FB}}(q^2)$ , and the normalized angular coefficients  $S_i(q^2)$  [78]. Many analyses further improve sensitivity by using optimized observables  $P_i^{(\prime)}(q^2)$  [79, 80], which are designed to reduce both experimental and theoretical uncertainties. For the computation of the SMEFT contributions, we employ the `flavio` package [67], while SM predictions are taken from the literature. We list the observables for the LFC semileptonic decays  $P \rightarrow V \ell_i^+ \ell_i^-$  in Tab. 18.

Process	Observables	Ref	SM Ref
$B^0 \rightarrow K^{*0} e^+ e^-$	$F_L, P_i^{(\prime)}$ (1 bin)	[81]	[82]
$B^0 \rightarrow K^{*0} \mu^+ \mu^-$	$F_L, P_i^{(\prime)}$ (8 bins)	[83]	[67, 82]
$B^0 \rightarrow K^{*0} \tau^+ \tau^-$	90% CL limit on $\mathcal{B}$	[84]	[67]
$B^+ \rightarrow K^{*+} e^+ e^-$	$\Gamma(B^+ \rightarrow K^{*+} e^+ e^-)$	[23]	[67]
$B^+ \rightarrow K^{*+} \mu^+ \mu^-$	$F_L, P_i^{(\prime)}$ (8 bins)	[85]	[67, 82]
$B_s \rightarrow \phi e^+ e^-$	$F_L, S_3$ (3 bins)	[86]	[67]
$B_s \rightarrow \phi \mu^+ \mu^-$	$F_L, S_3, S_4, S_7$ (5 bins)	[87]	[67]
$B_s \rightarrow K^* \mu^+ \mu^-$	$\Gamma(B_s \rightarrow K^* \mu^+ \mu^-)$	[88]	[89]

**Table 18.** Observables of  $P \rightarrow V \ell_i^+ \ell_i^-$  decays considered in this work.

Searches have also been conducted for LFV decays of the form  $P \rightarrow P' \ell_i \ell_j$  and  $P \rightarrow V \ell_i \ell_j$  with  $i \neq j$ . As there is no signal in the SM, only upper limits on the branching fractions are available. The channels included in our analysis are listed in Tab. 19.

Meson	$e\mu$	$e\tau$	$\mu\tau$
$B^0$	$\pi^0, K^0, K^{*0}$	$K^{*0}$	$K^{*0}$
$B^+$	$\pi^+, K^+, K^{*+}$	$\pi^+, K^+, K^{*+}$	$\pi^+, K^+$
$B_s$	$\phi$		

**Table 19.** Semileptonic LFV meson decays included in this work.

We also consider semileptonic decays into dineutrinos,  $P \rightarrow M \nu \bar{\nu}$ . In our MFV setup, FCNC decays of this type are sensitive only to the coefficient  $C_{\nu q}^{V,LL}$ , since no right-handed FCNCs are induced. We compute the SM and SMEFT predictions following Ref. [90].

The FCNC dineutrino decays are currently constrained only by upper limits, with the exceptions of  $K^+ \rightarrow \pi^+ \nu \bar{\nu}$  and  $B^+ \rightarrow K^+ \nu \bar{\nu}$ . The latter has recently been measured by the Belle II collaboration [91], yielding  $\mathcal{B}(B^+ \rightarrow K^+ \nu \bar{\nu}) = 2.3(0.7) \cdot 10^{-5}$  which deviates from the SM prediction of  $5.58(0.37) \cdot 10^{-6}$  [74] at the  $2.7\sigma$  level. The relevant observables are listed in Tab.20.<sup>4</sup>

Observable	Measurement [GeV]	SM Prediction [GeV]
$\Gamma(K^+ \rightarrow \pi^+ \nu \bar{\nu})$	$6.1(2.1) \cdot 10^{-27}$ [23]	$4.18(0.32) \cdot 10^{-27}$ [93]
$\Gamma(B^0 \rightarrow \pi^0 \nu \bar{\nu})$	$< 3.9 \cdot 10^{-18}$ [94]	$2.56(0.55) \cdot 10^{-20}$
$\Gamma(B^0 \rightarrow K^0 \nu \bar{\nu})$	$< 1.1 \cdot 10^{-17}$ [94]	$1.78(0.10) \cdot 10^{-18}$
$\Gamma(B^+ \rightarrow \pi^+ \nu \bar{\nu})$	$< 5.6 \cdot 10^{-18}$ [94]	$5.1(1.1) \cdot 10^{-20}$
$\Gamma(B^+ \rightarrow K^+ \nu \bar{\nu})$	$9.2(2.8) \cdot 10^{-18}$ [91]	$2.08(0.10) \cdot 10^{-18}$
$\Gamma(B^0 \rightarrow \rho^0 \nu \bar{\nu})$	$< 1.7 \cdot 10^{-17}$ [94]	$7.4(1.1) \cdot 10^{-20}$
$\Gamma(B^0 \rightarrow K^{*0} \nu \bar{\nu})$	$< 7.8 \cdot 10^{-18}$ [94]	$3.95(0.36) \cdot 10^{-18}$
$\Gamma(B^+ \rightarrow \rho^+ \nu \bar{\nu})$	$< 1.2 \cdot 10^{-17}$ [94]	$1.48(0.21) \cdot 10^{-19}$
$\Gamma(B^+ \rightarrow K^{*+} \nu \bar{\nu})$	$< 1.6 \cdot 10^{-17}$ [94]	$3.95(0.36) \cdot 10^{-18}$
$\Gamma(B_s \rightarrow \phi \nu \bar{\nu})$	$< 2.3 \cdot 10^{-15}$ [95]	$4.2(0.3) \cdot 10^{-18}$

**Table 20.** Measurements and 90% CL limits on the decay rates of semileptonic meson decays  $P \rightarrow M \nu \bar{\nu}$ , alongside the corresponding SM predictions. The upper (lower) part presents measurements into pseudoscalar (vector) mesons. Resonance contributions from  $B^+ \rightarrow M^+(\rightarrow \tau \nu) \nu$  affecting decays of charged  $B$ -mesons, see Sec. 6, are not included in the SM predictions.

<sup>4</sup>The BESIII collaboration has set an upper limit of  $\mathcal{B}(D^0 \rightarrow \pi^0 \nu \bar{\nu}) < 2.1 \cdot 10^{-4}$  [92]. As our MFV setup does not induce  $c \rightarrow u$  FCNCs, this bound gives no constraint in our analysis.

## 5 Global Analysis

In this section, we present the results of the global analysis. We outline the fit methodology and the underlying statistical framework in Sec. 5.1. We discuss the outcome of the fit, comparing results for individual lepton flavors with those from lepton-flavor-universal and lepton-flavor-democratic scenarios for different types of operators in Secs. 5.2-5.6. We examine the posterior distributions of the MFV ratios  $r_L$  and  $r_R$  (Sec. 5.7) and the fit results of the CKM matrix (Sec. 5.8). In Sec. 6 we use the posteriors from the global analysis to make predictions for the branching fractions of  $B \rightarrow P\nu\bar{\nu}$  and  $B \rightarrow V\nu\bar{\nu}$  decays.

### 5.1 Fit Methodology

We perform global fits to the Wilson coefficients of the SMEFT operators listed in Tab. 1, using rescaled Wilson coefficients  $\tilde{C}$ , see (2.2). For LFV interactions, the dipole, scalar and tensor coefficients  $\tilde{C}_{ij}$  and  $\tilde{C}_{ji}$  are treated as two independent degrees of freedom, whereas for vector operators, hermiticity imposes the relation  $\tilde{C}_{ij} = \tilde{C}_{ji}^*$ . We further include the four Wolfenstein parameters of the CKM matrix as nuisance parameters, along with the five MFV ratios defined in Eq. (2.5), for  $O_{lq}^{(1/3)}$ ,  $O_{qe}$ ,  $O_{lu}$ , and  $O_{eu}$ . In total, this results in 26 degrees of freedom for the LFC or universal fits, and 30 for LFV scenarios.

To constrain the high-dimensional parameter space, we adopt a Bayesian framework using the *EFTfitter* package [96], based on the Bayesian Analysis Toolkit (BAT.jl) [97, 98]. As a preparatory step, we perform prefits using Reactive Nested Sampling, as implemented in the *UltraNest* package [99], to determine suitable prior ranges for the Wilson coefficients. For the final fit, we employ uniform priors within the optimized ranges and use the Robust Adaptive Metropolis–Hastings (RAM) algorithm [100] to sample the posterior distribution of the Wilson coefficients. We run  $N_{\text{chains}} = 10$  independent chains, each with  $2 \cdot 10^6$  iterations, and discard the first 30% of samples as burn-in.

To present the outcome of the global fit to the full set of the 17 Wilson coefficients we discuss the constraints separately for the five, phenomenologically distinct classes: Higgs–current operators (Sec. 5.2), semileptonic four–fermion operators with vector couplings (Sec. 5.3), four–lepton operators (Sec. 5.4), leptonic dipole operators (Sec. 5.5), and scalar and tensor operators (Sec. 5.6).

### 5.2 Higgs-Current Operators

We consider the leptonic Higgs-current coefficients  $\tilde{C}_{\varphi l}^{(1)}$ ,  $\tilde{C}_{\varphi l}^{(3)}$  and  $\tilde{C}_{\varphi e}$ . Fig. 4 shows the 90% credible intervals for these Wilson coefficients for the different lepton-flavor scenarios. LFC coefficients are shown in red, LFV coefficients in blue, and lepton-flavor-universal scenarios in orange. All Wilson coefficients are consistent with zero, corresponding to the SM expectation. In addition, Fig. 5 shows the resulting lower bounds on the new-physics

scale  $\Lambda/\sqrt{C}$ . Numerical values of the 90% credible intervals for the Higgs-current Wilson coefficients are given in Tab. 28.

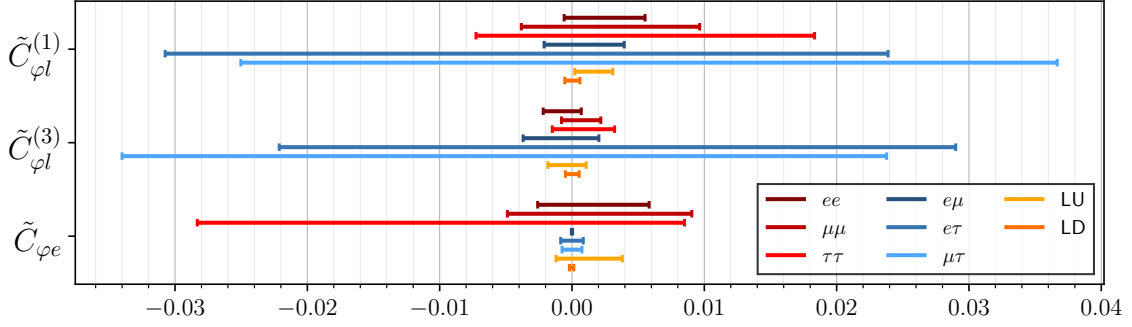


**Figure 4.** 90% credible intervals of the Wilson coefficients  $\tilde{C}_{\varphi l}^{(1)}$ ,  $\tilde{C}_{\varphi l}^{(3)}$  and  $\tilde{C}_{\varphi e}$  from lepton-flavor specific global SMEFT fits.

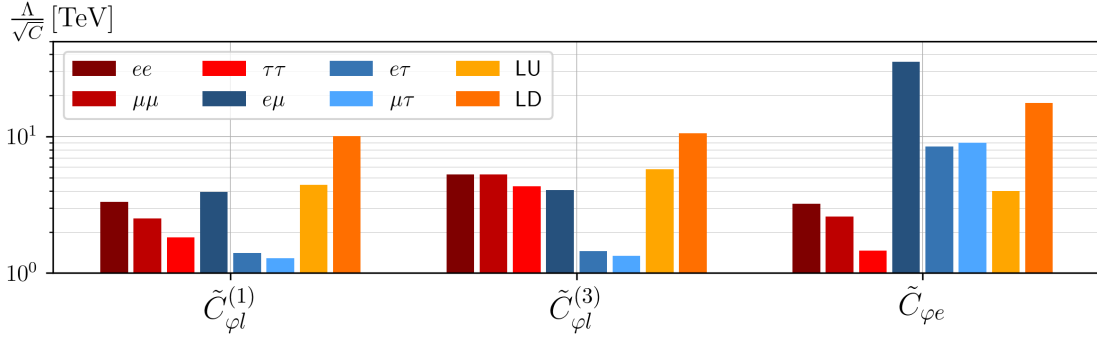


**Figure 5.** Lower bounds on  $\Lambda/\sqrt{C}$  at the 90% credible level for the Wilson coefficients  $\tilde{C}_{\varphi l}^{(1)}$ ,  $\tilde{C}_{\varphi l}^{(3)}$  and  $\tilde{C}_{\varphi e}$  from lepton-flavor specific global SMEFT fits.

The most stringent bounds are obtained in the  $e\mu$  scenario, with a 90% credible interval of  $[-4.8, 4.3] \cdot 10^{-5}$  for  $\tilde{C}_{\varphi e}$ , driven by the tight experimental limits on LFV decays. This corresponds to a reach of  $\Lambda/\sqrt{C} \gtrsim 30$  TeV. In contrast, the weakest bounds are found for the  $e\tau$  and  $\mu\tau$  couplings, where the upper bounds on  $\tilde{C}_{\varphi l}^{(1)}$  and  $\tilde{C}_{\varphi l}^{(3)}$  are  $|\tilde{C}| \lesssim 0.3$ , testing scales of order 1 TeV. In general, coefficients involving  $\tau$  leptons are less constrained due to the experimental challenges associated with reconstructing  $\tau$  decay products.

In the LD scenario, the resulting bound on  $\tilde{C}_{\varphi e}$  is weaker than in the  $e\mu$  fit alone. This effect arises because several channels included in the combination, such as  $Z \rightarrow \tau\tau$ , display small but statistically non-significant deviations from the SM expectation. These fluctuations broaden the overall posterior distribution and thereby relax the constraints compared to the more precise  $Z \rightarrow e\mu$  channel. This behavior is illustrated in Fig. 6, where we compare the posteriors of the  $e\mu$  and LD fits alongside the  $\tau\tau$  contribution (rescaled by a factor of 100 for visibility).

For the LFC couplings  $ee$ ,  $\mu\mu$ , and  $\tau\tau$ , we find that  $\tilde{C}_{\varphi l}^{(3)}$  is better constrained than  $\tilde{C}_{\varphi l}^{(1)}$ .

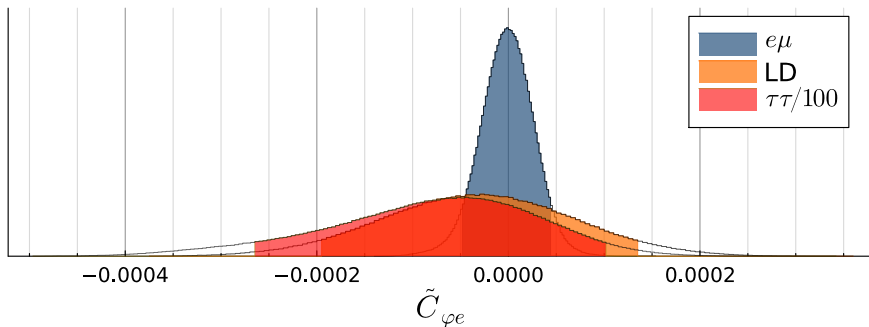


**Figure 6.** Posterior distributions in the  $e\mu$  fit (blue), the combined LD scenario (orange), and the  $\tau\tau$  channel (red, rescaled by a factor of 100 for visibility). While the  $e\mu$  fit yields the strongest constraint, the additional channels in the LD combination broadens the interval due to small, non-significant deviations, in particular from  $\tau\tau$  resulting in a weaker overall bound.

The reason is that the triplet operator  $O_{lq}^{(3)}$  also contributes to charged-current processes, whereas the singlet operator only contributes to neutral-currents. The coefficient  $\tilde{C}_{\varphi e}$  is constrained to a similar extent as  $\tilde{C}_{\varphi l}^{(1)}$ , since both affect the observable to a similar magnitude. The differences mainly arise from the interference term between the SM and SMEFT amplitudes, since the  $Z$  boson does not couple equally to left- and right-handed leptons.

In case of the LFV couplings  $e\mu$ ,  $e\tau$ , and  $\mu\tau$ , the bounds on  $\tilde{C}_{\varphi l}^{(1)}$  and  $\tilde{C}_{\varphi l}^{(3)}$  are of similar magnitude, whereas the constraints on  $\tilde{C}_{\varphi e}$  are significantly stronger. This distinction arises because the combination  $\tilde{C}_{\varphi l}^-$ , governing the  $Z \rightarrow \nu\bar{\nu}$  vertex, is only weakly constrained compared to the couplings of charged leptons proportional to  $\tilde{C}_{\varphi l}^+$ . Moreover, the LFV components of  $\tilde{C}_{\varphi l}^{(3)}$  do not interfere with the SM amplitude, rendering them less constrained. Consequently, the weak bounds on  $\tilde{C}_{\varphi l}^-$  remain unbroken by additional limits on  $\tilde{C}_{\varphi l}^{(3)}$ , allowing for a larger viable parameter space for both,  $\tilde{C}_{\varphi l}^{(1)}$  and  $\tilde{C}_{\varphi l}^{(3)}$ .

In the LU and LD scenarios, the bounds on  $\tilde{C}_{\varphi l}^{(1)}$  and  $\tilde{C}_{\varphi l}^{(3)}$  are significantly tighter than in the flavor-specific fits. This improvement results from the strong constraints on  $\tilde{C}_{\varphi l}^{(3)}$ , particularly from the  $\mu\mu$  coupling, which help to lift the degeneracy associated with  $\tilde{C}_{\varphi l}^-$  and thus enable the stringent limits on  $\tilde{C}_{\varphi l}^+$ , e.g. from  $Z \rightarrow e\mu$ , to be fully exploited.

To assess the impact of the different sectors, we perform single-coefficient fits in which all Wilson coefficients except for  $\tilde{C}_{\varphi l}^{(3)}$  are set to zero, and we consider one sector at a time. The resulting sensitivities are displayed in Fig. 7 for collider observables and in Fig. 8 for flavor data. We compare the lepton-flavor universal and the lepton-flavor democratic scenarios, with the latter including LFV observables. Overall, the strongest constraints arise from LFV lepton decays, which are probed with very high sensitivity. Since these processes are essentially null tests, the corresponding bounds are generally much tighter than those from lepton-flavor conserving observables. Among the latter, leptonic  $\ell_i \rightarrow \ell_j \nu\bar{\nu}$  decays and  $Z$ -pole measurements provide the most stringent constraints.

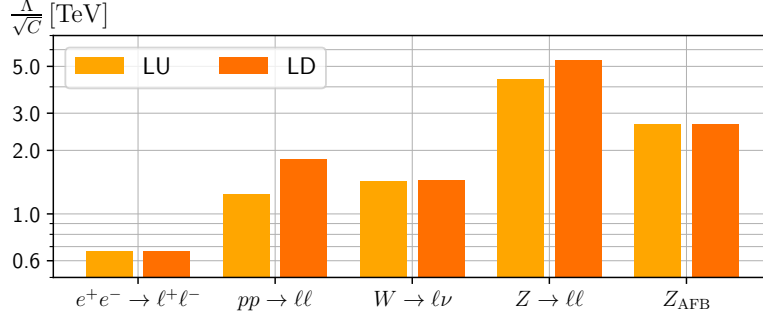


**Figure 7.** Lower bounds on  $\Lambda/\sqrt{C}$  at the 90% credible level for the Wilson coefficient  $\tilde{C}_{\varphi l}^{(3)}$  resulting from single-coefficient fits to individual sectors of collider observables. We compare fits in the LU scenario (yellow) to the LD scenario (orange).

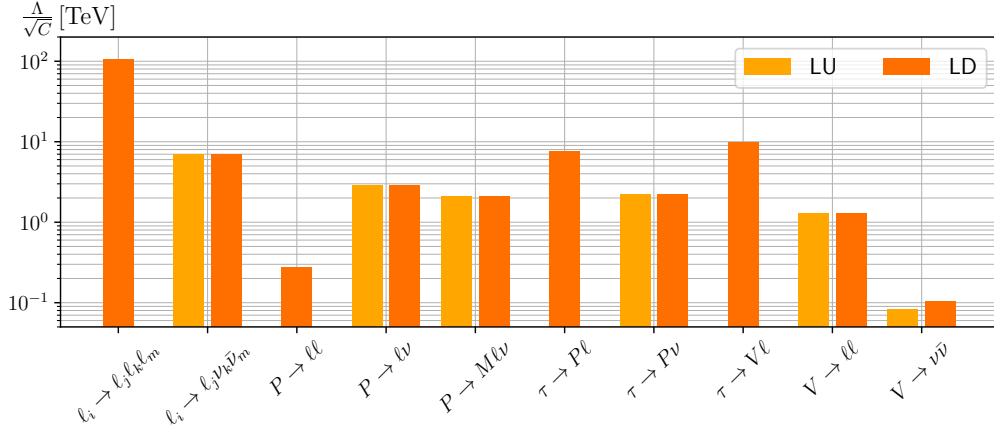


**Figure 8.** Lower bounds on  $\Lambda/\sqrt{C}$  at the 90% credible level for the Wilson coefficient  $\tilde{C}_{\varphi l}^{(3)}$  resulting from single-coefficient fits to individual sectors of flavor observables. We compare fits in the LU scenario (yellow) to the LD scenario (orange).

### 5.3 Semileptonic Four-Fermion Operators

We consider semileptonic four-fermion coefficients with vector couplings  $\tilde{C}_{lq}^{(1)}$ ,  $\tilde{C}_{lq}^{(3)}$ ,  $\tilde{C}_{qe}$ ,  $\tilde{C}_{lu}$ ,  $\tilde{C}_{eu}$ ,  $\tilde{C}_{ld}$  and  $\tilde{C}_{ed}$ . Fig. 9 shows the 90% credible intervals for these Wilson coefficients obtained from our global SMEFT fit. The numerical values are provided in Appendix D, Tabs. 29 and 30. The corresponding lower bounds on the NP scale  $\Lambda$  are shown in Fig. 10.

We find that the bounds on LFV coefficients are particularly stringent, probing NP scales of order  $\Lambda/\sqrt{C} \sim 10$  TeV. These limits arise primarily from flavor observables such as LFV  $\tau$  or meson decays, as well as from the analyses of LFV DY processes  $pp \rightarrow \ell_i \ell_j$ . The bounds on LFV coefficients are of similar strength for the different operators and we see only minor variations across the LFV lepton flavor scenarios.

In contrast, the bounds on LFC coefficients are generally weaker due to larger SM back-

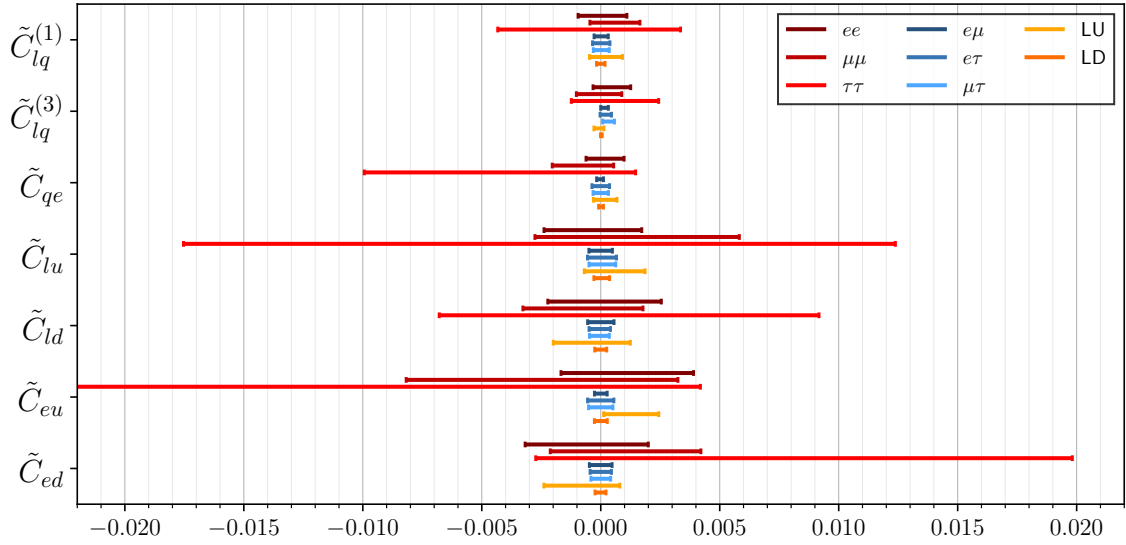


**Figure 9.** 90% credible intervals for the semileptonic four-fermion coefficients with vector structure.

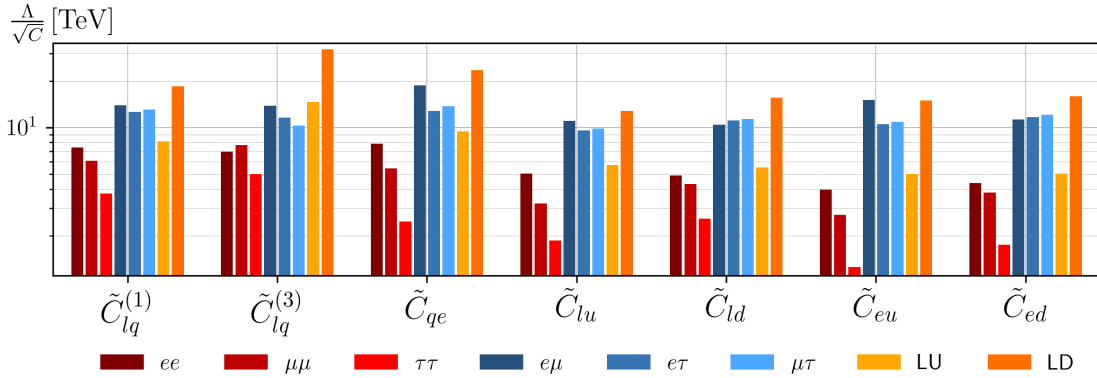


**Figure 10.** Lower bounds on  $\Lambda/\sqrt{C}$  at 90% obtained from the 90% credible intervals for the semileptonic four-fermion coefficients with vector structure.

grounds in the corresponding observables. In particular the  $\tau\tau$  channel has the weakest constraints. For the LFC coefficients, we observe that operators involving left-handed quark fields are more strongly constrained than their right-handed counterparts, as only the left-handed operators induce FCNCs in our MFV setup. Moreover, the operators with left-handed quarks and left-handed leptons,  $O_{lq}^{(1)}$  and  $O_{lq}^{(3)}$ , are particularly well constrained as they also contribute to dineutrino decays. The operator  $O_{qe}$  with right-handed lepton singlets, on the other hand, contributes only to processes involving charged leptons.

The limits on the Wilson coefficients in the LU and LD scenarios are slightly tighter than those in the lepton-flavor-specific fits, demonstrating the synergy across different flavor channels. This is particularly pronounced for the coefficients  $\tilde{C}_{lq}^{(1)}$  and  $\tilde{C}_{lq}^{(3)}$ , which are most affected by potential flat directions since they contribute via the linear combinations  $\tilde{C}_{lq}^{\pm}$

to many observables. The strongest bound in this class of coefficients is obtained for  $\tilde{C}_{lq}^{(3)}$  in the LD scenario with a 90% credible interval of  $[-0.86, 5.91] \cdot 10^{-5}$ , corresponding to a reach of 30 TeV for  $\Lambda/\sqrt{C}$ , far exceeding the direct limits from the LHC.

While most coefficients are consistent with zero within the 90% credible intervals, we find slight preferences for nonzero values in the fit results for  $\tilde{C}_{lq}^{(3)}$  in the  $\mu\tau$  scenario and for  $\tilde{C}_{eu}$  in the LU scenario. The corresponding 90% credible intervals are  $[0.78, 5.74] \cdot 10^{-4}$  and  $[0.12, 2.44] \cdot 10^{-3}$ , respectively. The shift in the LFV coefficient can plausibly be traced to mild enhancements in the highest  $p_T$  bin of  $pp \rightarrow \mu\tau$  production measured by ATLAS [42], together with upward fluctuations in the high- $p_T$  bins of  $pp \rightarrow \mu\nu$  [43], non-significant excesses in  $P \rightarrow \tau\nu$  and  $\tau \rightarrow K\nu$  decays, and the  $2.7\sigma$  deviation observed in the  $B^+ \rightarrow K^+\nu\bar{\nu}$  measurement by Belle II [91]. In contrast, for  $\tilde{C}_{eu}$  no single observable shows a comparable deviation, suggesting that the effect originates from the interplay of multiple observables and statistical fluctuations. This underlines the additional sensitivity that can be achieved through combined fits. Nevertheless, all coefficients remain compatible with zero at the  $3\sigma$  level.

In addition, we perform single-coefficient fits for  $\tilde{C}_{lq}^{(3)}$  within individual sectors to assess the relative impact of different data sets. The resulting limits on  $\Lambda/\sqrt{C}$  are shown in Fig. 11. The most stringent bounds arise from decays of the type  $P \rightarrow V\ell\ell$ , such as  $B \rightarrow K^*\mu\mu$ , reaching scales above 40 TeV in the LD scenario. The DY process  $pp \rightarrow \ell\ell$  also provides strong sensitivity, with limits above 10 TeV. In contrast, the weakest bounds are obtained from quarkonia decays to dineutrinos, as expected since only upper limits on their branching ratios are currently available.

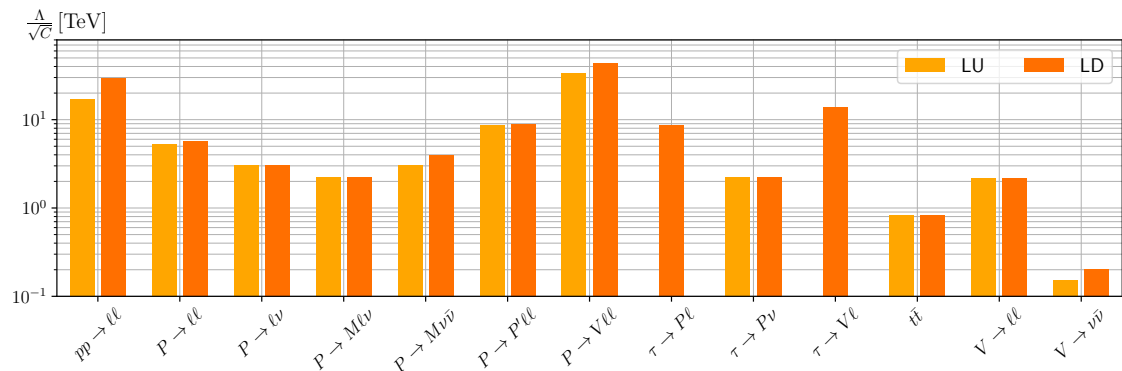


**Figure 11.** Lower bounds on  $\Lambda/\sqrt{C}$  at the 90% credible level for the Wilson coefficient  $\tilde{C}_{lq}^{(3)}$  resulting from single-coefficient fits to individual sectors. We compare fits in the LU scenario (yellow) to the LD scenario (orange).

#### 5.4 Four-Lepton Operators

We briefly discuss flavor possibilities of four-lepton coefficients  $\tilde{C}_{ll}$ ,  $\tilde{C}_{le}$ , and  $\tilde{C}_{ee}$ , each with four flavor indices  $ijkl$ , and how they enter the global fits.

In general, all flavors can be equal,  $i = j = k = l$ , which is LFC, and contributes to the  $ii$ -fit, the LU-fit, and the LD-fit. If two different flavors appear twice, abbreviated as 2+2, and  $i = j \neq k = l$  or  $i = l \neq j = k$ ,<sup>5</sup> these are LFC, and contribute to the LU-fit and the LD-fit. Examples for such  $iikk$ - or  $ijji$ -type induced processes are  $e^+e^- \rightarrow \mu^+\mu^-$  or  $\mu^- \rightarrow e^-\bar{\nu}_e\nu_\mu$ . Another 2+2-possibility are decays such as  $\mu^- \rightarrow e^-\bar{\nu}_\mu\nu_e$ , which violate lepton flavor by two units ( $i = k \neq j = l$ ), that is, with  $ijij$  indices. It contributes to the  $ij$ -fit, and the combined, LD-fit. The 3+1 case, that is  $i \neq j = k = l$ , or 2+1+1, corresponding to  $i \neq j \neq k = l$ , these are LFV, and contribute only to the LD-fit. This classification is a choice, as we like to stick to our definition that in the  $ij$ -fit only a single combination,  $ij$ , is switched on by NP. For bilinears this is of course unambiguous. As with two leptons, the concept of democracy with four leptons refers to all lepton flavor combinations contributing with a single coefficient. Since all operator flavors contribute to the LD-fit, we expect here the strongest bounds, followed by those from the LU-fit.

The four-lepton coefficients are directly constrained by LFC dilepton production at LEP and  $\ell \rightarrow \ell' l l$  decays into charged leptons  $l = \ell^\pm$  ( $\tilde{C}_{ll}$ ,  $\tilde{C}_{le}$ ,  $\tilde{C}_{ee}$ ) and with neutrinos  $l = \nu$  ( $\tilde{C}_{ll}$ ,  $\tilde{C}_{le}$ ). Hence, in the LFV  $ijij$ -case,  $\mathcal{O}_{ee}$  is unconstrained by the observables considered in this analysis.

Fig. 12 shows the 90% credible intervals for the Wilson coefficients across the different lepton-flavor scenarios; the corresponding lower bounds on  $\Lambda/\sqrt{C}$  are shown in Fig. 13. Numerical values of the credible intervals are provided in Tab. 31. Constraints on operators with four muons, or four taus arise predominantly from their RG-mixing onto leptonic penguin and semileptonic four-fermion operators.  $\mathcal{O}_{le}$  also enters the AMMs [45].

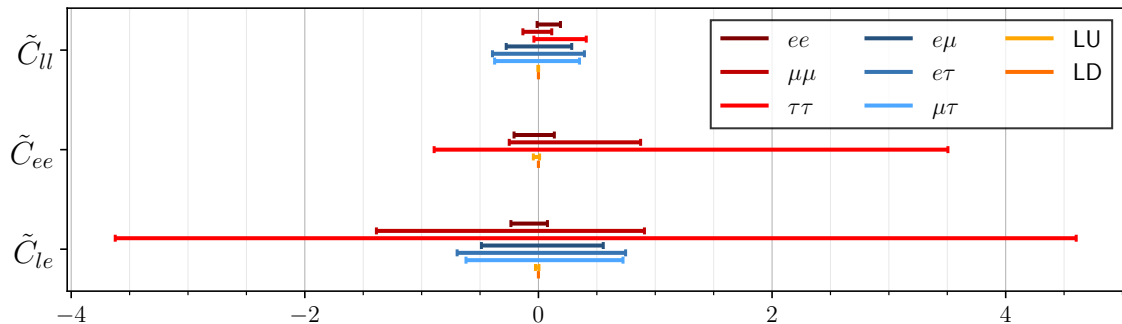


**Figure 12.** 90% credible intervals for the four-lepton coefficients.  $\tilde{C}_{ee}$  is not constrained in the LFV  $ij$ -case, see text, and no bounds are shown here.

We find, as anticipated, that the bounds in the LD and LU scenarios are significantly stronger than in the others. In particular, the LD-fit reaches scales of  $\Lambda/\sqrt{C} \sim 30$  TeV, whereas in the lepton-flavor-individual fits they are below 1 TeV.

<sup>5</sup>For  $\mathcal{O}_{ee}$  the coefficients with  $ijkl$  are identical to the ones with  $ilkj$  due to Fierzing rules.

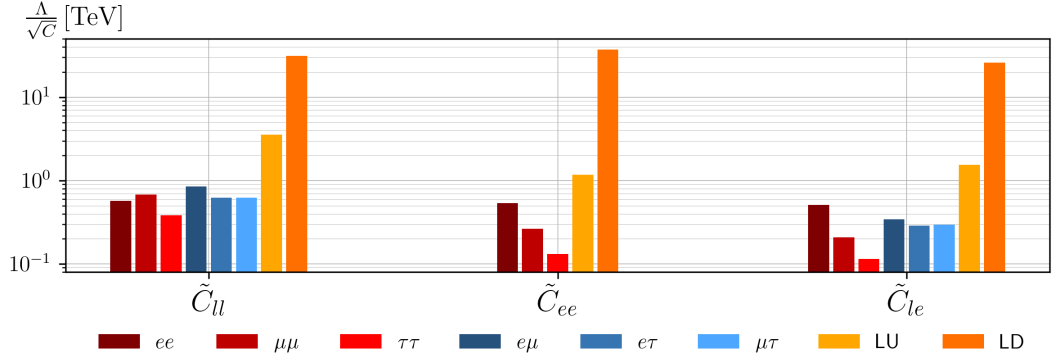


**Figure 13.** Lower bounds on  $\Lambda/\sqrt{C}$  for the four-lepton operators, see Fig. 12.

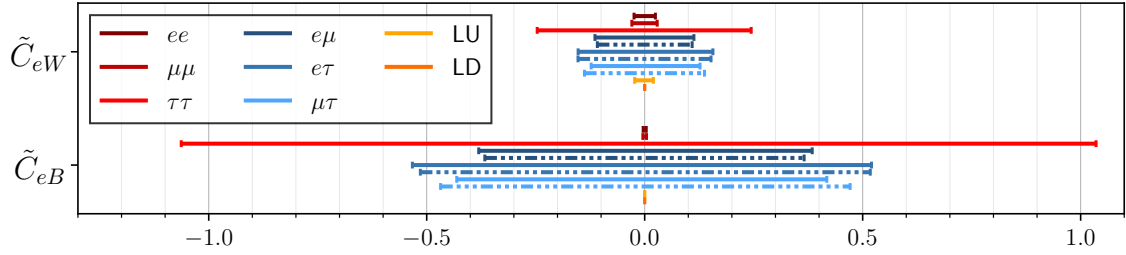


**Figure 14.** 90% credible intervals for the dipole coefficients  $\tilde{C}_{eB}$  and  $\tilde{C}_{eW}$  from global SMEFT fits. The solid lines show the bounds for the flavor components  $ij$  with  $i < j$ , while the striped lines show the bounds for  $ji$ .

## 5.5 Dipole Operators

The dipole coefficients  $\tilde{C}_{eB}$  and  $\tilde{C}_{eW}$  contribute to a variety of observables, including the AMMs of charged leptons,  $Z$  and  $W$  boson decays, and radiative lepton decays. Since the dipole operators are not Hermitian, the flavor components  $ij$  and  $ji$  with  $i < j$  contribute independently to the fit. While neutral-current processes are sensitive to  $|\tilde{C}_{ij}|^2 + |\tilde{C}_{ji}|^2$ , charged-current processes such as  $W \rightarrow \ell_i \nu_j$  receive contributions from only one of the two components, leading to slight differences in the resulting bounds.

Fig. 14 displays the 90% credible intervals for the Wilson coefficients obtained from the global SMEFT fit, while Fig. 15 shows the corresponding lower bounds on  $\Lambda/\sqrt{C}$ . Solid lines and bars denote the bounds for the  $ij$  coefficients with  $i < j$ , and striped lines and bars correspond to the  $ji$  components. Numerical values of the credible intervals are given in Tab. 32.

The coefficient  $\tilde{C}_{eW}$  is more tightly constrained than  $\tilde{C}_{eB}$  for the  $\tau\tau$  and LFV coefficients, as it contributes to a broader range of observables, including charged-current processes. It also dominates the linear combination  $\tilde{C}_{eZ}$ , which is strongly constrained by  $Z$ -pole observables. On the other hand, in the  $ee$  and  $\mu\mu$  channels, we find tighter limits for  $\tilde{C}_{eB}$  than for  $\tilde{C}_{eW}$ .

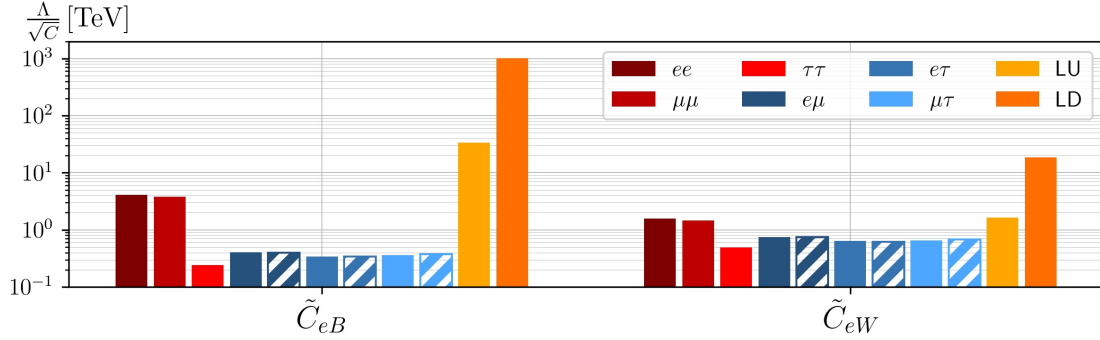


**Figure 15.** Lower bounds on  $\Lambda/\sqrt{C}$  for the dipole coefficients  $\tilde{C}_{eB}$  and  $\tilde{C}_{eW}$  obtained from the 90% credible intervals shown in Fig. 14. The solid bars show the bounds for the flavor components  $ij$  with  $i < j$ , while the striped bars show the bounds for  $ji$ .

This stems from the AMMs of the electron and muon, which are very sensitive to the LEFT dipole coefficient  $\mathcal{C}_{e\gamma}$ , to which the primary matching contribution comes from  $\tilde{C}_{eB}$ .

Synergies across the different observables significantly enhance sensitivity in the LD scenario. The 90% credible interval for  $\tilde{C}_{eB}$  is  $[-5.95, 0.11] \cdot 10^{-8}$ , corresponding to a lower bound on the NP scale of  $\Lambda/\sqrt{C} \sim 1000$  TeV, representing the strongest limit obtained in this analysis. This marks an improvement of more than two orders of magnitude compared to the individual flavor-specific fits.

The origin of this enhancement is that in single-flavor fits at least one linear combination of Wilson coefficients remains comparatively weakly constrained. In particular, the scalar and tensor coefficients  $\tilde{C}_{lequ}^{(1)}$  and  $\tilde{C}_{lequ}^{(3)}$  mix into the dipole operators under RGE running [12–14], which induces a degeneracy in most flavor-specific analyses. Direct constraints on these coefficients are currently available only from  $t\bar{t}l\bar{l}$  production, and thus limited to the  $ee$  and  $\mu\mu$  flavor channels. By combining the information from all lepton flavors, however, this degeneracy can be lifted, leading to substantially stronger bounds on the dipole coefficients. The global analysis fully exploits the stringent limits from LFV  $Z$  decays together with the precise measurements of the electron and muon anomalous magnetic moments.

Fig. 16 illustrates the impact of the individual sectors on the dipole bounds. We show the 90% credible limits on  $\Lambda/\sqrt{C}$  in a  $\tilde{C}_{eW}$ -only fit. The strongest bounds come from radiative lepton decays, which are experimentally very well constrained. In the LU fit, the best limit results from the anomalous magnetic moments, with a reach of several hundred TeV.

## 5.6 Scalar and Tensor Operators

The scalar and tensor operators  $O_{lequ}^{(1)}$  and  $O_{lequ}^{(3)}$  contribute only via their coupling to the top quark in our MFV framework. As a result, they are not directly constrained by DY production or flavor observables. The only direct experimental constraints come from  $t\bar{t}ee$  and  $t\bar{t}\mu\mu$  production [11]. Beyond these direct constraints,  $\tilde{C}_{lequ}^{(1)}$  and  $\tilde{C}_{lequ}^{(3)}$  are constrained only

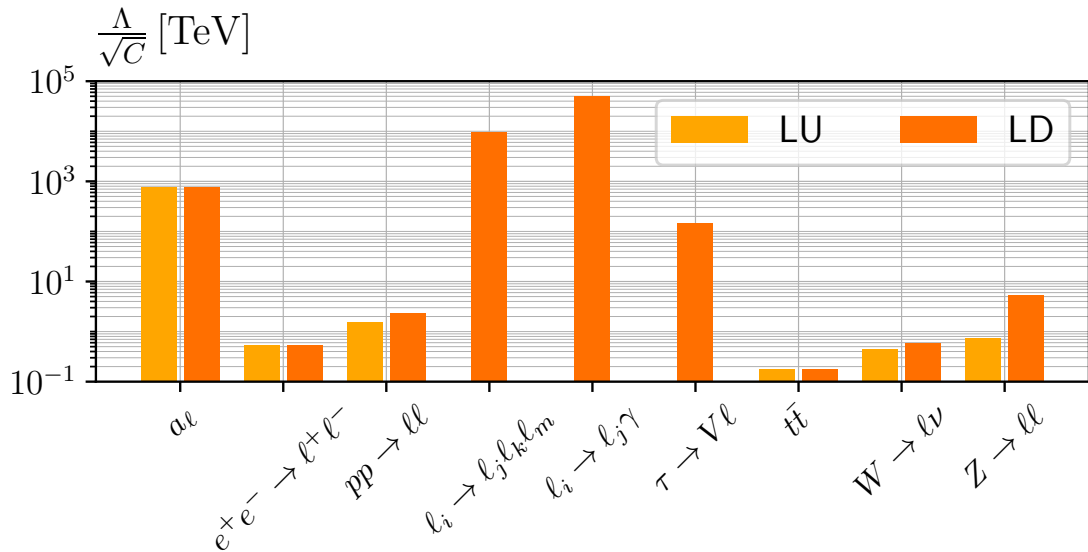


**Figure 16.** Lower bounds on  $\Lambda/\sqrt{C}$  at the 90% credible level for the Wilson coefficient  $\tilde{C}_{eW}$  resulting from single-coefficient fits to individual sectors. We compare fits in the LU scenario (yellow) to the LD scenario (orange).

via their RG-mixing with the electroweak dipoles  $\tilde{C}_{eW}$  and  $\tilde{C}_{eB}$ . Since the tensor operator mixes more strongly with the dipoles than the scalar operator, the resulting constraints on  $\tilde{C}_{lequ}^{(3)}$  are roughly an order of magnitude tighter than those on  $\tilde{C}_{lequ}^{(1)}$ .

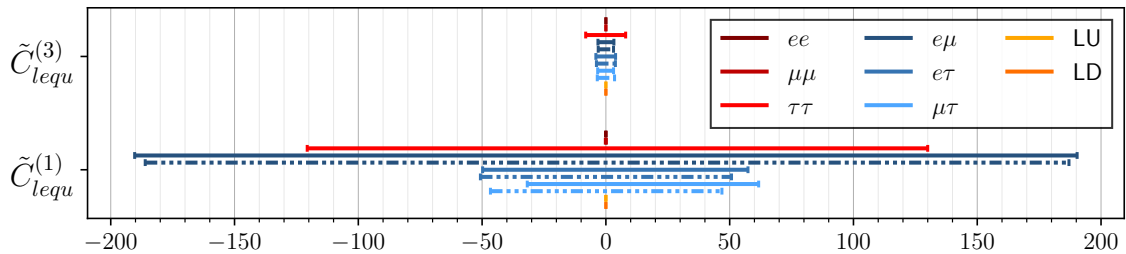


**Figure 17.** 90% credible intervals for  $\tilde{C}_{lequ}^{(1)}$  and  $\tilde{C}_{lequ}^{(3)}$  from global SMEFT fits. The solid lines show the bounds for the flavor components  $ij$  with  $i < j$ , while the striped lines show the bounds for  $ji$ .

Fig. 17 shows the 90% credible intervals for these Wilson coefficients, and Fig. 18 displays the corresponding lower bounds on  $\Lambda/\sqrt{C}$ . Numerical values are listed in Tab. 32 in Appendix D. The operators  $O_{lequ}^{(1)}$  and  $O_{lequ}^{(3)}$  are not Hermitian, so the flavor components  $ij$  and  $ji$  are treated as independent degrees of freedom. We indicate the bounds for  $ij$  with  $i < j$  using solid lines and bars, and those for  $ji$  with striped ones.

As expected from the AMMs and  $t\bar{t}l\bar{l}$  production the constraints on the  $ee$  and  $\mu\mu$  coefficients are significantly stronger than those on other flavor combinations. Consequently,

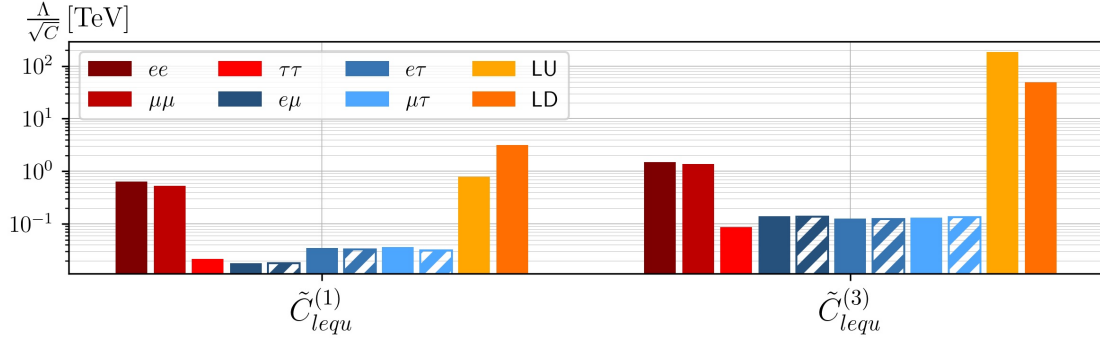


**Figure 18.** Lower bounds on  $\Lambda/\sqrt{C}$  for  $\tilde{C}_{lequ}^{(1)}$  and  $\tilde{C}_{lequ}^{(3)}$  from global SMEFT fits. The solid bars show the bounds for the flavor combinations  $ij$  with  $i < j$ , while the striped bars show the bounds for  $ji$ .

the bounds in the LU and LD scenarios also benefit from these constraints, reaching scales for the tensor coupling  $\tilde{C}_{lequ}^{(3)}$  of  $\Lambda/\sqrt{C} \sim 100$  TeV and  $\Lambda/\sqrt{C} \sim 50$  TeV, respectively. In contrast, the LFV coefficient  $\tilde{C}_{lequ}^{(1)}$  in the  $e\mu$  fit receives the weakest constraints among all coefficients in our analysis, with a 90% credible interval of  $[-193, 193]$ .

## 5.7 Testing MFV

We discuss the fit results for the parameters in the MFV expansion  $r_L$ ,  $r_R$  defined in Eq. (2.5). We include operator specific ratios  $r_L$  for coefficients with left-handed quarks,  $C_{lq}^+$ ,  $C_{lq}^-$  and  $C_{qe}$ , and ratios  $r_R$  for  $C_{lu}$  and  $C_{eu}$  with right-handed up-type quarks. The ratios  $r_L$  induce down-type FCNCs and non-universal couplings to the top and down-type quarks, while  $r_R$  only affect the right-handed  $t\bar{t}$ -couplings.

We find that the posterior distributions for  $r_R$  are flat and unbounded for both operators, indicating that the right-handed flavor structure is essentially unconstrained by the observables considered in this work. This is expected, as the only process probing  $r_R$  is  $t\bar{t}l\bar{l}$  production, whose constraints are orders of magnitude weaker than those from flavor observables and Drell–Yan production.

In contrast, the posterior distributions for  $r_L$  shown in Fig. 19 for the operators  $O_{lq}^+$  (left),  $O_{lq}^-$  (center) and  $O_{qe}$  (right) feature non-trivial, bells-type shapes. They differ in sharpness as a result of the sensitivity of the different lepton-flavor scenarios to the MFV structure. All distributions are consistent with  $r_L = 0$ , reflecting the fact that we currently do not see significant deviations from the SM in the flavor data, which would require next-to-leading terms in the MFV-expansion [6]. For the posterior of  $r_L^{qe}$ , note that the  $\tau\tau$ ,  $e\tau$  and  $\mu\tau$  distributions are slightly shifted towards negative values and peak around  $r \sim -1$ .

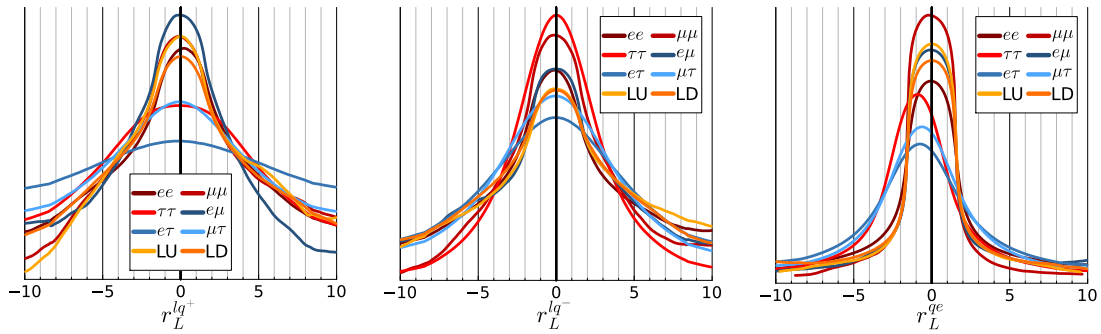


**Figure 19.** Posterior distributions for the MFV ratios  $r_L^{lq^+}$  (left),  $r_L^{lq^-}$  (middle) and  $r_L^{qe}$  (right). The color coding indicates the different lepton-flavor scenarios.

## 5.8 CKM Parameters

The parameters  $\lambda$ ,  $A$ ,  $\rho$ , and  $\eta$  of the Wolfenstein parameterization of the CKM matrix defined in Eq. (B.1) are treated as nuisance parameters in our fit. In Fig. 20, we show the mean values obtained from our global fits as black lines, along with the corresponding  $1\sigma$  credible intervals shown as colored bands for the various lepton-flavor scenarios. For comparison, we show the results of the CKMfitter group [101, 102], with mean values indicated by gray lines and the  $1\sigma$  intervals by gray bands.

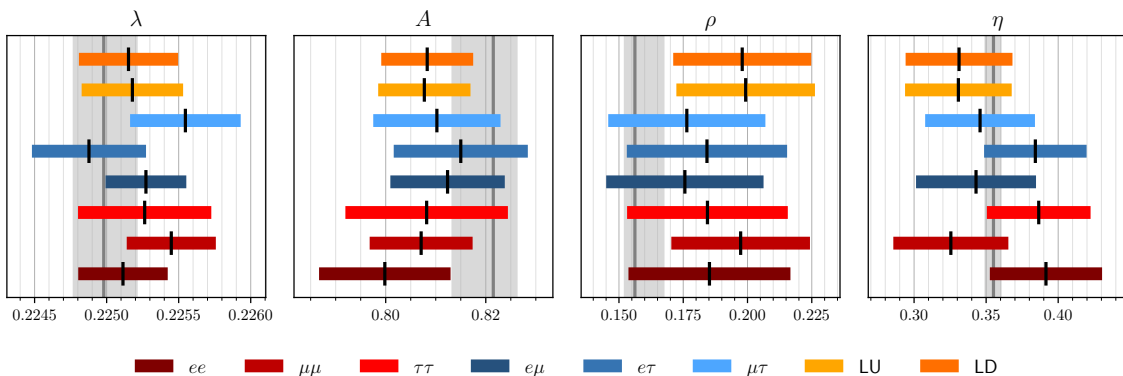


**Figure 20.**  $1\sigma$  credible intervals (colored) and mean values (black) for the CKM parameters  $\lambda$ ,  $A$ ,  $\rho$  and  $\eta$  from the global SMEFT fits. Results are shown for lepton-flavor diagonal (red), lepton-flavor universal (orange), and lepton-flavor violating (blue) scenarios. The results of the CKMfitter group [101, 102] are shown in gray.

Our results are compatible at  $1\sigma$  with those from the CKMfitter collaboration, except for small deviations in  $\rho$  in the LU, LD and  $\mu\mu$  fits. One also notices that the ranges for the parameter  $A$  from our fit tend towards smaller values compared to the CKMfitter results, while the values for  $\rho$  are slightly larger. For  $\lambda$  and  $\eta$ , on the other hand, we find the results vary more strongly across the different lepton-flavor scenarios.

Using Eq. (B.1), we compute the CKM matrix elements corresponding to the posterior distributions. The results are presented in Fig. 21, where black lines denote the mean values and colored bands indicate the  $1\sigma$  credible intervals. We again compare our results to those of the CKMfitter group, shown as gray lines and bands. As for the Wolfenstein

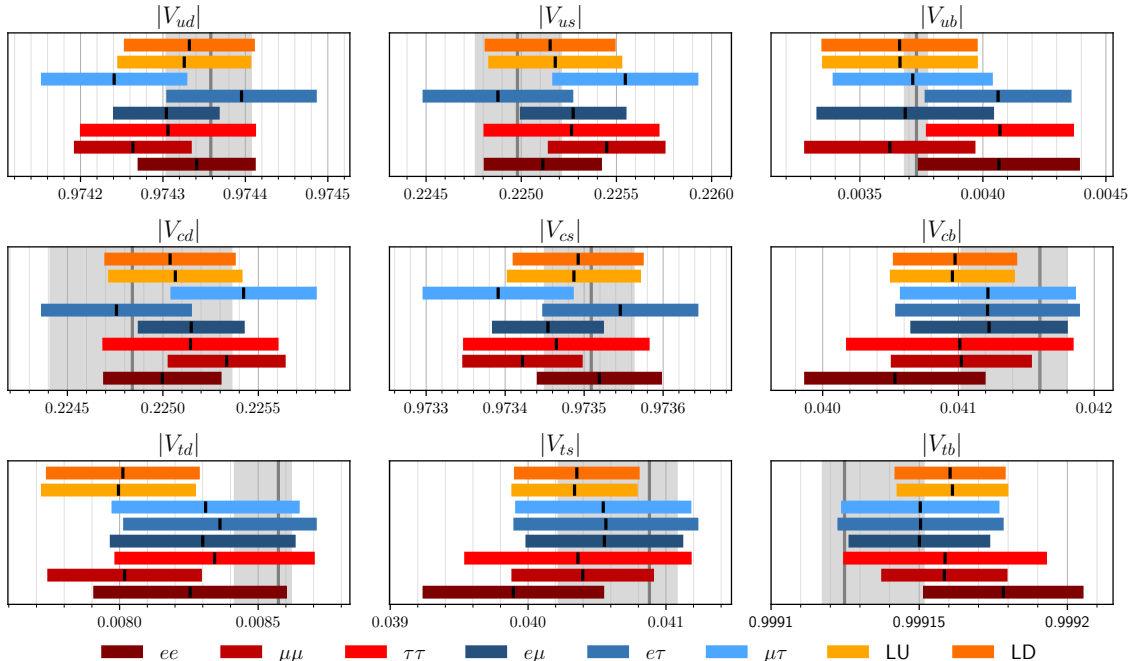


**Figure 21.** Absolute values of the CKM matrix elements derived from the posterior distributions of the Wolfenstein parameters  $\lambda$ ,  $A$ ,  $\rho$ , and  $\eta$ . Colored bands represent the  $1\sigma$  credible intervals, with mean values shown as black lines. Results are compared to those from the CKMfitter group [101, 102] (gray lines and bands).

parameters, we find overall good agreement between our results for the CKM elements and the CKMfitter values, with somewhat larger uncertainties. This is expected, since our analysis relies on fewer observables and includes additional sources of uncertainty from the Wilson coefficients. For the CKM element  $V_{cb}$ , we obtain slightly smaller values compared to CKMfitter. This originates from different input, see Tab. 27. Our analysis relies on exclusive determinations, whereas CKMfitter also includes inclusive measurements. The downward shift in  $V_{cb}$  therefore follows the well-established trend that exclusive determinations yield lower central values than inclusive ones [23, 103], and it also leads to a smaller value of  $A$  in our fits. The Wolfenstein parameter  $\rho$  obtained from our fits is larger than the CKMfitter results, mainly reflecting a shift in  $V_{td}$ . In particular, we observe a preference for smaller values of  $|V_{td}|$ , driven primarily by the neutral meson mass splitting  $\Delta M_d$ .

Across all parameters, we observe consistency among the different lepton-flavor scenarios, indicating that the impact of lepton-flavor universality on the CKM parameters is mild.

## 6 Predicting Dineutrino Modes

The only dineutrino branching fraction of a  $B$  meson decay evidenced to date is  $\mathcal{B}(B^+ \rightarrow K^+ \nu \bar{\nu})$ , by the Belle II collaboration [91]. For all other dineutrino modes, only upper limits exist at the level of few  $\cdot 10^{-5}$  [94, 104]. Belle II is expected to significantly improve the sensitivity to these channels, with the goal of measuring the branching fractions of  $B \rightarrow K^{(*)} \nu \bar{\nu}$  with a precision of roughly 10% [105].

Using the posterior distributions of the Wilson coefficients from the fits, we predict the branching fractions for these dineutrino modes within our MFV approach. Fig. 22 illustrates the resulting probability distributions for the decays  $B^0 \rightarrow K^{*0} \nu \bar{\nu}$  (top) and  $B^0 \rightarrow \rho^0 \nu \bar{\nu}$  (bottom) based on the lepton-flavor specific fit with only the  $\tau\tau$  coefficient switched on. We compare the predictions from the fit (blue) to the SM expectations (orange), the current experimental bounds (red), and the projected Belle II sensitivity [105], if available. The experimental upper limit  $\mathcal{B}(B^0 \rightarrow \rho^0 \nu \bar{\nu}) < 4.0 \cdot 10^{-5}$  [94] is not shown as it is outside the plot. Additional plots for the decays of charged  $B$  mesons as well as  $B^0 \rightarrow K^0 \nu \bar{\nu}$  and  $B^0 \rightarrow \pi^0 \nu \bar{\nu}$  are given in Appendix E.

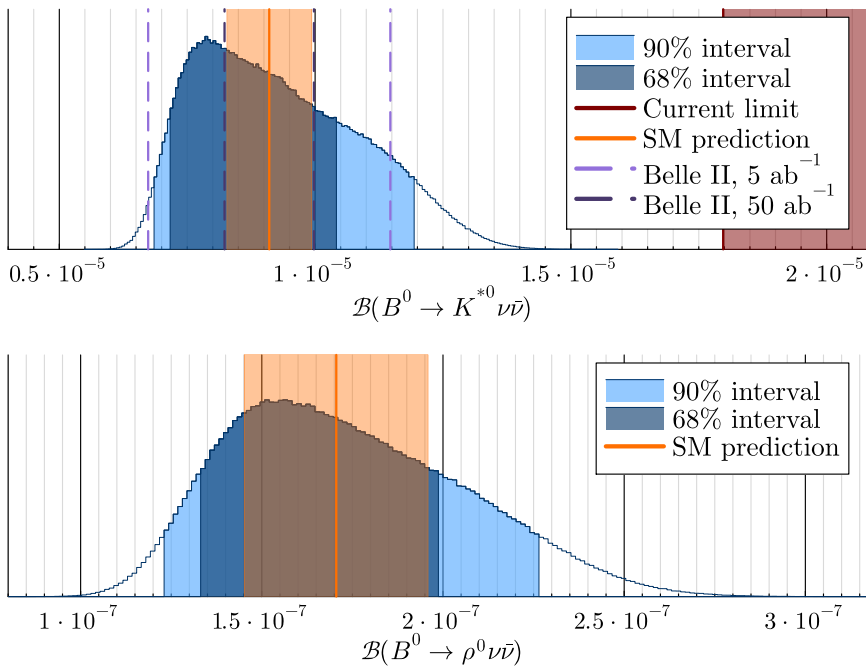


**Figure 22.** Predictions for the dineutrino decays  $B^0 \rightarrow K^{*0} \nu \bar{\nu}$  (top) and  $B^0 \rightarrow \rho^0 \nu \bar{\nu}$  (bottom) based on the global fit in the  $\tau\tau$  scenario. Colored bands (blue) indicate the 68% and 90% credible intervals; the orange band denotes the  $1\sigma$  SM prediction. The red area represents the current experimental 90% CL bound  $\mathcal{B}(B^0 \rightarrow K^{*0} \nu \bar{\nu}) < 1.8 \cdot 10^{-5}$  [94], while dashed purple lines show Belle II projected sensitivities [105], if applicable.

The MFV-SMEFT predictions agree with the SM. They peak at slightly smaller values compared to the SM predictions, for which we used as CKM input the SM-only CKM

fit results given in App. B, while for the SMEFT predictions we fit the CKM parameters simultaneously. The uncertainties of the predictions based on our posterior distributions are larger than those of the SM predictions, due to the additional uncertainties introduced by the SMEFT Wilson coefficients.

Predictions for the short-distance contributions to the branching fractions of  $B \rightarrow K^{(*)}\nu\bar{\nu}$  and  $B \rightarrow (\pi, \rho)\nu\bar{\nu}$  are given in Tabs. 21 and 22, respectively, across different lepton-flavor scenarios and  $1\sigma$  uncertainties in parentheses. In charged meson decays  $B^+ \rightarrow M^+\nu\bar{\nu}$ , with  $M$  a pseudoscalar or vector meson, an additional long-distance contribution arises from cascade decays  $B^+ \rightarrow \tau^+(\rightarrow M^+\bar{\nu})\nu$ . For  $b \rightarrow s$  FCNCs, these resonant decays are at the order of 10%, whereas for  $b \rightarrow d$  the  $\tau$ -background is Cabibbo-enhanced and exceeds the SM short-distance contribution in  $B^+ \rightarrow \pi^+\nu\bar{\nu}$  decays by nearly two orders of magnitude [74, 106, 107]. Although clearly important, in our prediction we only give the short-distance contributions as the precise value of the background depends on cuts and experimental aspects. We note that in principle also the  $\tau$ -background could be modified by NP, however, experimental determinations of  $\mathcal{B}(B^+ \rightarrow \tau^+\nu)$  [23] and  $\mathcal{B}(\tau^+ \rightarrow M^+\bar{\nu})$  (see Tab.10) are in good agreement with the SM predictions, thereby limiting possible deviations.

Fit	$\mathcal{B}^0 \rightarrow K^0\nu\bar{\nu}$	$\mathcal{B}(B^0 \rightarrow K^{*0}\nu\bar{\nu})$	$\mathcal{B}(B^+ \rightarrow K^{*+}\nu\bar{\nu})$
$ee$	$4.09(0.44) \cdot 10^{-6}$	$9.07(0.98) \cdot 10^{-6}$	$9.8(1.1) \cdot 10^{-6}$
$\mu\mu$	$4.22(0.44) \cdot 10^{-6}$	$9.36(0.97) \cdot 10^{-6}$	$10.1(1.0) \cdot 10^{-6}$
$\tau\tau$	$4.19(0.71) \cdot 10^{-6}$	$9.3(1.6) \cdot 10^{-6}$	$10.0(1.7) \cdot 10^{-6}$
$e\mu$	$4.19(0.12) \cdot 10^{-6}$	$9.31(0.26) \cdot 10^{-6}$	$10.0(0.3) \cdot 10^{-6}$
$e\tau$	$4.21(0.14) \cdot 10^{-6}$	$9.33(0.31) \cdot 10^{-6}$	$10.1(0.3) \cdot 10^{-6}$
$\mu\tau$	$4.20(0.14) \cdot 10^{-6}$	$9.33(0.30) \cdot 10^{-6}$	$10.1(0.3) \cdot 10^{-6}$
LD	$4.15(0.15) \cdot 10^{-6}$	$9.20(0.33) \cdot 10^{-6}$	$9.93(0.35) \cdot 10^{-6}$

**Table 21.** Predictions for the branching fractions of the short-distance contributions to  $B \rightarrow K^{(*)}\nu\bar{\nu}$  decays in the various lepton-flavor scenarios. The numbers in parentheses indicate the  $1\sigma$  uncertainties.

The mean values of the branching fractions are similar across the different flavor scenarios. However, scenarios involving LFC coefficients tend to exhibit larger uncertainties, since these coefficients interfere with the SM amplitudes, thereby amplifying the parameter-induced spread in the predictions. The largest uncertainties are observed in the  $\tau\tau$  scenario, since the corresponding Wilson coefficients are least constrained.

A distinctive feature of the MFV setup is that FCNC dineutrino decays are maximally correlated, since right-handed currents do not contribute to either the leptonic or quark currents. Consequently, only a single Wilson coefficient,  $\mathcal{C}_{\nu d}^{V,LL}$ , governs these processes. The ratios of branching fractions are therefore independent of SMEFT effects and depend

Fit	$\mathcal{B}(B^0 \rightarrow \pi^0 \nu \bar{\nu})$	$\mathcal{B}(B^+ \rightarrow \pi^+ \nu \bar{\nu})$	$\mathcal{B}(B^0 \rightarrow \rho^0 \nu \bar{\nu})$	$\mathcal{B}(B^+ \rightarrow \rho^+ \nu \bar{\nu})$
$ee$	$5.88(0.78) \cdot 10^{-8}$	$1.27(0.17) \cdot 10^{-7}$	$1.70(0.22) \cdot 10^{-7}$	$3.66(0.49) \cdot 10^{-7}$
$\mu\mu$	$5.59(0.70) \cdot 10^{-8}$	$1.20(0.15) \cdot 10^{-7}$	$1.61(0.20) \cdot 10^{-7}$	$3.48(0.44) \cdot 10^{-7}$
$\tau\tau$	$6.0(1.1) \cdot 10^{-8}$	$1.30(0.24) \cdot 10^{-7}$	$1.74(0.32) \cdot 10^{-7}$	$3.75(0.70) \cdot 10^{-7}$
$e\mu$	$5.90(0.48) \cdot 10^{-8}$	$1.27(0.10) \cdot 10^{-7}$	$1.70(0.14) \cdot 10^{-7}$	$3.68(0.30) \cdot 10^{-7}$
$e\tau$	$6.00(0.50) \cdot 10^{-8}$	$1.29(0.11) \cdot 10^{-7}$	$1.73(0.15) \cdot 10^{-7}$	$3.74(0.31) \cdot 10^{-7}$
$\mu\tau$	$5.93(0.48) \cdot 10^{-8}$	$1.28(0.10) \cdot 10^{-7}$	$1.71(0.14) \cdot 10^{-7}$	$3.70(0.30) \cdot 10^{-7}$
LD	$5.49(0.41) \cdot 10^{-8}$	$1.18(0.09) \cdot 10^{-7}$	$1.58(0.12) \cdot 10^{-7}$	$3.42(0.25) \cdot 10^{-7}$

**Table 22.** Predictions for the branching ratios of the short distance contributions to  $B \rightarrow (\pi, \rho) \nu \bar{\nu}$  decays, see Tab. 21.

solely on form factors, kinematics, and CKM matrix elements within the MFV paradigm:

$$\begin{aligned}
\frac{\mathcal{B}(B^0 \rightarrow K^0 \nu \bar{\nu})}{\mathcal{B}(B^0 \rightarrow K^{*0} \nu \bar{\nu})} &= 0.451(38), & \frac{\mathcal{B}(B^0 \rightarrow \pi^0 \nu \bar{\nu})}{\mathcal{B}(B^0 \rightarrow \rho^0 \nu \bar{\nu})} &= 0.346(85), \\
\frac{\mathcal{B}(B^0 \rightarrow \pi^0 \nu \bar{\nu})}{\mathcal{B}(B^0 \rightarrow K^0 \nu \bar{\nu})} &= 0.335(70) \cdot |V_{td}|^2 / |V_{ts}|^2 = 0.0144(32), & & (6.1) \\
\frac{\mathcal{B}(B^0 \rightarrow \rho^0 \nu \bar{\nu})}{\mathcal{B}(B^0 \rightarrow K^{*0} \nu \bar{\nu})} &= 0.436(68) \cdot |V_{td}|^2 / |V_{ts}|^2 = 0.0187(33).
\end{aligned}$$

Here we used  $|V_{td}|^2 / |V_{ts}|^2 = 0.0428(34)$  obtained from the global  $\tau\tau$  fit as input for the CKM parameters. Ratios involving decays of  $B^+$  mesons need to be amended by  $B^+ \rightarrow \tau^+ (\rightarrow M^+ \bar{\nu}) \nu$  induced contributions. The ratios (6.1) probe the MFV structure in  $b \rightarrow d$  and  $b \rightarrow s$  transitions. Deviations would indicate the breakdown of the SM and MFV, that could arise from right-handed currents [108] or light NP.

## 7 Conclusions

We perform a comprehensive global analysis of processes involving leptons and neutrinos from low and high- $p_T$  in the SMEFT, covering semileptonic and purely leptonic four-fermion operators, electroweak dipoles and leptonic Higgs-current ("penguin") operators. Our main target is the lepton flavor structure and exploring its impact on the fit. Specifically, we analyze the data in three ways, (i) lepton-flavor specifically, that is, with only one pair of lepton flavors switched on at a time, for all LFC and LFV combinations, (ii) assuming lepton universality, and (iii) assuming all couplings in the coefficient matrix to be equal.

We find that the strongest limit on NP in the global fit is on the electroweak dipole operator  $\mathcal{O}_{eB}$  in the flavor democratic LD-fit at  $\sim 1000$  TeV, followed by the tensor  $\mathcal{O}_{lequ}^{(3)}$  in the flavor universal LU-fit at  $\sim 100$  TeV, the four-fermion operator  $\mathcal{O}_{\ell q}^{(3)}$  in the LD-fit and the Higgs-current one  $\mathcal{O}_{\varphi e}$  at  $\sim 30$  TeV. These limits are obtained in fits combining different lepton

flavors, except for the latter, which results from the LFV, flavor-specific  $e\mu$ -fit. The results of the fit are consistent with the SM and MFV. 90 % credible intervals are given in App. D.

We also identify in single-coefficient fits, shown in Figs 7, 8, 11 and 16, the impact of sets of observables. We summarize the results for the LFC, universal case and the LFV, democratic case in Tab. 23, where we give the observables with the strongest limits. Improving precision in these observables, theoretical and experimental, is hence contributing to improvements in the global fit. This invites explorations at a future Tera- $Z$ -factory, such as FCC-ee [109], CEPC [110], a super- $\tau$ -charm factory [111], the HL-LHC and precision study in rare  $B$ -decays, as ongoing at the LHC-experiments and Belle II. However, also other observables, while not performing best in the single-coefficient fits, are key for the global fit by resolving ambiguities and flat directions, or sharpening the flavor picture. Two important examples,  $t\bar{t}$  production with leptons, and  $B$  decays to dineutrinos, are highlighted below. A detailed assessment of the individual benefits of the  $\mathcal{O}(170)$  decay modes included in the global analysis, and their impact considering possible improvements in theory and experimental uncertainties on future SMEFT fits, is beyond the scope of this work.

operator	lepton universality (LFC)	lepton democracy (LFV)
$\mathcal{O}_{\varphi\ell}^{(3)}$	$Z \rightarrow \ell\ell, \ell \rightarrow \ell\nu\bar{\nu}$	$Z \rightarrow \ell\ell, \ell \rightarrow \ell\ell\ell, \tau \rightarrow M\ell$
$\mathcal{O}_{lq}^{(3)}$	$B \rightarrow V\ell\ell, pp \rightarrow \ell\ell$	$B \rightarrow V\ell\ell, pp \rightarrow \ell\ell, \tau \rightarrow V\ell$
$\mathcal{O}_{eW}$	$a_\ell$	$\ell \rightarrow \ell\gamma, \ell \rightarrow \ell\ell\ell$

**Table 23.** Observables with strongest impact in single-coefficient fits in LU and LD flavor scenarios.

As the majority of observables are tied with the complexities of quark flavor we fit SMEFT coefficients simultaneously with the CKM elements and the coefficients in the MFV-ansatz, which we employ for the quarks. We also test the MFV-ansatz including higher order terms in the global fit. While data are consistent with MFV, the higher order MFV structure of the Wilson coefficients, parameterized by  $r_{L,R}$  Eq. (2.5) is not well probed, see Fig. 19. This could be improved by a better sensitivity to rare  $B$ -decays, also in the  $ee$  channels and with other leptons complementing the flagship  $B \rightarrow K^*\mu\mu$  mode. Moreover, the  $t\bar{t}\ell\ell$  vertex is key to improve the sensitivity to the right-handed ratios  $r_R$ , which are currently essentially unconstrained. This could be achieved, for example, by further study of the  $t\bar{t}\ell\ell$  production, ideally in lepton flavor specific ways [11] or future measurements of  $t\bar{t}$  production at a lepton collider. More generally, recall that NP signatures in top or charm FCNCs indicate BSM physics beyond MFV.

Within MFV the scalar and tensor operators  $\mathcal{O}_{lequ}^{(1)}$  and  $\mathcal{O}_{lequ}^{(3)}$  are directly probed only in  $t\bar{t}\ell\ell$  production. While the top sector alone is not causing the strong limits displayed in Fig. 18, it provides an independent, complementary constraint in parameter space to the indirect ones from the AMMs, and resolves ambiguities. This underlines the importance of further experimental study, also in other channels than  $ee$  and  $\mu\mu$ .

We also obtain predictions for rare  $B$ -decays into dineutrinos from the fit-posterior, see Sec. 6. Branching ratios are given in Tabs. 21 and 22. We highlight the predictive power of MFV for  $b \rightarrow (d, s)\nu\bar{\nu}$  transitions for the ratios of branching fractions (6.1). If these ratios deviate significantly from the SM predictions, it would indicate the presence of NP that is not captured by the MFV or SMEFT framework, such as sizeable right-handed FCNCs or new light degrees of freedom. Such possibilities together with lepton-nonuniversality are also suggested by the enhanced  $B^+ \rightarrow K^+\nu\bar{\nu}$  branching ratio [112]. Therefore further study of dineutrino modes is strongly encouraged.

Our explorative works contributes to the advancement of flavorful SMEFT fits. We look forward to pursue flavorful global fits with future data.

**Note added:** During the completion of this work, the preprints 2507.06191 [113] and 2507.13141 [114] appeared on the arXiv, which also consider multi-observable SMEFT fits but differ in the following from our works: The former [113] focusses on  $U(3)^5$  and  $U(2)^5$  flavor symmetry, hence does not fit lepton-flavor specifically; the latter [114] analyses LFV four-fermion operators outside of MFV, also presenting only single-coefficient fit results.

## Acknowledgments

LN is supported by the doctoral scholarship program of the *Studienstiftung des Deutschen Volkes*.

## A Numerical Input Parameters

$G_F$  and  $v$  are expressed in terms of the input parameters  $\{\alpha_{\text{em}}, m_W, m_Z\}$  as

$$G_F = \frac{\pi\alpha_{\text{em}}m_Z^2}{\sqrt{2}m_W^2(m_Z^2 - m_W^2)}(1 + \delta_R), \quad (\text{A.1})$$

where  $\delta_R = 0.03686(21)$  [23] and  $v = (\sqrt{2}G_F)^{-1/2}$ . The weak mixing angle  $\theta_W$  is given as

$$\sin^2 \theta_W = 1 - \frac{m_W^2}{m_Z^2}(1 + \delta \sin^2 \theta_W), \quad (\text{A.2})$$

with  $\delta \sin^2 \theta_W = 0.0349(3)$  [23].

Tab. 24 lists the input parameters used in this analysis, from [23]. The values of the decay constants and form factors are given in Tab. 25 and Tab. 26, respectively.

Decay	Ref.	Decay	Ref.	Decay	Ref.
$D \rightarrow \pi$	[121]	$D \rightarrow \eta$	[66]	$D \rightarrow \eta'$	[122]
$D \rightarrow K$	[103]	$B \rightarrow \pi$	[103]	$B \rightarrow K$	[6]
$B \rightarrow D$	[103]	$B_s \rightarrow K$	[103]	$B_s \rightarrow D_s$	[123]
$D \rightarrow \rho$	[66]	$D \rightarrow \omega$	[66]	$D \rightarrow K^*$	[66]
$D_s \rightarrow \phi$	[66]	$D_s \rightarrow K^*$	[66]	$B \rightarrow \rho$	[124]
$B \rightarrow K^*$	[124]	$B \rightarrow D^*$	[125]	$B_s \rightarrow \phi$	[124]
$B_s \rightarrow K^*$	[124]	$B_s \rightarrow D_s^*$	[103]		

**Table 26.** Form factors for semileptonic decays of mesons throughout this analysis. The form factors are obtained from lattice QCD calculations or light-cone sum rules.

Parameter	Value	Parameter	Value
$\alpha_{\text{em}}$	0.0072973525693(11)	$\alpha_s(m_Z)$	0.1180 (9)
$m_W$	80.369(13) GeV	$m_Z$	91.1880(20) GeV
$m_e$	510.99895000(15) keV	$m_\mu$	105.6583755(23) MeV
$m_\tau$	1.77693(9) GeV	$m_b$	4.183(7) GeV
$m_t$	72.57(29) GeV		

**Table 24.** Input parameters used throughout this analysis, taken from [23].

$f_M$	Value	$f_M$	Value
$f_\pi$	130.2(0.8) MeV [103]	$f_\eta^q$	108(3) MeV [115]
$f_\eta^s$	-111(6) MeV [115]	$f_{\eta'}^q$	89(3) MeV [115]
$f_{\eta'}^s$	136(6) MeV [115]	$f_{\rho/\omega}$	199(4) MeV [116]
$f_\phi$	241(9) MeV [117]	$f_K$	155.7(0.3) MeV [103]
$f_{K^*}$	241 MeV [118]	$f_{J/\Psi}$	418(9) MeV [119]
$f_D$	210.4(1.5) MeV [103]	$f_{D_s}$	247.7(1.2) MeV [103]
$f_\Upsilon$	677.2(9.7) MeV [120]	$f_B$	190.0(1.3) MeV [103]
$f_{B_s}$	230.3(1.3) MeV [103]		

**Table 25.** Decay constants of the mesons used in this analysis.

## B Treatment of the CKM matrix

We parameterize the CKM matrix in terms of the Wolfenstein parameters  $\lambda$ ,  $A$ ,  $\rho$  and  $\eta$

$$V_{\text{CKM}} = \begin{pmatrix} 1 - \frac{\lambda^2}{2} - \frac{\lambda^4}{8} & \lambda & A\lambda^3 \left(1 + \frac{\lambda^2}{2}\right) (\rho - i\eta) \\ -\lambda + A^2\lambda^5 \left(\frac{1}{2} - \rho - i\eta\right) & 1 - \frac{\lambda^2}{2} - \frac{\lambda^4}{8} (1 + 4A^2) & A\lambda^2 \\ A\lambda^3 (1 - \rho - i\eta) & -A\lambda^2 + A\lambda^4 \left(\frac{1}{2} - \rho - i\eta\right) & 1 - \frac{\lambda^4}{2} A^2 \end{pmatrix}. \quad (\text{B.1})$$

In the global fit, we treat the CKM parameters as nuisance parameters.

For the MFV expansion in terms of the quark yukawas which involve CKM elements in the mass basis, we employ fixed (central) values for the CKM matrix elements, which we obtain from a fit of  $\Gamma(K \rightarrow \mu\nu_\mu)/\Gamma(\pi \rightarrow \mu\nu_\mu)$ ,  $\Gamma(B \rightarrow \tau\nu_\tau)$ ,  $\Delta M_d$ ,  $\Delta M_s$  [16], neglecting BSM effects. Tab. 27 lists the observables, experimental inputs and SM predictions. We obtain

$$\{\lambda, A, \rho, \eta\} = \{0.22532(47), 0.804(17), 0.184(32), 0.388(52)\}, \quad (\text{B.2})$$

corresponding to the absolute values of the CKM matrix elements

$$V_{\text{CKM}} = \begin{pmatrix} 0.97429(11) & 0.22532(47) & 0.00405(49) \\ 0.22520(47) & 0.97346(11) & 0.04081(85) \\ 0.00832(21) & 0.04016(87) & 0.999167(35) \end{pmatrix}. \quad (\text{B.3})$$

We use these results from "SM-only CKM fit" to compute the SM predictions of various observables, such as those in Tab.20.

Observable	Measurement	SM Prediction
$\mathcal{B}(B^+ \rightarrow \tau^+ \bar{\nu}_\tau)$	$1.09(24) \cdot 10^{-4}$ [23]	$6.361(89) \cdot  V_{ub} ^2$
$\Gamma(K^+ \rightarrow \mu^+ \nu_\mu)/\Gamma(\pi^+ \rightarrow \mu^+ \nu_\mu)$	$1.3367(32)$ [23]	$24.993(90) \cdot  V_{us} ^2 /  V_{ud} ^2$
$\Delta M_d$	$0.5069(19) \cdot 10^{12} \text{ s}^{-1}$ [23]	$4.81(25) \cdot 10^{15} \cdot  V_{td} V_{tb}^* ^2 \text{ s}^{-1}$
$\Delta M_s$	$17.765(5) \cdot 10^{12} \text{ s}^{-1}$ [23]	$7.23(32) \cdot 10^{15} \cdot  V_{ts} V_{tb}^* ^2 \text{ s}^{-1}$

**Table 27.** Observables used to determine the CKM parameters in the SM-only CKM fit. The SM predictions are computed following Ref. [16].

## C Matching Conditions

We match the SMEFT coefficients of the operators in Tab. 1 to the LEFT coefficients at the scale  $\mu = m_W$  at tree-level using [19]. The matching conditions for the dipole operators are given in Eq. (4.2).

For the four-fermion operators, the matching for the purely left-handed operators reads

$$\begin{aligned} \mathcal{C}_{ijkl}^{V,ee,LL} = & \frac{1}{v^2} \left( \tilde{C}_{ijkl}^{ll} - \frac{1}{4} \left( \left( \delta_{ij}(2\sin^2\theta_W - 1) - \tilde{C}_{ij}^{\varphi l+} \right) \left( \delta_{kl}(2\sin^2\theta_W - 1) - \tilde{C}_{kl}^{\varphi l+} \right) \right. \right. \\ & \left. \left. + \left( \delta_{il}(2\sin^2\theta_W - 1) - \tilde{C}_{il}^{\varphi l+} \right) \left( \delta_{kj}(2\sin^2\theta_W - 1) - \tilde{C}_{kj}^{\varphi l+} \right) \right) \right), \end{aligned} \quad (\text{C.1})$$

$$\begin{aligned} \mathcal{C}_{ijkl}^{V,\nu e,LL} = & \frac{1}{v^2} \left( \left( \tilde{C}_{ijkl}^{ll} + \tilde{C}_{kl ij}^{ll} \right) - \left( \left( \delta_{ij} - \tilde{C}_{ij}^{\varphi l-} \right) \left( \delta_{kl}(2\sin^2\theta_W - 1) - \tilde{C}_{kl}^{\varphi l+} \right) \right. \right. \\ & \left. \left. - 2 \left( \delta_{il} + \tilde{C}_{il}^{(3)} \right) \left( \delta_{kj} + \tilde{C}_{kj}^{\varphi l(3)} \right) \right) \right), \end{aligned} \quad (\text{C.2})$$

$$\mathcal{C}_{ijkl}^{V,\nu u,LL} = \frac{1}{v^2} \left( \tilde{C}_{ijkl}^{lq+} - \left( \delta_{ij} - \tilde{C}_{ij}^{\varphi l-} \right) \left( \delta_{kl} \left( 1 - \frac{4}{3} \sin^2\theta_W \right) \right) \right), \quad (\text{C.3})$$

$$\mathcal{C}_{ijkl}^{V,\nu d,LL} = \frac{1}{v^2} \left( \tilde{C}_{ijkl}^{lq-} - \left( \delta_{ij} - \tilde{C}_{ij}^{\varphi l-} \right) \left( \delta_{kl} \left( -1 + \frac{2}{3} \sin^2\theta_W \right) \right) \right), \quad (\text{C.4})$$

$$\mathcal{C}_{ijkl}^{V,eu,LL} = \frac{1}{v^2} \left( \tilde{C}_{ijkl}^{lq-} - \left( \delta_{ij}(2\sin^2\theta_W - 1) - \tilde{C}_{ij}^{\varphi l+} \right) \left( \delta_{kl} \left( 1 - \frac{4}{3} \sin^2\theta_W \right) \right) \right), \quad (\text{C.5})$$

$$\mathcal{C}_{ijkl}^{V,ed,LL} = \frac{1}{v^2} \left( \tilde{C}_{ijkl}^{lq+} - \left( \delta_{ij}(2\sin^2\theta_W - 1) - \tilde{C}_{ij}^{\varphi l+} \right) \left( \delta_{kl} \left( -1 + \frac{2}{3} \sin^2\theta_W \right) \right) \right), \quad (\text{C.6})$$

$$\mathcal{C}_{ijkl}^{V,\nu edu} + \text{h.c.} = \frac{2}{v^2} \left( \tilde{C}_{ijkl}^{lq(3)} - \left( \delta_{ij} + \tilde{C}_{ij}^{\varphi l(3)} \right) V_{lk} \right). \quad (\text{C.7})$$

For the purely right-handed operators, the matching conditions are given by

$$\begin{aligned} \mathcal{C}_{ijkl}^{V,ee,RR} = & \frac{1}{v^2} \left( \tilde{C}_{ijkl}^{ee} - \frac{1}{4} \left( \left( \delta_{ij} 2\sin^2\theta_W - \tilde{C}_{ij}^{\varphi e} \right) \left( \delta_{kl} 2\sin^2\theta_W - \tilde{C}_{kl}^{\varphi e} \right) \right. \right. \\ & \left. \left. + \left( \delta_{il} 2\sin^2\theta_W - \tilde{C}_{il}^{\varphi e} \right) \left( \delta_{kj} 2\sin^2\theta_W - \tilde{C}_{kj}^{\varphi e} \right) \right) \right), \end{aligned} \quad (\text{C.8})$$

$$\mathcal{C}_{ijkl}^{V,eu,RR} = \frac{1}{v^2} \left( \tilde{C}_{ijkl}^{eu} - \left( \delta_{ij} 2\sin^2\theta_W - \tilde{C}_{ij}^{\varphi e} \right) \left( -\delta_{kl} \frac{4}{3} \sin^2\theta_W \right) \right), \quad (\text{C.9})$$

$$\mathcal{C}_{ijkl}^{V,ed,RR} = \frac{1}{v^2} \left( \tilde{C}_{ijkl}^{ed} - \left( \delta_{ij} 2\sin^2\theta_W - \tilde{C}_{ij}^{\varphi e} \right) \left( \delta_{kl} \frac{2}{3} \sin^2\theta_W \right) \right), \quad (\text{C.10})$$

$$(\text{C.11})$$

and for the mixed chirality operators,

$$\mathcal{C}_{ijkl}^{V,ee,LR} = \frac{1}{v^2} \left( \tilde{C}_{ijkl}^{le} - \left( \delta_{ij}(2\sin^2\theta_W - 1) - \tilde{C}_{ij}^{\varphi l+} \right) \left( \delta_{kl} 2\sin^2\theta_W - \tilde{C}_{kl}^{\varphi e} \right) \right), \quad (\text{C.12})$$

$$\mathcal{C}_{ijkl}^{V,\nu e,LR} = \frac{1}{v^2} \left( \tilde{C}_{ijkl}^{le} - \left( \delta_{ij} - \tilde{C}_{ij}^{\varphi l-} \right) \left( \delta_{kl} 2\sin^2\theta_W - \tilde{C}_{kl}^{\varphi e} \right) \right), \quad (\text{C.13})$$

$$\mathcal{C}_{ijkl}^{V,LR} = \frac{1}{v^2} \left( \tilde{C}_{ijkl}^{lu} - (\delta_{ij} - \tilde{C}_{ij}^{\varphi l}) \left( -\delta_{kl} \frac{4}{3} \sin^2 \theta_W \right) \right), \quad (\text{C.14})$$

$$\mathcal{C}_{ijkl}^{V,LR} = \frac{1}{v^2} \left( \tilde{C}_{ijkl}^{ld} - (\delta_{ij} - \tilde{C}_{ij}^{\varphi l}) \left( \delta_{kl} \frac{2}{3} \sin^2 \theta_W \right) \right), \quad (\text{C.15})$$

$$\mathcal{C}_{ijkl}^{V,LR} = \frac{1}{v^2} \left( \tilde{C}_{ijkl}^{lu} - (\delta_{ij}(2 \sin^2 \theta_W - 1) - \tilde{C}_{ij}^{\varphi l+}) \left( -\delta_{kl} \frac{4}{3} \sin^2 \theta_W \right) \right), \quad (\text{C.16})$$

$$\mathcal{C}_{ijkl}^{V,LR} = \frac{1}{v^2} \left( \tilde{C}_{ijkl}^{ld} - (\delta_{ij}(2 \sin^2 \theta_W - 1) - \tilde{C}_{ij}^{\varphi l+}) \left( \delta_{kl} \frac{2}{3} \sin^2 \theta_W \right) \right), \quad (\text{C.17})$$

$$\mathcal{C}_{ijkl}^{V,LR} = \frac{1}{v^2} \left( \tilde{C}_{ijkl}^{qe} - (\delta_{ij}(1 - \frac{4}{3} \sin^2 \theta_W)) \left( \delta_{kl} 2 \sin^2 \theta_W - \tilde{C}_{kl}^{\varphi e} \right) \right), \quad (\text{C.18})$$

$$\mathcal{C}_{ijkl}^{V,LR} = \frac{1}{v^2} \left( \tilde{C}_{ijkl}^{qe} - (\delta_{ij}(-1 + \frac{2}{3} \sin^2 \theta_W)) \left( \delta_{kl} 2 \sin^2 \theta_W - \tilde{C}_{kl}^{\varphi e} \right) \right). \quad (\text{C.19})$$

## D Credible intervals of the global fit

We show the 90% credible intervals for the SMEFT coefficients for the global fit in Tabs. 28-33 for the different operator classes.

Lepton	$\tilde{C}_{\varphi l}^{(1)}$	$\tilde{C}_{\varphi l}^{(3)}$	$\tilde{C}_{\varphi e}$
$ee$	$[-0.59, 5.52] \cdot 10^{-3}$	$[-2.18, 0.70] \cdot 10^{-3}$	$[-2.59, 5.83] \cdot 10^{-3}$
$\mu\mu$	$[-3.83, 9.65] \cdot 10^{-3}$	$[-0.80, 2.18] \cdot 10^{-3}$	$[-4.88, 9.06] \cdot 10^{-3}$
$\tau\tau$	$[-0.73, 1.83] \cdot 10^{-2}$	$[-1.49, 3.22] \cdot 10^{-3}$	$[-2.83, 0.85] \cdot 10^{-2}$
$e\mu$	$[-2.11, 3.95] \cdot 10^{-3}$	$[-3.69, 2.03] \cdot 10^{-3}$	$[-4.83, 4.32] \cdot 10^{-5}$
$e\tau$	$[-3.07, 2.39] \cdot 10^{-2}$	$[-2.21, 2.90] \cdot 10^{-2}$	$[-8.54, 8.51] \cdot 10^{-4}$
$\mu\tau$	$[-2.50, 3.67] \cdot 10^{-2}$	$[-3.40, 2.38] \cdot 10^{-2}$	$[-7.49, 7.51] \cdot 10^{-4}$
LU	$[0.21, 3.08] \cdot 10^{-3}$	$[-1.82, 1.07] \cdot 10^{-3}$	$[-1.20, 3.80] \cdot 10^{-3}$
LD	$[-5.43, 5.96] \cdot 10^{-4}$	$[-4.99, 5.41] \cdot 10^{-4}$	$[-1.96, 1.32] \cdot 10^{-4}$

**Table 28.** 90% credible intervals for the leptonic Higgs-current coefficients.

Lepton	$\tilde{C}_{lq}^{(1)}$	$\tilde{C}_{lq}^{(3)}$	$\tilde{C}_{qe}$
$ee$	$[-0.95, 1.10] \cdot 10^{-3}$	$[-0.32, 1.26] \cdot 10^{-3}$	$[-6.17, 9.79] \cdot 10^{-4}$
$\mu\mu$	$[-0.46, 1.64] \cdot 10^{-3}$	$[-1.02, 0.88] \cdot 10^{-3}$	$[-2.04, 0.54] \cdot 10^{-3}$
$\tau\tau$	$[-4.33, 3.35] \cdot 10^{-3}$	$[-1.24, 2.43] \cdot 10^{-3}$	$[-9.94, 1.46] \cdot 10^{-3}$
$e\mu$	$[-2.80, 3.15] \cdot 10^{-4}$	$[-0.01, 3.19] \cdot 10^{-4}$	$[-1.72, 1.13] \cdot 10^{-4}$
$e\tau$	$[-3.43, 3.84] \cdot 10^{-4}$	$[-0.27, 4.49] \cdot 10^{-4}$	$[-3.70, 3.69] \cdot 10^{-4}$
$\mu\tau$	$[-3.12, 3.56] \cdot 10^{-4}$	$[0.78, 5.74] \cdot 10^{-4}$	$[-3.23, 3.23] \cdot 10^{-4}$
LU	$[-4.72, 9.14] \cdot 10^{-4}$	$[-2.85, 1.32] \cdot 10^{-4}$	$[-3.07, 6.81] \cdot 10^{-4}$
LD	$[-1.77, 1.78] \cdot 10^{-4}$	$[-0.86, 5.91] \cdot 10^{-5}$	$[-0.87, 1.10] \cdot 10^{-4}$

**Table 29.** 90% credible intervals for the semileptonic four-fermion coefficients with left-handed quarks.

Lepton	$\tilde{C}_{lu}$	$\tilde{C}_{ld}$	$\tilde{C}_{eu}$	$\tilde{C}_{ed}$
$ee$	$[-2.38, 1.72] \cdot 10^{-3}$	$[-2.22, 2.54] \cdot 10^{-3}$	$[-1.67, 3.90] \cdot 10^{-3}$	$[-3.18, 2.00] \cdot 10^{-3}$
$\mu\mu$	$[-2.77, 5.82] \cdot 10^{-3}$	$[-3.27, 1.77] \cdot 10^{-3}$	$[-8.17, 3.24] \cdot 10^{-3}$	$[-2.12, 4.21] \cdot 10^{-3}$
$\tau\tau$	$[-1.75, 1.24] \cdot 10^{-2}$	$[-6.79, 9.17] \cdot 10^{-3}$	$[-3.85, 0.42] \cdot 10^{-2}$	$[-0.27, 1.98] \cdot 10^{-2}$
$e\mu$	$[-4.98, 4.88] \cdot 10^{-4}$	$[-5.50, 5.57] \cdot 10^{-4}$	$[-2.63, 2.68] \cdot 10^{-4}$	$[-4.78, 4.75] \cdot 10^{-4}$
$e\tau$	$[-5.56, 6.60] \cdot 10^{-4}$	$[-4.90, 4.07] \cdot 10^{-4}$	$[-5.52, 5.51] \cdot 10^{-4}$	$[-4.48, 4.47] \cdot 10^{-4}$
$\mu\tau$	$[-4.94, 6.30] \cdot 10^{-4}$	$[-4.74, 3.59] \cdot 10^{-4}$	$[-5.12, 5.09] \cdot 10^{-4}$	$[-4.12, 4.15] \cdot 10^{-4}$
LU	$[-0.69, 1.86] \cdot 10^{-3}$	$[-1.99, 1.24] \cdot 10^{-3}$	$[0.12, 2.44] \cdot 10^{-3}$	$[-2.39, 0.80] \cdot 10^{-3}$
LD	$[-2.87, 3.69] \cdot 10^{-4}$	$[-2.51, 2.50] \cdot 10^{-4}$	$[-2.66, 2.74] \cdot 10^{-4}$	$[-2.39, 2.19] \cdot 10^{-4}$

**Table 30.** 90% credible intervals for the semileptonic four-fermion coefficients with right-handed quarks.

Lepton	$\tilde{C}_{ll}$	$\tilde{C}_{ee}$	$\tilde{C}_{le}$
$ee$	$[-0.01, 0.19]$	$[-0.21, 0.14]$	$[-0.24, 0.08]$
$\mu\mu$	$[-0.13, 0.11]$	$[-0.25, 0.88]$	$[-1.39, 0.91]$
$\tau\tau$	$[-0.04, 0.41]$	$[-0.89, 3.51]$	$[-3.62, 4.60]$
$e\mu$	$[-0.28, 0.29]$		$[-0.49, 0.56]$
$e\tau$	$[-0.39, 0.39]$		$[-0.70, 0.75]$
$\mu\tau$	$[-0.38, 0.35]$		$[-0.62, 0.72]$
LU	$[-4.84, 1.49] \cdot 10^{-3}$	$[-4.37, 0.98] \cdot 10^{-2}$	$[-2.55, 0.42] \cdot 10^{-2}$
LD	$[-4.21, 6.14] \cdot 10^{-5}$	$[-4.34, 2.87] \cdot 10^{-5}$	$[-9.08, 6.10] \cdot 10^{-5}$

**Table 31.** 90% credible intervals for the four-lepton coefficients.

Lepton	$\tilde{C}_{eB}$	$\tilde{C}_{eW}$
$ee$	$[-3.49, 3.55] \cdot 10^{-3}$	$[-2.44, 2.46] \cdot 10^{-2}$
$\mu\mu$	$[-4.12, 4.21] \cdot 10^{-3}$	$[-2.94, 2.87] \cdot 10^{-2}$
$\tau\tau$	$[-1.06, 1.04]$	$[-0.25, 0.24]$
$e\mu$	$[-0.38, 0.38]$	$[-0.11, 0.11]$
$\mu e$	$[-0.37, 0.37]$	$[-0.11, 0.11]$
$e\tau$	$[-0.53, 0.52]$	$[-0.15, 0.16]$
$\tau e$	$[-0.52, 0.52]$	$[-0.15, 0.15]$
$\mu\tau$	$[-0.43, 0.42]$	$[-0.12, 0.13]$
$\tau\mu$	$[-0.47, 0.47]$	$[-0.14, 0.14]$
LU	$[-5.47, 5.46] \cdot 10^{-5}$	$[-2.29, 1.99] \cdot 10^{-2}$
LD	$[-5.95, 0.11] \cdot 10^{-8}$	$[-1.73, 1.71] \cdot 10^{-4}$

**Table 32.** 90% credible intervals for the leptonic dipole coefficients.

Lepton	$\tilde{C}_{lequ}^{(1)}$	$\tilde{C}_{lequ}^{(3)}$
$ee$	$[-0.14, 0.15]$	$[-2.68, 2.63] \cdot 10^{-2}$
$\mu\mu$	$[-0.22, 0.20]$	$[-3.11, 3.18] \cdot 10^{-2}$
$\tau\tau$	$[-121, 130]$	$[-8.16, 7.98]$
$e\mu$	$[-190, 190]$	$[-3.20, 3.24]$
$\mu e$	$[-186, 187]$	$[-3.10, 3.08]$
$e\tau$	$[-49.8, 57.4]$	$[-4.04, 3.91]$
$\tau e$	$[-50.7, 50.7]$	$[-3.82, 3.84]$
$\mu\tau$	$[-31.8, 61.7]$	$[-3.32, 3.10]$
$\tau\mu$	$[-46.6, 46.9]$	$[-3.48, 3.50]$
LU	$[-0.10, 0.10]$	$[-1.76, 0.50] \cdot 10^{-6}$
LD	$[-5.89, 6.17] \cdot 10^{-3}$	$[-2.49, 2.34] \cdot 10^{-5}$

**Table 33.** 90% credible intervals for the scalar and tensor coefficients.

## E Further predictions for $B \rightarrow (K, K^*, \pi, \rho)\nu\bar{\nu}$

In Fig. 23 we show  $\mathcal{B}(B^0 \rightarrow K^0\nu\bar{\nu})$  (top) and  $\mathcal{B}(B^0 \rightarrow \pi^0\nu\bar{\nu})$  (bottom) based on the posterior probability distribution of the global fit in the  $\tau\tau$  scenario. Fig. 24 shows the predictions for the short distance contributions to the dineutrino decay rates of charged  $B$  mesons. For the latter, resonant-contributions from the  $\tau$  [106] are not included here.

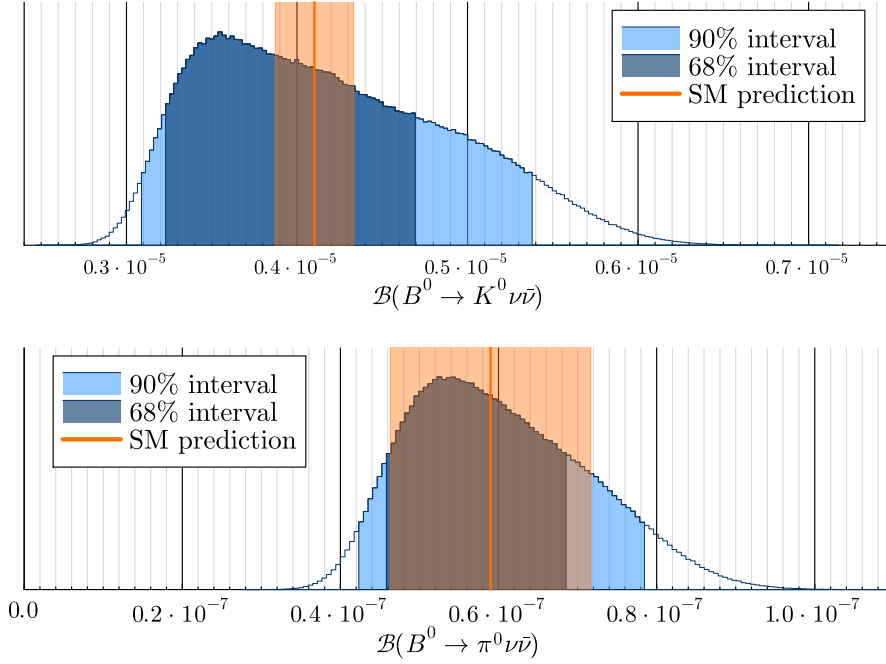


**Figure 23.** Predictions for  $B^0 \rightarrow K^0\nu\bar{\nu}$  (top) and  $B^0 \rightarrow \pi^0\nu\bar{\nu}$  (bottom) based on the global fit in the  $\tau\tau$  scenario. Colored bands indicate the 68% and 90% credible intervals; the orange band denotes the  $1\sigma$  SM prediction.

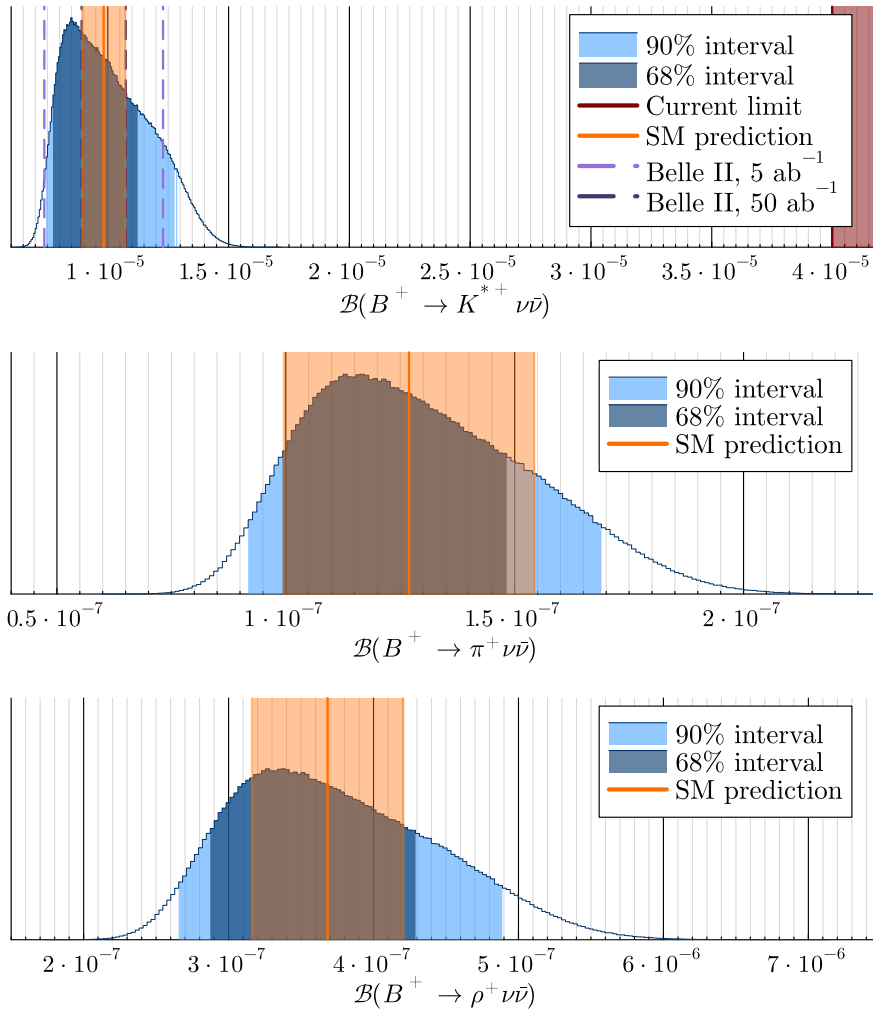


**Figure 24.** Predictions for the short-distance contributions to the branching ratios of  $B^+ \rightarrow K^{*+} \nu \bar{\nu}$  (top),  $B^+ \rightarrow \pi^+ \nu \bar{\nu}$  (middle) and  $B^+ \rightarrow \rho^+ \nu \bar{\nu}$  (bottom) based on the global fit in the  $\tau\tau$  scenario. Blue-colored bands indicate the 68% (light) and 90% (dark) credible intervals; the orange band denotes the  $1\sigma$  SM prediction. The red area represents the current 90% CL bound  $\mathcal{B}(B^+ \rightarrow K^{*+} \nu \bar{\nu}) < 4.0 \cdot 10^{-5}$  [104], while dashed purple lines show Belle II projected sensitivities [105], if applicable.

## References

- [1] W. Buchmuller and D. Wyler, *Effective Lagrangian Analysis of New Interactions and Flavor Conservation*, *Nucl. Phys. B* **268** (1986) 621–653.
- [2] B. Grzadkowski, M. Iskrzynski, M. Misiak and J. Rosiek, *Dimension-Six Terms in the Standard Model Lagrangian*, *JHEP* **10** (2010) 085, [[1008.4884](#)].
- [3] R. Aoude, T. Hurth, S. Renner and W. Shepherd, *The impact of flavour data on global fits of the MFV SMEFT*, *JHEP* **12** (2020) 113, [[2003.05432](#)].
- [4] S. Bruggisser, R. Schäfer, D. van Dyk and S. Westhoff, *The Flavor of UV Physics*, *JHEP* **05** (2021) 257, [[2101.07273](#)].
- [5] A. Greljo, J. Salko, A. Smolkovič and P. Stangl, *Rare  $b$  decays meet high-mass Drell-Yan*, *JHEP* **05** (2023) 087, [[2212.10497](#)].
- [6] C. Grunwald, G. Hiller, K. Kröninger and L. Nollen, *More synergies from beauty, top, Z and Drell-Yan measurements in SMEFT*, *JHEP* **11** (2023) 110, [[2304.12837](#)].
- [7] L. Allwicher, D. A. Faroughy, F. Jaffredo, O. Sumensari and F. Wilsch, *Drell-Yan tails beyond the Standard Model*, *JHEP* **03** (2023) 064, [[2207.10714](#)].
- [8] G. Hiller, L. Nollen and D. Wendler, *Total Drell-Yan in the flavorful SMEFT*, *Eur. Phys. J. C* **85** (2025) 657, [[2502.12250](#)].
- [9] R. Aliberti et al., *The anomalous magnetic moment of the muon in the Standard Model: an update*, *Phys. Rept.* **1143** (2025) 1–158, [[2505.21476](#)].
- [10] MUON G-2 collaboration, D. P. Aguillard et al., *Measurement of the Positive Muon Anomalous Magnetic Moment to 127 ppb*, *Phys. Rev. Lett.* **135** (2025) 101802, [[2506.03069](#)].
- [11] ATLAS collaboration, G. Aad et al., *Measurement of high-mass  $t\bar{t}\ell^+\ell^-$  production and lepton flavour universality-inspired effective field theory interpretations at  $\sqrt{s} = 13$  TeV with the ATLAS detector*, [2504.05919](#).
- [12] E. E. Jenkins, A. V. Manohar and M. Trott, *Renormalization Group Evolution of the Standard Model Dimension Six Operators I: Formalism and lambda Dependence*, *JHEP* **10** (2013) 087, [[1308.2627](#)].
- [13] R. Alonso, E. E. Jenkins, A. V. Manohar and M. Trott, *Renormalization Group Evolution of the Standard Model Dimension Six Operators III: Gauge Coupling Dependence and Phenomenology*, *JHEP* **04** (2014) 159, [[1312.2014](#)].
- [14] E. E. Jenkins, A. V. Manohar and M. Trott, *Renormalization Group Evolution of the Standard Model Dimension Six Operators II: Yukawa Dependence*, *JHEP* **01** (2014) 035, [[1310.4838](#)].
- [15] J. Aebischer, J. Kumar and D. M. Straub, *Wilson: a Python package for the running and matching of Wilson coefficients above and below the electroweak scale*, *Eur. Phys. J. C* **78** (2018) 1026, [[1804.05033](#)].
- [16] S. Descotes-Genon, A. Falkowski, M. Fedele, M. González-Alonso and J. Virto, *The CKM parameters in the SMEFT*, *JHEP* **05** (2019) 172, [[1812.08163](#)].
- [17] G. D’Ambrosio, G. F. Giudice, G. Isidori and A. Strumia, *Minimal flavor violation: An Effective field theory approach*, *Nucl. Phys. B* **645** (2002) 155–187, [[hep-ph/0207036](#)].

- [18] A. Greljo, A. Palavrić and A. E. Thomsen, *Adding Flavor to the SMEFT*, *JHEP* **10** (2022) 010, [[2203.09561](#)].
- [19] E. E. Jenkins, A. V. Manohar and P. Stoffer, *Low-Energy Effective Field Theory below the Electroweak Scale: Operators and Matching*, *JHEP* **03** (2018) 016, [[1709.04486](#)].
- [20] E. E. Jenkins, A. V. Manohar and P. Stoffer, *Low-Energy Effective Field Theory below the Electroweak Scale: Anomalous Dimensions*, *JHEP* **01** (2018) 084, [[1711.05270](#)].
- [21] I. Brivio and M. Trott, *The Standard Model as an Effective Field Theory*, *Phys. Rept.* **793** (2019) 1–98, [[1706.08945](#)].
- [22] ALEPH, DELPHI, L3, OPAL, SLD, LEP ELECTROWEAK WORKING GROUP, SLD ELECTROWEAK GROUP, SLD HEAVY FLAVOUR GROUP collaboration, S. Schael et al., *Precision electroweak measurements on the Z resonance*, *Phys. Rept.* **427** (2006) 257–454, [[hep-ex/0509008](#)].
- [23] PARTICLE DATA GROUP collaboration, S. Navas et al., *Review of particle physics*, *Phys. Rev. D* **110** (2024) 030001.
- [24] ATLAS collaboration, G. Aad et al., *Search for the charged-lepton-flavor-violating decay  $Z \rightarrow e\mu$  in  $pp$  collisions at  $\sqrt{s} = 13$  TeV with the ATLAS detector*, *Phys. Rev. D* **108** (2023) 032015, [[2204.10783](#)].
- [25] ATLAS collaboration, G. Aad et al., *Search for lepton-flavor-violation in Z-boson decays with  $\tau$ -leptons with the ATLAS detector*, *Phys. Rev. Lett.* **127** (2022) 271801, [[2105.12491](#)].
- [26] CMS collaboration, A. Tumasyan et al., *Precision measurement of the W boson decay branching fractions in proton-proton collisions at  $\sqrt{s} = 13$  TeV*, *Phys. Rev. D* **105** (2022) 072008, [[2201.07861](#)].
- [27] DELPHI collaboration, J. Abdallah et al., *Measurement and interpretation of fermion-pair production at LEP energies above the Z resonance*, *Eur. Phys. J. C* **45** (2006) 589–632, [[hep-ex/0512012](#)].
- [28] W. R. Inc., “Mathematica, Version 14.2.”
- [29] R. Mertig, M. Bohm and A. Denner, *FEYN CALC: Computer algebraic calculation of Feynman amplitudes*, *Comput. Phys. Commun.* **64** (1991) 345–359.
- [30] V. Shtabovenko, R. Mertig and F. Orellana, *New Developments in FeynCalc 9.0*, *Comput. Phys. Commun.* **207** (2016) 432–444, [[1601.01167](#)].
- [31] V. Shtabovenko, R. Mertig and F. Orellana, *FeynCalc 9.3: New features and improvements*, *Comput. Phys. Commun.* **256** (2020) 107478, [[2001.04407](#)].
- [32] V. Shtabovenko, R. Mertig and F. Orellana, *FeynCalc 10: Do multiloop integrals dream of computer codes?*, *Comput. Phys. Commun.* **306** (2025) 109357, [[2312.14089](#)].
- [33] A. Dedes, J. Rosiek, M. Ryczkowski, K. Suxho and L. Trifyllis, *SmeftFR v3 – Feynman rules generator for the Standard Model Effective Field Theory*, *Comput. Phys. Commun.* **294** (2024) 108943, [[2302.01353](#)].
- [34] J. Alwall, R. Frederix, S. Frixione, V. Hirschi, F. Maltoni, O. Mattelaer, H. S. Shao, T. Stelzer, P. Torrielli and M. Zaro, *The automated computation of tree-level and next-to-leading order differential cross sections, and their matching to parton shower simulations*, *JHEP* **07** (2014) 079, [[1405.0301](#)].

- [35] NNPDF collaboration, R. D. Ball et al., *The path to proton structure at 1% accuracy*, *Eur. Phys. J. C* **82** (2022) 428, [[2109.02653](#)].
- [36] J. Cruz-Martinez, S. Forte, N. Laurenti, T. R. Rabemananjara and J. Rojo, *LO, NLO, and NNLO parton distributions for LHC event generators*, *JHEP* **09** (2024) 088, [[2406.12961](#)].
- [37] A. Buckley, J. Ferrando, S. Lloyd, K. Nordström, B. Page, M. Rüfenacht, M. Schönherr and G. Watt, *LHAPDF6: parton density access in the LHC precision era*, *Eur. Phys. J. C* **75** (2015) 132, [[1412.7420](#)].
- [38] C. Bierlich et al., *A comprehensive guide to the physics and usage of PYTHIA 8.3*, *SciPost Phys. Codeb.* **2022** (2022) 8, [[2203.11601](#)].
- [39] DELPHES 3 collaboration, J. de Favereau, C. Delaere, P. Demin, A. Giammanco, V. Lemaitre, A. Mertens and M. Selvaggi, *DELPHES 3, A modular framework for fast simulation of a generic collider experiment*, *JHEP* **02** (2014) 057, [[1307.6346](#)].
- [40] M. Farina, G. Panico, D. Pappadopulo, J. T. Ruderman, R. Torre and A. Wulzer, *Energy helps accuracy: electroweak precision tests at hadron colliders*, *Phys. Lett. B* **772** (2017) 210–215, [[1609.08157](#)].
- [41] CMS collaboration, A. M. Sirunyan et al., *Search for resonant and nonresonant new phenomena in high-mass dilepton final states at  $\sqrt{s} = 13$  TeV*, *JHEP* **07** (2021) 208, [[2103.02708](#)].
- [42] ATLAS collaboration, G. Aad et al., *Search for lepton-flavour violation in high-mass dilepton final states using  $139 \text{ fb}^{-1}$  of  $pp$  collisions at  $\sqrt{s} = 13$  TeV with the ATLAS detector*, *JHEP* **23** (2020) 082, [[2307.08567](#)].
- [43] ATLAS collaboration, G. Aad et al., *Search for a heavy charged boson in events with a charged lepton and missing transverse momentum from  $pp$  collisions at  $\sqrt{s} = 13$  TeV with the ATLAS detector*, *Phys. Rev. D* **100** (2019) 052013, [[1906.05609](#)].
- [44] CMS collaboration, A. Tumasyan et al., *Search for new physics in the  $\tau$  lepton plus missing transverse momentum final state in proton-proton collisions at  $\sqrt{s} = 13$  TeV*, *JHEP* **09** (2023) 051, [[2212.12604](#)].
- [45] J. Aebischer, W. Dekens, E. E. Jenkins, A. V. Manohar, D. Sengupta and P. Stoffer, *Effective field theory interpretation of lepton magnetic and electric dipole moments*, *JHEP* **07** (2021) 107, [[2102.08954](#)].
- [46] T. Aoyama, T. Kinoshita and M. Nio, *Theory of the Anomalous Magnetic Moment of the Electron*, *Atoms* **7** (2019) 28.
- [47] ATLAS collaboration, G. Aad et al., *Observation of the  $\gamma\gamma \rightarrow \tau\tau$  Process in  $Pb+Pb$  Collisions and Constraints on the  $\tau$ -Lepton Anomalous Magnetic Moment with the ATLAS Detector*, *Phys. Rev. Lett.* **131** (2023) 151802, [[2204.13478](#)].
- [48] S. Eidelman and M. Passera, *Theory of the tau lepton anomalous magnetic moment*, *Mod. Phys. Lett. A* **22** (2007) 159–179, [[hep-ph/0701260](#)].
- [49] MEG collaboration, A. M. Baldini et al., *Search for the lepton flavour violating decay  $\mu^+ \rightarrow e^+\gamma$  with the full dataset of the MEG experiment*, *Eur. Phys. J. C* **76** (2016) 434, [[1605.05081](#)].
- [50] BABAR collaboration, B. Aubert et al., *Searches for Lepton Flavor Violation in the Decays  $\tau_{u+} \rightarrow e_{u+}$  gamma and  $\tau_{u-} \rightarrow \mu_{u-}$  gamma*, *Phys. Rev. Lett.* **104** (2010) 021802, [[0908.2381](#)].

- [51] BELLE collaboration, A. Abdesselam et al., *Search for lepton-flavor-violating tau-lepton decays to  $\ell\gamma$  at Belle*, *JHEP* **10** (2021) 19, [[2103.12994](#)].
- [52] A. Crivellin, S. Najjari and J. Rosiek, *Lepton Flavor Violation in the Standard Model with general Dimension-Six Operators*, *JHEP* **04** (2014) 167, [[1312.0634](#)].
- [53] M. I. Ali, U. Chattopadhyay, N. Rajeev and J. Roy, *SMEFT analysis of charged lepton flavor violating B-meson decays*, *Phys. Rev. D* **109** (2024) 075028, [[2312.05071](#)].
- [54] I. Plakias and O. Sumensari, *Lepton Flavor Violation in Semileptonic Observables*, [2312.14070](#).
- [55] K. Hayasaka et al., *Search for Lepton Flavor Violating Tau Decays into Three Leptons with 719 Million Produced Tau+Tau- Pairs*, *Phys. Lett. B* **687** (2010) 139–143, [[1001.3221](#)].
- [56] SINDRUM collaboration, U. Bellgardt et al., *Search for the Decay  $\mu^+ \rightarrow e^+e^+e^-$* , *Nucl. Phys. B* **299** (1988) 1–6.
- [57] J. Erler, *Electroweak radiative corrections to semileptonic tau decays*, *Rev. Mex. Fis.* **50** (2004) 200–202, [[hep-ph/0211345](#)].
- [58] M. A. Arroyo-Ureña, G. Hernández-Tomé, G. López-Castro, P. Roig and I. Rosell, *Radiative corrections to  $\tau \rightarrow \pi(K)\nu\tau[\gamma]$ : A reliable new physics test*, *Phys. Rev. D* **104** (2021) L091502, [[2107.04603](#)].
- [59] HEAVY FLAVOR AVERAGING GROUP (HFLAV) collaboration, S. Banerjee et al., *Averages of b-hadron, c-hadron, and  $\tau$ -lepton properties as of 2023*, [2411.18639](#).
- [60] A. Angelescu, D. A. Faroughy and O. Sumensari, *Lepton Flavor Violation and Dilepton Tails at the LHC*, *Eur. Phys. J. C* **80** (2020) 641, [[2002.05684](#)].
- [61] BELLE collaboration, Y. Miyazaki et al., *Search for lepton flavor violating tau- decays into l- eta, l- eta-prime and l- pi0*, *Phys. Lett. B* **648** (2007) 341–350, [[hep-ex/0703009](#)].
- [62] BABAR collaboration, B. Aubert et al., *Search for Lepton Flavor Violating Decays  $\tau^\pm \rightarrow \ell^\pm\pi^0, \ell^\pm\eta, \ell^\pm\eta'$* , *Phys. Rev. Lett.* **98** (2007) 061803, [[hep-ex/0610067](#)].
- [63] BELLE collaboration, N. Tsuzuki et al., *Search for lepton-flavor-violating  $\tau$  decays into a lepton and a vector meson using the full Belle data sample*, *JHEP* **06** (2023) 118, [[2301.03768](#)].
- [64] T. Li, X.-D. Ma and M. A. Schmidt, *General neutrino interactions with sterile neutrinos in light of coherent neutrino-nucleus scattering and meson invisible decays*, *JHEP* **07** (2020) 152, [[2005.01543](#)].
- [65] J. G. Korner, K. Schilcher, M. Wirbel and Y. L. Wu, *A Detailed Analysis of D, D(s) and B Meson Transition Form-factors and the Determination of V(cb)*, *Z. Phys. C* **48** (1990) 663–672.
- [66] Y.-L. Wu, M. Zhong and Y.-B. Zuo, *B(s), D(s)  $\rightarrow$  pi, K, eta, rho, K\*, omega, phi Transition Form Factors and Decay Rates with Extraction of the CKM parameters |V(ub)|, |V(cs)|, |V(cd)|*, *Int. J. Mod. Phys. A* **21** (2006) 6125–6172, [[hep-ph/0604007](#)].
- [67] D. M. Straub, *flavio: a Python package for flavour and precision phenomenology in the Standard Model and beyond*, [1810.08132](#).
- [68] BABAR collaboration, J. P. Lees et al., *Search for the rare decays  $B\bar{B}\pi\ell^+\ell^-$  and  $B^0\bar{B}\eta\ell^+\ell^-$* , *Phys. Rev. D* **88** (2013) 032012, [[1303.6010](#)].

- [69] N. R. Soni, A. Issadykov, A. N. Gadaria, J. J. Patel and J. N. Pandya, *Rare  $b \rightarrow d$  decays in covariant confined quark model*, *Eur. Phys. J. A* **58** (2022) 39, [2008.07202].
- [70] BELLE collaboration, J. T. Wei et al., *Search for  $B \rightarrow \pi l^+ l^-$  Decays at Belle*, *Phys. Rev. D* **78** (2008) 011101, [0804.3656].
- [71] LHCb collaboration, R. Aaij et al., *First measurement of the differential branching fraction and CP asymmetry of the  $B^\pm \rightarrow \pi^\pm \mu^+ \mu^-$  decay*, *JHEP* **10** (2015) 034, [1509.00414].
- [72] FERMILAB LATTICE, MILC collaboration, J. A. Bailey et al.,  *$B \rightarrow \pi \ell \ell$  form factors for new-physics searches from lattice QCD*, *Phys. Rev. Lett.* **115** (2015) 152002, [1507.01618].
- [73] R. Bause, H. Gisbert, M. Golz and G. Hiller, *Model-independent analysis of  $b \rightarrow d$  processes*, *Eur. Phys. J. C* **83** (2023) 419, [2209.04457].
- [74] HPQCD collaboration, W. G. Parrott, C. Bouchard and C. T. H. Davies, *Standard Model predictions for  $B \rightarrow K \ell^+ \ell^-$ ,  $B \rightarrow K \ell^+ \ell^+ \ell^-$  and  $B \rightarrow K \nu \nu^-$  using form factors from  $N_f=2+1+1$  lattice QCD*, *Phys. Rev. D* **107** (2023) 014511, [2207.13371].
- [75] LHCb collaboration, R. Aaij et al., *Differential branching fractions and isospin asymmetries of  $B \rightarrow K^{(*)} \mu^+ \mu^-$  decays*, *JHEP* **06** (2014) 133, [1403.8044].
- [76] N. Gubernari, M. Reboud, D. van Dyk and J. Virto, *Improved theory predictions and global analysis of exclusive  $b \rightarrow s \mu^+ \mu^-$  processes*, *JHEP* **09** (2022) 133, [2206.03797].
- [77] BABAR collaboration, J. P. Lees et al., *Search for  $B^+ \rightarrow K^+ \tau^+ \tau^-$  at the BaBar experiment*, *Phys. Rev. Lett.* **118** (2017) 031802, [1605.09637].
- [78] W. Altmannshofer, P. Ball, A. Bharucha, A. J. Buras, D. M. Straub and M. Wick, *Symmetries and Asymmetries of  $B \rightarrow K^* \mu^+ \mu^-$  Decays in the Standard Model and Beyond*, *JHEP* **01** (2009) 019, [0811.1214].
- [79] J. Matias, F. Mescia, M. Ramon and J. Virto, *Complete Anatomy of  $\bar{B}_d \rightarrow \bar{K}^{*0} (- \rightarrow K \pi) l^+ l^-$  and its angular distribution*, *JHEP* **04** (2012) 104, [1202.4266].
- [80] S. Descotes-Genon, T. Hurth, J. Matias and J. Virto, *Optimizing the basis of  $B \rightarrow K^* l l$  observables in the full kinematic range*, *JHEP* **05** (2013) 137, [1303.5794].
- [81] LHCb collaboration, R. Aaij et al., *Angular analysis of  $B^0 \rightarrow K^{*0} e^+ e^-$  decays*, *JHEP* **06** (2025) 140, [2502.10291].
- [82] M. Algueró, A. Biswas, B. Capdevila, S. Descotes-Genon, J. Matias and M. Novoa-Brunet, *To (b)e or not to (b)e: no electrons at LHCb*, *Eur. Phys. J. C* **83** (2023) 648, [2304.07330].
- [83] LHCb collaboration, R. Aaij et al., *Measurement of CP-Averaged Observables in the  $B^0 \rightarrow K^{*0} \mu^+ \mu^-$  Decay*, *Phys. Rev. Lett.* **125** (2020) 011802, [2003.04831].
- [84] BELLE-II collaboration, I. Adachi et al., *Search for  $B^0 \rightarrow K^{*0} \tau^+ \tau^-$  Decays at the Belle II Experiment*, *Phys. Rev. Lett.* **135** (2025) 151801, [2504.10042].
- [85] LHCb collaboration, R. Aaij et al., *Angular Analysis of the  $B^+ \rightarrow K^{*+} \mu^+ \mu^-$  Decay*, *Phys. Rev. Lett.* **126** (2021) 161802, [2012.13241].
- [86] LHCb collaboration, R. Aaij et al., *Angular analysis of the decay  $B_s^0 \rightarrow \phi e^+ e^-$* , *JHEP* **07** (2025) 069, [2504.06346].
- [87] LHCb collaboration, R. Aaij et al., *Angular analysis of the rare decay  $B_s^0 \rightarrow \phi \mu^+ \mu^-$* , *JHEP* **11** (2021) 043, [2107.13428].

- [88] LHCb collaboration, R. Aaij et al., *Evidence for the decay  $B_S^0 \rightarrow \bar{K}^{*0} \mu^+ \mu^-$* , *JHEP* **07** (2018) 020, [1804.07167].
- [89] B. Kindra and N. Mahajan, *Predictions of angular observables for  $\bar{B}_s \rightarrow K^* \ell \ell$  and  $\bar{B} \rightarrow \rho \ell \ell$  in the standard model*, *Phys. Rev. D* **98** (2018) 094012, [1803.05876].
- [90] T. Felkl, S. L. Li and M. A. Schmidt, *A tale of invisibility: constraints on new physics in  $b \rightarrow s \nu \nu$* , *JHEP* **12** (2021) 118, [2111.04327].
- [91] BELLE-II collaboration, I. Adachi et al., *Evidence for  $B^+ \rightarrow K^+ \nu \nu^-$  decays*, *Phys. Rev. D* **109** (2024) 112006, [2311.14647].
- [92] BESIII collaboration, M. Ablikim et al., *Search for the decay  $D^0 \rightarrow \pi^0 \nu \bar{\nu}$* , *Phys. Rev. D* **105** (2022) L071102, [2112.14236].
- [93] G. D’Ambrosio, A. M. Iyer, F. Mahmoudi and S. Neshatpour, *Anatomy of kaon decays and prospects for lepton flavour universality violation*, *JHEP* **09** (2022) 148, [2206.14748].
- [94] BELLE collaboration, J. Grygier et al., *Search for  $B \rightarrow h \nu \bar{\nu}$  decays with semileptonic tagging at Belle*, *Phys. Rev. D* **96** (2017) 091101, [1702.03224].
- [95] DELPHI collaboration, W. Adam et al., *Study of rare  $b$  decays with the DELPHI detector at LEP*, *Z. Phys. C* **72** (1996) 207–220.
- [96] N. Castro, J. Erdmann, C. Grunwald, K. Kröninger and N.-A. Rosien, *EFTfitter—A tool for interpreting measurements in the context of effective field theories*, *Eur. Phys. J. C* **76** (2016) 432, [1605.05585].
- [97] A. Caldwell, D. Kollar and K. Kroninger, *BAT: The Bayesian Analysis Toolkit*, *Comput. Phys. Commun.* **180** (2009) 2197–2209, [0808.2552].
- [98] O. Schulz, F. Beaujean, A. Caldwell, C. Grunwald, V. Hafych, K. Kröninger, S. La Cagnina, L. Röhrig and L. Shtembari, *BAT.jl: A Julia-Based Tool for Bayesian Inference*, *SN Comput. Sci.* **2** (2021) 1–17, [2008.03132].
- [99] J. Buchner, *UltraNest – a robust, general purpose Bayesian inference engine*, 2101.09604.
- [100] M. Vihola, *Robust adaptive metropolis algorithm with coerced acceptance rate*, *Statistics and Computing* **22** (Sept., 2012) 997–1008.
- [101] CKMfitter Group, “Numerical results: CKMfitter Summer 2023.” [http://ckmfitter.in2p3.fr/www/results/plots\\_summer23/num/ckmEval\\_results\\_summer23.html](http://ckmfitter.in2p3.fr/www/results/plots_summer23/num/ckmEval_results_summer23.html), Jul, 2023.
- [102] CKMFITTER GROUP collaboration, J. Charles, A. Hocker, H. Lacker, S. Laplace, F. R. Le Diberder, J. Malcles, J. Ocariz, M. Pivk and L. Roos, *CP violation and the CKM matrix: Assessing the impact of the asymmetric  $B$  factories*, *Eur. Phys. J. C* **41** (2005) 1–131, [hep-ph/0406184].
- [103] FLAVOUR LATTICE AVERAGING GROUP (FLAG) collaboration, Y. Aoki et al., *FLAG Review 2024*, 2411.04268.
- [104] BELLE collaboration, O. Lutz et al., *Search for  $B \rightarrow h^{(*)} \nu \bar{\nu}$  with the full Belle  $\Upsilon(4S)$  data sample*, *Phys. Rev. D* **87** (2013) 111103, [1303.3719].
- [105] BELLE-II collaboration, W. Altmannshofer et al., *The Belle II Physics Book*, *PTEP* **2019** (2019) 123C01, [1808.10567].

- [106] J. F. Kamenik and C. Smith, *Tree-level contributions to the rare decays  $B^+ \rightarrow \pi^+ \nu$  anti- $\nu$ ,  $B^+ \rightarrow K^+ \nu$  anti- $\nu$ , and  $B^+ \rightarrow K^{*+} \nu$  anti- $\nu$  in the Standard Model*, *Phys. Lett. B* **680** (2009) 471–475, [[0908.1174](#)].
- [107] R. Bause, H. Gisbert, M. Golz and G. Hiller, *Interplay of dineutrino modes with semileptonic rare  $B$ -decays*, *JHEP* **12** (2021) 061, [[2109.01675](#)].
- [108] A. J. Buras, J. Girrbach-Noe, C. Niehoff and D. M. Straub,  *$B \rightarrow K^{(*)} \nu \bar{\nu}$  decays in the Standard Model and beyond*, *JHEP* **02** (2015) 184, [[1409.4557](#)].
- [109] FCC collaboration, M. Benedikt et al., *Future Circular Collider Feasibility Study Report: Volume 1, Physics, Experiments, Detectors*, [2505.00272](#).
- [110] X. Ai et al., *Flavor physics at the CEPC: a general perspective\**, *Chin. Phys.* **49** (2025) 103003, [[2412.19743](#)].
- [111] M. Achasov et al., *STCF conceptual design report (Volume 1): Physics & detector*, *Front. Phys. (Beijing)* **19** (2024) 14701, [[2303.15790](#)].
- [112] R. Bause, H. Gisbert and G. Hiller, *Implications of an enhanced  $B \rightarrow K \nu \bar{\nu}$  branching ratio*, *Phys. Rev. D* **109** (2024) 015006, [[2309.00075](#)].
- [113] J. de Blas, A. Goncalves, V. Miralles, L. Reina, L. Silvestrini and M. Valli, *Constraining new physics effective interactions via a global fit of electroweak, Drell-Yan, Higgs, top, and flavour observables*, [2507.06191](#).
- [114] U. Chattopadhyay, D. Das, R. Puri and J. Roy, *Constraining lepton flavor violating  $2q2\ell$  operators from low-energy  $cLFV$  processes*, [2507.13141](#).
- [115] M. Beneke and M. Neubert, *Flavor singlet  $B$  decay amplitudes in QCD factorization*, *Nucl. Phys. B* **651** (2003) 225–248, [[hep-ph/0210085](#)].
- [116] V. M. Braun et al., *The  $\rho$ -meson light-cone distribution amplitudes from lattice QCD*, *JHEP* **04** (2017) 082, [[1612.02955](#)].
- [117]  $\chi$ QCD collaboration, Y. Chen, W.-F. Chiu, M. Gong, Z. Liu and Y. Ma, *Charmed and  $\phi$  meson decay constants from 2+1-flavor lattice QCD*, *Chin. Phys. C* **45** (2021) 023109, [[2008.05208](#)].
- [118] M. S. Bhagwat and P. Maris, *Vector meson form factors and their quark-mass dependence*, *Phys. Rev. C* **77** (2008) 025203, [[nucl-th/0612069](#)].
- [119] D. Bečirević, G. Duplančić, B. Klajn, B. Melić and F. Sanfilippo, *Lattice QCD and QCD sum rule determination of the decay constants of  $\eta_c$ ,  $J/\psi$  and  $h_c$  states*, *Nucl. Phys. B* **883** (2014) 306–327, [[1312.2858](#)].
- [120] D. Hatton, C. T. H. Davies, J. Koponen, G. P. Lepage and A. T. Lytle, *Bottomonium precision tests from full lattice QCD: Hyperfine splitting, Upsilon leptonic width, and  $b$  quark contribution to  $e^+e^- \rightarrow$  hadrons*, *Phys. Rev. D* **103** (2021) 054512, [[2101.08103](#)].
- [121] FERMILAB LATTICE, MILC collaboration, A. Bazavov et al.,  *$D$ -meson semileptonic decays to pseudoscalars from four-flavor lattice QCD*, *Phys. Rev. D* **107** (2023) 094516, [[2212.12648](#)].
- [122] G. S. Bali, S. Collins, S. Dürer and I. Kanamori,  *$D_s \rightarrow \eta, \eta'$  semileptonic decay form factors with disconnected quark loop contributions*, *Phys. Rev. D* **91** (2015) 014503, [[1406.5449](#)].
- [123] E. McLean, C. T. H. Davies, J. Koponen and A. T. Lytle,  *$B_s \rightarrow D_s \ell \nu$  Form Factors for the*

full  $q^2$  range from Lattice QCD with non-perturbatively normalized currents, *Phys. Rev. D* **101** (2020) 074513, [[1906.00701](#)].

[124] A. Bharucha, D. M. Straub and R. Zwicky,  $B \rightarrow V \ell^+ \ell^-$  in the Standard Model from light-cone sum rules, *JHEP* **08** (2016) 098, [[1503.05534](#)].

[125] N. Gubernari, A. Kokulu and D. van Dyk,  $B \rightarrow P$  and  $B \rightarrow V$  Form Factors from  $B$ -Meson Light-Cone Sum Rules beyond Leading Twist, *JHEP* **01** (2019) 150, [[1811.00983](#)].